Quantifying Uptake, Transport, and Elimination in 3D Self-Assembled Microtissues

by

Toni-Marie Achilli

B.S., The Johns Hopkins University, 2014

Submitted in partial fulfillment of the requirements for the degree of Doctor of Philosophy in the Program of Biomedical Engineering at Brown University

Providence, Rhode Island

March 2014

This dissertation by Toni-Marie Achilli is accepted in its present form by the Program of Biomedical Engineering as satisfying the dissertation requirement for the degree of Doctor of Philosophy.

Date_____ _____

Jeffrey Morgan, Ph.D., Advisor

Recommended to the Graduate Council

Date_____ _____

Anubhav Tripathi, Ph.D., Reader

Date_____ _____

Diane Hoffman-Kim, Ph.D., Reader

Date_____ _____

Karen Harnett, Ph.D., Reader

Date_____ _____

Angela Slitt, Ph.D., External Reader

Approved by the Graduate Council

Date_____ _____

Peter Weber, Dean of the Graduate School

Curriculum Vitae

Toni-Marie (Ferruccio) Achilli was born at Women and Infants Hospital in Providence, RI on March 17, 1986 and was raised in Johnston, RI. She attended Johnston Senior High School where she played softball, was class president, student body president, and an integral member of the school's academic decathlon team. She graduated from The Johns Hopkins University in 2008 with a B.S. in Chemical and Biomolecular Engineering. At Johns Hopkins she gained research experience in the laboratories of Dr. Erika Matunis and Dr. Marc Ostermeier, and attained additional experience in the lab of Dr. Kristi Wharton at Brown University. After graduating, Toni-Marie pursued her PhD in Biomedical Engineering at Brown University under the guidance of Dr. Jeffrey Morgan.

Toni-Marie Achilli
14 Jasmine Lane Johnston, RI 02919
401-764-5826
tonimarie.achilli@gmail.com

Education

Graduate Student - Doctoral Candidate, Biomedical Engineering
Brown University*, Providence, RI*
Expected: May 2014
GPA 4.0/4.0

B.S. Degree in Chemical and Biomolecular Engineering
The Johns Hopkins University, *Baltimore, MD*
May 22, 2008
G.P.A. 3.3/4.0

Related course work: Biology of the Eukaryotic Cell, Molecular Pharmacology and Physiology**,** Biochemistry, Genetics, Cell Biology, Analysis of Development, Drug and Gene Delivery, Cell Physiology and Biophysics, Biotransport Processes, Therapeutic and Diagnostic Colloids, Kinetic Processes, Separations, Organic Chemistry, Thermodynamics, Applied Physical Chemistry

Awards and Associations:

- Research featured as 1 of the top 10 medical breakthroughs of 2010 by Time Magazine (artificial ovary)
- Awarded best poster presentation at International Conference on Frontiers in Pharmaceutical Sciences
- Dean's List
- June R. Levy Fellowship
- Biomedical Engineering Society

Teaching Experience

Adjunct Faculty, Community College of Rhode Island, Lincoln, RI
Department of Biology
Human Physiology Biol:1020
Fall 2013-current

- Taught Lecture and laboratory sections of human physiology for students preparing to apply for the nursing program

Teaching Assistant, Brown University, Providence, RI
Department of Molecular Pharmacology, Physiology, and Biotechnology
Biomedical Engineering and Biotechnology Seminar, Professor Jeffrey Morgan
Fall 2011-current

Teaching Assistant, Brown University, Providence, RI
Department of Molecular Biology, Cell Biology, and Biochemistry
The Foundations of Living Systems, Professor Kenneth Miller
January 2010-May 2010

Research Experience

Morgan Lab, *Brown University, Providence, RI*
August 2008-current

- Developed a method to quantify transport through 3D micro-tissues using epi-fluorescent microscopy
- Measured the effects of p-glycoprotein inhibitors and gap junction inhibitors in primary cells and cell lines
- Determined that p-glycoprotein inhibitors may block transport of drugs into tumors via the unwanted side effects on gap junctional communication
- Developed a method to quantify cellular self-sorting
- Created an artificial ovary to be used in *in vitro* maturation of oocytes

Ostermeier Lab, *The Johns Hopkins University, Baltimore, MD*
January 2006-May 2008

- Isolated and purified protein molecular switches through biochemical techniques to be used for kinetic assays
- Created a protein library of every one base truncation of a gene via incremental truncation

Amgen Inc.*, Enbrel Manufacturing Facility, West Greenwich, RI*
May 2007-August 2007

- Assigned to spare parts project which was designed to ensure that every system used in the manufacturing of Enbrel was equipped with the correct spare parts such that the mission of Amgen, "every patient, every time", was achieved
- Exposed to controlled cGMP
- Created templates from P&IDs of 125 systems to be used for walk downs of the equipment
- Analyzed chromatography elution trends in Pi database
- Hands on exposure to the manufacturing facility of both upstream and downstream processes of the production of Enbrel

Wharton Lab*, Brown University, Providence, RI*
May 2005-January 2007 (seasonal)

- Analysis of TGF-β signaling pathway to determine the effect of *dpp* and *gbb* ligand location on cell communication in the imaginal discs and ovaries of *Drosophila melanogaster* using dissection, confocal microscopy, and SEM
- Designed vectors with specific restriction enzymes so that the *dpp* and *gbb* chimeras could be inserted to properly facilitate the expression in *Drosophila*
- Created protein chimeras of the *dpp* and *gbb* ligands by means of biochemical techniques

Matunis Lab, *The Johns Hopkins University School of Medicine, Baltimore, MD*
November 2004-February 2006

- Analysis of the JAK/STAT signaling pathway via the effect of ligand concentration on stem cell fate and renewal, *Drosophila melanogaster* used as model system
- Genetically engineered knock-out mutants and analyzed testes for a corresponding change in stem cell number via dissection and confocal microscopy

Publications and Abstracts

Published Manuscripts

1. **Achilli TM**, McCalla S, Tripathi A, Morgan JR. Quantification of the kinetics and extent of self-sorting in three dimensional spheroids. Tissue Eng Part C Methods 2012;18(4): 302-9.

2. **Achilli TM**, Meyer J, Morgan JR. Advances in the formation, use and understanding of multi-cellular spheroids. Expert Opin Biol Ther 2012;12(10): 1347-60.

3. Tejavibulya N, Youssef J, Bao B, **Ferruccio TM**, Morgan JR. Directed self-assembly of large scaffold-free multi-cellular honeycomb structures. Biofabrication 2011;3(3): 034110.

4. Krotz SP, Robins JC, **Ferruccio TM**, et al. In vitro maturation of oocytes via the pre-fabricated self-assembled artificial human ovary. J Assist Reprod Genet 2010;27(12): 743-50.

5**.** Youssef J, Bao B, **Ferruccio T-M**, Morgan JR. (2010), "Micromolded Nonadhesive Hydrogels for the Self-Assembly of Scaffold-Free 3D Cellular Microtissues" Methods in Bioengineering 3D Tissue Engineering. Francois Berthiaume and Jeffrey Morgan. Norwood, MA: Artech House. P 151-166

Submitted Manuscripts

1**. Achilli TM**, McCalla S, Meyer J, Tripathi A, Morgan JR. Multi-Layer Spheroids to Quantify Drug Uptake and Diffusion in 3D. Molecular Pharmaceutics 2014.

Manuscripts in Preparation

1. **Achilli TM**, Morgan JR. Quantification of Tissue Elimination from 3D Multi-Layer Spheroids. Drug Metabolism and Disposition.

Patent Applications

1.U.S. Application No.: 13/623,599
Filing Date: September 20, 2012
Title: Differential Effects Of Drugs On Transport In A Multi-layer 3D Spheroid Model
Your Reference No.: BU 2079
Our Docket No.: 2670.2021-001

2. U.S. Application No.: 13/623,668
Filing Date: September 20, 2012
Title: Mechanotransduction By The Synergistic Action Of Heterotypic Cell Interactions
Brown Reference No.: BU 2095
Our Docket No.: 2670.2020-001

Abstracts

1**. Achilli, T.M**., McCalla, S., Tripathi, A., Morgan, J.R. "A New Model for Quantifying Drug Uptake and Transport in 3D Multicellular Spheroids: A Case Study for P-glycoprotein," Oral Presentation. Internation Conference on Frontiers in Pharmaceutical Sciences, South Kingston, RI (URI), September 28-30, 2012

2. **Ferruccio, T.M**., McCalla, S., Tripathi, A., Morgan, J.R. "Quantifying the Extent and Kinetics of Self-Assembly and Self-Sorting in 3D Microtissues," Oral Presentation. Biomedical Engineering Society Fall Meeting, Austin Texas, October 6-9, 2010

Preface and Acknowledgements

Foremost, I would like to express my sincere gratitude to my thesis advisor, and mentor, Dr. Jeffrey Morgan for his excellent guidance, support, caring, patience, and for providing me with an excellent atmosphere for conducting research. I attribute the accomplishments of this thesis to his continual encouragement and effort. I admire the scientist and man that you are, and the dedication that you have to your students. The independence and flexibility that you have entrusted in me allowed me to flourish as a research scientist and in my personal goals. I am honored to have learned so much from you over these years.

I would also like to thank my thesis committee, for their support and advice throughout the various stages of my research. I would especially like to thank Dr. Anubhav Tripathi and Dr. Stephanie McCalla for the collaborations that made this thesis possible. Additionally, I would like to thank the departmental staff for all of their administrative support. To all the past and present members of the Morgan, Hoffman-Kim, Mathiowitz, and Darling laboratories – thank you for promoting a stimulating and welcoming academic and social environment.

Above all I would like to thank my family, for their unequivocal support. To my Mom and Dad, thank you for always believing in me and my success, and always putting your children first - affording me every opportunity to succeed. I certainly would not be finishing my PhD without the work ethic and commitment that you have taught me, along with all of the sacrifices that you have made. Gerald, Victoria, and Katerina, although you may be younger than me, I have learned so much from the three of you in terms of following your passion and how to not take everything so seriously. I do look up to the

three of you more than you know, and you are my best friends. To Evie - thank you for always being my biggest cheerleader in everything that I do - I know that Papa would be so proud!!!

To my biggest supporters, my husband, Jason and my son, Anthony. Words cannot adequately express how thankful I am to have the both of you in my life. As with everything, you have supported me through every step and displayed incredible patience with me. The two of you have provided me with so much motivation, especially in these final months leading to graduation. I love you both, and just hope that I have made you as proud as I am of you.

And, to baby girl, although I cannot wait to meet you, thank you for staying put and allowing me to finish this thesis on time.

Table of Contents

List of Figures

Chapter 1: Introduction

1.1 ATP-Binding Cassette (ABC) Transporters

Cell membranes play an important physiological role in forming barriers between the internal and external cellular environments. On these cell membranes exists proteins that act as active transporters for both the import and export of molecules such as nutrients, wastes, and drugs. A large class of these transporters includes the ATP-binding cassette (ABC) transporters that are crucial to both the physiological and toxicological role of the export, or efflux, process. These pumps are particularly important because of the broad range of structurally diverse substrates that they can transport. While they were first discovered in prokaryotic cells as import nutrient pumps, their importance was realized when they were discovered to be involved in the multi-drug resistance of eukaryotes[1]. Since their discovery in the human genome, 48 ABC-transporters belonging to 7 subfamilies have been identified, with three (P-glycoprotein, breast cancer resistance protein, and multi-drug resistant associated proteins) having particular importance to the absorption, distribution, metabolism, excretion and toxicity (ADME-Tox) of clinically important drugs as well as multi-drug resistance[2]. The following will emphasize the importance of ABC-transporters, particularly P-glycoprotein to these phenomena.

1.1.1 The Structure and Mechanism of ABC-transporters

ABC-transporters are large; membrane bound proteins that in general contain a combination of cytoplasmic ATP-binding domains (NBDs) (usually 2) and helical membrane-spanning domains (TMDs) (usually a minimum of 12). These transporters are named after their conserved ATP-binding domain which is responsible for the hydrolysis of ATP, the energy source for this active transport[3]. While a high resolution structure of

eukaryotic ABC-transporters is not available, it is believed the substrate binding sites are located within the TMDs of the pump[4].

Based on the available structural information, the model for efflux from these pumps can be explained by high and low affinity substrate states with cycles of ATP-hydrolysis to move substrates against their concentration gradients[3, 5, 6]. The mechanism of how the transporters function can be explained by four distinct steps: (1) substrate binding, (2) ATP-binding, (3) substrate translocation, and (4) ATP-hydrolysis which returns the pump to the original substrate binding conformation. When ATP is not bound the transporter is considered to be in the "open" conformation (open towards the cytosol) which is the high substrate affinity state. As substrates diffuse into the cells they can access the substrate binding pockets from either the leaflets of the plasma membrane or from the cytosol. As the substrate binds, there is a conformational change, particularly in the NBDs, which leads to the binding of ATP. When ATP binds to the NBDs a conformational change to the "closed" conformation occurs, and it is now closed to the cytosol. This conformation is the low substrate affinity state. Thus, the decreased affinity for the substrate leads to the efflux of the substrate out of the cell. Finally, the hydrolysis of ATP provides the energy required to return the pump to its open, high substrate affinity conformation[3, 5-7](**Figure 1-1**).

1.1.2 P-glycoprotein (ABCB1, MDR1, Pgp)

P-glycoprotein will be the main focus of the remainder of this thesis. Pgp was first discovered in Chinese hamster ovary cells (CHO) cells that displayed multi-drug resistance, and was found to be a 170 kDa glycoprotein with a role in drug permeability[8]. Pgp has been found to have a very broad range of tissue distribution in the body, including but not limited to hepatocytes, renal proximal tubules, endothelial cells, the

placenta, ovary, and testes[9](**Figure 1-2)**. This transporter effluxes a wide range of structurally diverse substrates including steroids, carcinogen, numerous classes of drugs, and many chemotherapeutics (paclitaxel, vinca alkaloids, and anthracyclines)[10-14]. In general, these are bulky amphipathic molecules that range from 200-1900 Da in size. Most of these substrates are hydrophobic in nature which allows them to easily cross cell membranes into tissues and pharmacological compartments. Pgp in the GI tract affects the ability of drugs to be absorbed and reach their intended target, while overexpression in tumor cells leads to increased chemoresistance by decreasing the cellular accumulation of the therapeutic[15].

There have been numerous molecules and drugs that have been found to inhibit and modulate the activity of Pgp including calcium channel blockers, calmodulin antagonists, and immunosuppressants[14, 16, 17]. Many of the identified inhibitors are also substrates of Pgp and thus act as competitive inhibitors. Unfortunately, the use of drugs to modulate Pgp in the clinic has led to poor clinical translation. This is in part to Pgp's physiological importance being so broad and can cause toxicity issue or decreased transport into intended tissue targets. The role of Pgp to these processes, particularly the ADME-Tox of drugs and multi-drug resistance is to be discussed in more detail in the sections that follow.

1.2 The Role of P-glycoprotein to the ADME-TOX of Drugs

Pharmacokinetics has been defined to study the absorption, distribution, metabolism, and excretion of drugs within a biological system. Historically, the focus of the ADME-Tox of a drug was attributed to the passive transport of drugs crossing cell membranes and the metabolism needed for the final excretion of the drug. Now, there has been an increased importance placed on the role of transporters to these pharmacological events. It is now widely recognized that the ADME-Tox of drugs is modulated by the active transport of import and efflux pumps. In particular efflux transporters are especially important to the study of hydrophobic substrates that passively cross through lipid membranes, and are then pumped out. The importance of transporters, particularly of Pgp, has been noted by drug regulatory agencies which require all new drug candidates to undergo testing to determine if the test compound interacts with Pgp (drug-transporter interactions) and to predict unwanted drug-drug interactions (DDIs)[18].

1.2.1 The Role of P-glycoprotein in Drug Absorption and Distribution

Drugs must pass several physiological barriers before reaching its intended target site[19]. One of the most formidable of these barriers is that of the intestinal epithelium, which expresses many transporters. At this barrier Pgp is expressed along the apical membrane of the intestine, pumping substrates from the basolateral to apical side, and thus limits absorption by effluxing substrates back into the lumen of the gut[20, 21]. The action of Pgp at this barrier decreased the bioavailability of orally administered drugs[22]. Studies have shown that increased tissue absorption of orally administered Pgp substrates can be achieved when they are administered concurrently with a Pgp inhibitor. This action can pose a significant obstacle for the therapeutic applications of drugs. This action can be studied using monolayers of caco-2 cell monolayers and should be checked

early in drug development to determine if test compounds are also Pgp substrates. If the compound also proves to be a good Pgp substrate it could be prohibitive to the intended therapeutic applications.

Pgp is also expressed at other important barriers such as the blood-brain barrier (BBB), blood-placental barrier, blood-CNS barrier, and blood-testis barrier. At these barriers Pgp plays an important role to restrict the accumulation of drugs that could be potentially toxic to the organs that they protect[19, 23]. For example, Pgp expressed in trophoblast cells pump drugs back into the maternal blood so that it does not reach the developing fetus. A negative consequence of this is that the pump also limits the drug penetration into these organs when a treatment is needed behind the barrier. For example, Pgp is expressed in the endothelial cells of the BBB to limit the passage of hydrophobic drugs into the brain, and effluxes them back into the blood, decreasing penetration up to 100 fold. This is problematic when treating gliomas in the brain with chemotherapeutics[24, 25].

1.2.2 The Role of P-glycoprotein in Drug Elimination

Pharmacokinetics defines the elimination as the endpoint by which drugs or their metabolites are excreted from the body. Another equally important aspect to elimination is the rate at which drugs are effluxed from the tissues from which they have penetrated. The main routes of traditional drug elimination are biliary excretion and renal clearance[20, 21, 26]. In the liver, Pgp is localized to the canalicular membrane of hepatocytes and aids drug excretion into the bile. In the kidney, Pgp is expressed in both renal and epithelial cells as well as the renal proximal tubules, aiding elimination into the urine. The absence of Pgp in the kidney leads to complex changes to the overall renal excretion and ultimately the total clearance of the drug. There is also an important protective role of

Pgp to the kidney itself. During renal failure there is an increased expression of Pgp to help the organ eliminate toxins.

1.2.3 The Role of P-glycoprotein in Drug-Drug Interaction and Multi-Drug Resistance

An additional consideration in studying the role of transporter to ADME-Tox is determining the possible drug-drug interaction or drug-transporter interactions that result from interactions with these pumps[27]. These interactions with transporters can lead to increasing the drug concentration in different body compartments, such as the brain, without changing the actual blood levels of the drug. An example of this includes flavonoids in grapefruit juice which inhibits Pgp efflux in the body and the increases the bioavailability of drugs taken with it[28]. Ultimately this leads to a change in the drugs tissue distribution.

The two main mechanisms of transporter mediated drug-drug interactions include: (1) an increase in competition between drugs for binding sites during polymedication which leads to impairing the transport of the drugs, particularly the drug with the lower pump affinity is most affected and (2) exposure to drugs that can lead to a change in the overall expression profile of the transporter, and the affects the transport of all pump substrates. A change in the expression of the pumps can lead to an acquired multi-drug resistance[29]. For example, overexpression of transporters in cancer cells generally leads to a poor overall prognosis because they have the ability to efflux anti-cancer drugs much more rapidly from the cells[29]. Multi-drug resistance and the role of transporters to cancer will be discussed in more detail in the following section.

1.3 The Role of P-glycoprotein in Multi-Drug Resistance of Cancer

While aggressive chemotherapeutic regimens are the most effective treatment of cancer and metastatic tumors, these treatments do not always lead to successful outcomes. Multi-drug resistance is one of the major contributing factors that impede the action of anticancer drugs from affecting its intended target. Even dosing regimens consisting of a combination of multiple therapeutics do not lead to more effective treatments because of the nature of multi-drug resistance[30].

1.3.1 The Role of P-glycoprotein in Cancer

Many clinical studies have been conducted to study the role that ABC-transporters have in cancer and metastasis, and particularly the role of Pgp. It was originally discovered that Pgp was highly expressed in cancers derived from tissues that constitutively expressed Pgp for their normal function, especially in colon, kidney, and hepatocellular cancers, but was later found that Pgp expression could be induced in nearly all cancers[31]. It was originally believed that Pgp expression alone could adequately explain drug resistance, but it is now known that many other factors contribute to this phenomenon.

In general, an increase in Pgp expression has been shown to correlate with cancers that are less differentiated, and thus more malignant. As the expression level impairs the chemotherapeutic, the expression of Pgp actually increases. In many studies of cells of solid tumors this correlation has been shown to exist. For example, it is reported in breast cancer that up to 41% express high levels of Pgp, and the expression actually increases after therapy leading to greater failure rates[32, 33]. Different studies report that between 15-50% of ovarian cancers express Pgp[34, 35]. And, in sarcomas there is a strong correlation between Pgp and the relapse and survival rate in patients[36].

1.3.2 Cellular Mechanics of Multi-Drug Resistance

In general resistance to anticancer drugs can result from two different mechanisms, both of which are impacted by the expression and efflux mediated by Pgp and other ABC-transporters. The first of these mechanisms is the impaired delivery of chemotherapeutics to the targeted cells. This impaired delivery is due to poor absorption and the decreased bioavailability of the drug when it is orally administered.

The second mechanism of multi-drug resistance occurs due to molecular changes to the cell itself, primarily increased expression of Pgp. This acquired resistance leads to an increase in drug efflux from the cells and a decreased intracellular drug concentration below therapeutically relevant levels. *In vitro* studies of multi-drug resistance has shown that cells can acquire resistance when they are incubated in a drug for prolonged periods of time, which can then be reversed using inhibitors of the efflux pump. When these resistant cells are transplanted to *in vivo* or are studied in three-dimensional spheroids, the resistance can no longer be reversed[37, 38]. This suggests that expression and inhibition of Pgp and transporters alone may not be sufficient to fully explain multi-drug resistance, as environmental factors and geometry may affect this reversal.

In addition to these two main mechanisms, multi-drug resistance can also arise from numerous other mechanisms including decreased uptake of the drug, changes to apoptosis, or an activation of DNA repair pathways[39, 40]. Since the cancer cells within a tumor are considered to be heterogeneous, and are affected by multi-drug resistance differently, it is believed that more than one mechanism of multi-drug resistance will be present in ag given solid tumor.

1.3.3 The Role of P-glycoprotein Inhibitors to the Reversal of Multi-Drug Resistance

In vitro studies have identified numerous drugs and molecules that have been shown to reverse Pgp-mediated multi-drug resistance in cancer cells. And, although research efforts have been made for over thirty years, and up to third generation inhibitors have been identified, there are still disappointing clinical results. In fact, there is no inhibitor currently used in the clinic to reverse multi-drug resistance.

The first generation of inhibitors consisted of drugs that were already approved for other clinical conditions and also inhibited Pgp. Examples included cyclosporine and verapamil, both of which had promising results, but displayed unwanted DDIs and increased toxicity to other organs, such as cardiotoxicity[17, 41, 42]. Second generation inhibitors were modeled after the first generation to possess increased potency and decreased toxicity. Results with these inhibitors were found to be less effective clinically. Valspodar, a cyclosporine derivative, was the most studied second generation inhibitor, showed that there was no benefit to co-administering it with paclitaxel in the treatment of ovarian cancers[43]. It is now believed that clinical benefit to modulating Pgp through inhibitors for cancer may be hard to realize because of several other existing limitations that exist when using these inhibitors. For example, modulating Pgp also alters the pharmacokinetics of the drug, in particular it may decrease overall clearance of the drug and lead to toxicity and increased side effects. Also, while Pgp is still believed to be the most influential of the transporters, it has been shown that up to 20 of the ABC-transporters may have a role in multi-drug resistance, and the expression of multiple of these transporters proves troublesome because their substrates overlap.

1.4 Methods for Identifying Transporter Activity and Modulation

Increasing recognition of the role of transporters to the absorption, distribution, and elimination of many drugs, as well as their contribution to multi-drug resistance in cancer, has led to the development of several *in vitro* assays used to predict the effect of new drugs and to find new inhibitors of these pumps. Additionally, the importance of identifying potential drug-drug interactions that change drug disposition, efficacy, or can lead to toxicity has led to regulatory agencies expecting new drug candidates to have been investigated to predict the risk of transporter-mediated DDIs. The current *in vitro* methods used can be divided into two main categories, membrane based and cellular based assays[44, 45].

1.4.1 Membrane Based Assays

Membranes isolated from cells expressing ABC-transporters, or cells genetically modified to overexpress a particular transporter, allow for a straightforward characterization of specific transporter proteins, and are amenable to high throughput screening. Such assays are most useful in obtaining data on substrate affinity and substrate specificity. Another added advantage is that since membranes are not living cells cytotoxicity does not have to be considered (**Figure 1-3)**.

1.4.1.1 Vesicular Transport assay

The vesicular transport assay is a method to study the directional translocation of test compounds by transporters, since transport is unidirectional. Membranes are prepared from cells overexpressing transporters or from tissues expressing endogenous levels of the protein. Inside-out vesicles are oriented such that the ATP binding domain and substrate binding site of the transporter face the outside media. Test compounds that are substrates are transported into the vesicles during incubation[46]. Rapid filtration can be

used to separate the vesicles from the incubation solution and the test compound remains inside the vesicle. In this assay compounds can be labelled or unlabeled and then quantified. Unlabeled compounds can be determined by high resolution and high sensitivity assays such as HPLC[47]. Alternatively, radiolabelled and fluorescent compounds can be quantified using standard techniques. While this assay can measure the direct transport of a substrate, its disadvantage is that compounds with medium-to-high permeability are not retained inside the vesicles making measurements of these compounds difficult to quantify.

1.4.1.2 ATPase Activity Assay

The ATPase activity assay is an indirect method that can be used to distinguish if test compounds are substrates or inhibitors of the pump, using membrane vesicles prepared from cells or isolated proteins. Since the efflux of compounds is energized by ATP, increase in the transport of a substrate would lead to an increase in the rate of ATP-hydrolysis. Similarly, an inhibitor would decrease the rate at which substrates are transported, and would lead to a decrease in ATP-hydrolysis[46]. The rate of ATP-hydrolysis can be quantified experimentally by the release of inorganic phosphate and measured by colorimetric reactions. While this assay is amenable to high throughput testing and allows for a kinetic analysis that can predict unwanted DDIs, the main disadvantage of this assay is that the data analysis is not straightforward, since many of the inhibitors of these pumps are competitive inhibitors. These competitive inhibitors are also substrates that are transported which add complexity to the net effect on ATP-hydrolysis.

1.4.1.3 Drug Binding/Photoaffinity Labeling Assay

The drug binding/photoaffinity labeling assay can be used to determine if a test compound interacts and binds to a transporter. In this assay membranes are prepared from cells containing overexpressed levels of proteins and are then incubated with photoaffinity labeled compounds. UV irradiation is used to permanently attach the compounds to the transporter, which can then be quantified[48]. While this assay is amenable to high throughput testing and is attuned at determining DDIs, it cannot distinguish between compounds that are substrates or inhibitors of the pumps.

1.4.2 Cell Based Assays

There have been several cell based assays developed to study the transport of compounds by transporters and to identify inhibitors of these pumps. Genetically engineered cell lines are used to conduct these studies more often than cells expressing only endogenous levels of the pumps. Overexpressed cells allow for the in-depth study of a particular transporter rather than a net effect of all the expressed pumps, and they can be modified to overexpress more than one transporter. An important example would be cells that are modified to overexpress both efflux and influx transporters to model the complex processes involved in the ADME-Tox of compounds. These assays are generally amenable to high throughput analysis and can be used to determine important kinetic parameters. A disadvantage to using cultured cells is that changes in the expression level of transporters either by overexpression or culturing conditions could lead to a different correlation in the *in vivo* situation (**Figure 1-4**).

1.4.2.1 Cytotoxicity/Chemosensitivity/Multi-drug Resistance Assay

The cytotoxicity/chemosensitivity/multi-drug resistance assay is generally used to test both substrates and inhibitors of transporters. Cell lines that are modified to overexpress specific pumps are cultured in varying concentration of the substrate or

inhibitor and the IC_{50} of the compound is calculated. In addition to IC_{50} calculation endpoint quantification such as ATP content, release of cytoplasmic enzymes, dye uptake, and macromolecule synthesis can be determined. Results from overexpressed cell lines are compared to results from parental cell lines expressing only endogenous levels of pumps. Pump inhibitors can be identified as those compounds that increase the cytotoxicity of known substrates. While this assay is straightforward and quantitative, results are highly depended on the expression level of the transporters.

1.4.2.2 Cellular Accumulation Assay

The cellular accumulation assay is based on the principle that transported substrates will have less accumulation in cells that express transporters, and inhibitors will increase the accumulation of the substrates. While this assay can use labeled or unlabeled substrates, it is particularly useful to use substrates that are naturally fluorescent or are radioactively labeled. This assay is often used to discover transport pump inhibitors using fluorescent dyes, such as calcein-AM or rhodamie-123[47, 49]. The main limitation to this assay is that only few test compounds are naturally fluorescent or are available in a labeled form without changing its affinity for the transporter.

1.4.2.3 Transcellular (Vectorial) Transport Assay

The transcellular transport assay models vectorial transport across polarized cellular monolayers, and are particularly useful to study the transport of compounds across physiological barriers. Cell lines used in this assay must be polarized and express the transporters in the appropriate membrane domains of the cell. Cells are seeded to confluence on a semi-permeable membrane in a transwell system. Since the cells are polarized the compound is added to the apical or basal side of the monolayer, and after a given time the concentration of the substrate is measured on both sided of the membrane.

The apical-basolateral (A-B) and basolateral-apical (B-A) transport rates are measured to determine the role and directionality of the transport of the compound. For transporters such as Pgp, B-A transport will dominate since Pgp is expressed on the apical membrane of the cell[49-51]. For known substrates, this assay is useful in testing compounds as inhibitors of the pumps. This assay is considered to be a sensitive method since only the transport of the test compound is measured. Another advantage to this assay is that it can quantify the active versus the passive transport of compounds. A disadvantage to this assay is that compounds with low permeability are not useful unless transport is aided by an uptake transporter.

1.4.2.4 Sandwich-Cultured Hepatocyte Assay

The sandwich-cultured hepatocyte assay is a more sophisticated and complex technique to analyze the vectorial transport of substrates into the bile canaliculi. Sandwich-cultured hepatocytes are plated on collagen-coated plates and then covered with collagen or a matrigel. Hepatocytes cultured this way (after 5-7 days) have increased value because the cells retain many of the *in vivo* like properties important to transport, such as an intact canalicular network with polarized transporter expression[52]. Test compounds are incubated with cultured cells, with or without inhibitors present. Transport specifically into the bile canaliculi can be measured by incubation in Ca^{2+}-free media which disrupts the tight junctions that form the canalicular network. This assay can be used to estimate the biliary clearance and has shown good correlation to *in vivo* measurements[52, 53]. Additionally, this assay can distinguish between substrates, inhibitors and predict DDIs. The main disadvantages of this assay are the time required for the localization of the transporters to the appropriate cellular membrane locations, and that cells in Ca^{2+}-free media for prolonged periods can lead to cytotoxicity.

1.5 Advances in the Formation, Use and Understanding of Multi-Cellular Spheroids

(The following section was published in Expert Opinion on Biological Therapies October 2012 doi: 10.1517/14712598.2012.707181. Epub 2012 Jul 12)

1.5.1 Introduction

The culture of mammalian cells in vitro has led to numerous conceptual advances in cell biology and to the understanding of the formation and function of tissues, organs, as well as diseased states such as cancer. Most of these findings were elucidated using traditional 2D culture techniques, but biology is clearly a complex 3D system. 2D cell culture techniques do not faithfully replicate all of the mechanical and biochemical signals present in vivo[54]. In 2D techniques, cell-to-plastic interactions prevail rather than the crucial cell-to-cell and cell-to-extracellular matrix (ECM) interactions that form the basis for normal cell function[55]. Additionally, the plastic Petri dish is an unnaturally stiff substrate compared to the softer mechanical environment that cells experience in vivo which is well known to alter cell function.

In the absence of an attachment surface or scaffold, cells will aggregate and undergo the process of self-assembly. During self-assembly, mono-dispersed cells form 3D microtissues called multi-cellular spheroids (MCSs). Self-assembly mimics natural processes that occur during embryogenesis, morphogenesis and organogenesis[56-58] (**Figure 1-5**). Spheroids mimic the architectural and functional characteristics of native tissue such as cardiomyocyte spheroids that beat with heart-like rhythm, hepatocyte spheroids that have liver-like functionality, as well as human endothelial cells vascularizing fibroblast microtissues[59-62].

The in vivo-like microenvironment that the spheroid creates is the result of numerous factors including the formation of molecular gradients. Gradients of soluble

components in the cell culture medium (e.g., nutrients, oxygen, growth factors) as well as those produced by cells (e.g. metabolites, paracrine factors) are established due to the barriers to diffusion imposed by the spheroid, as well as the rates of consumption and production of these factors by the cells[63]. In addition to gradients, spheroids create an in vivo-like microenvironment by forming more complex cell-to-cell interactions and cell-to-ECM adhesions. These serve to simultaneously deliver additional signals including mechanical forces, biochemical signals and electrical coupling that can influence cell shape, motility, proliferation, and differentiation as well as gene expression[54, 64].

In this article, we do not review the entire field of 3D cell culture. Excellent comprehensive reviews and books can be found elsewhere. Much of this work is focused on culturing cells attached to and cast in various natural and synthetic scaffolds. Instead, we focus our review on multi-cellular spheroids formed without an attachment to a scaffold or gel. Cell-to-cell adhesion is one of the key driving forces of their formation. In most cases, these structures are termed spheroids due to their approximate spherical shape. However, other shapes are now possible, hence the term multi-cellular microtissues or simply microtissues. Regardless of how they are formed, spheroids and microtissues are all characterized by a very high density of cells, a density that more closely approximates that of normal organs or tissues. We discuss the techniques to form microtissues, their advantages and disadvantages, as well as uses of microtissues in basic biology, cancer research, tissue engineering and drug discovery.

1.5.2 Methods

1.5.2.1 Methods to Form Spheroids

1.5.2.1.1 Pellet Culture

The pellet culture technique uses centrifugal force to concentrate cells to the bottom of a tube maximizing the opportunity for cell-to-cell adhesions to form (**Figure 1-6A**). To form spheroids, a cell suspension in a tube with a conical bottom is centrifuged at a speed of 500g for 5 minutes[65]. To optimize this process, the cell suspension may be incubated on a shaker for one hour prior to centrifugation. Due to the ease of formation, pellet culture is often used to create spheroids to study chondrogenesis, and bone formation, and for the differentiation of mesenchymal stem cells[65-69]. While a large number of cells can aggregate rapidly, a disadvantage is the shear stress from centrifugation that can damage cells. This method is used to form spheroids of fairly large diameter which can create a low oxygen concentration in the center. For chondrocytes, differentiation is stimulated by low oxygen, but for other cells types, hypoxia can cause necrosis in the spheroid core [70, 71]. Additionally, while this method is simple and rapid to perform, it has not been scaled up for mass production of spheroids, nor can the cells be visualized as they aggregate.

1.5.2.1.2 Spinner Culture

The spinner culture method creates spheroids by preventing cells in suspension from settling and by promoting cell-to-cell collisions via constant stirring (**Figure 1-6B**)[72, 73]. To form spheroids, spinner flasks are seeded with a uniform, well mixed single cell suspension and the fluid environment and mass transfer in the flask is controlled by convective forces generated by an impeller or magnetic stir bar. Maintaining a constant rotation speed is critical. An agitation speed that is too slow will allow the spheroids to settle, but one that is too high will cause cell damage due to fluid shear stress. One advantage is that the fluid movement aids mass transport in and out of the spheroids.

Spinner culture has been used with a variety of primary cells, cell lines, and mixtures of two different cell types to form heterotypic spheroids[60, 74-76]. Spinner culture can be scaled up to produce large number of spheroids. By decreasing the agitation speed and allowing the cells to settle, culture conditions can be controlled through media changes and addition of drugs and growth factors. Due to shear forces, this method may not be useful for cells with low cohesiveness, cells that are sensitive to shear forces, or for adherent cells that may undergo apoptosis while in suspension. Due to constant mixing, cells cannot be visualized as they aggregate.

1.5.2.1.3 Hanging Drop

The hanging drop method relies on gravity-enforced self-assembly to produce spheroids[77]. To make spheroids, small volumes (20-30 μL) of a cell suspension are pipetted onto the inside lid of a tissue culture plate. The lid is inverted, and the drops stay attached to the lid due to surface tension. Gravity causes the cells to settle and concentrate at the bottom of the drop, and a single spheroid is formed[77, 78] (**Figure 1-6C**). A variety of cell types have formed spheroids using this method including both primary cells as well as cell lines[60]. Different cell types can be co-cultured to form heterotypic spheroids. Spheroid size and cellular composition is controlled by adjusting the cell density in each drop. Advances into high throughput production of spheroids using the hanging drop method have been established, producing up to 384 spheroids in a single array[79]. However, with this method, it is difficult to track these spheroids during formation and it is nontrivial to exchange media or add drugs.

1.5.2.1.4 Liquid Overlay

The liquid overlay method inhibits the attachment of cells to tissue culture plates and promotes cell-cell aggregation. In this method, a cell suspension is seeded onto flat

tissue culture dishes made of low-adhesive surfaces such as agarose[80, 81], and poly (2-hydroxethyl methacrylate) (pHEMA)[82] (**Figure 1-6D**). The plates are rocked and with a small amount of shaking, the cells aggregate into spheroids. Both primary cells and cell lines form spheroids using this method. While the method is easy, the spheroids are often heterogeneous in both size and shape. This technique, when performed in 96 well plates, allows for monitoring of individual spheroid formation and growth.

1.5.2.1.5 Rotating Wall Vessel

The rotating wall vessel creates a microgravity environment that maintains cells in suspension and allows cells to aggregate into spheroids. A cell suspension in a rotating wall vessel is slowly rotated about an x-axis maintaining the cells in continuous free fall (**Figure 1-6E**). Initially, rotation is very slow (~15 rpms), but as spheroids begin to form and the mass of the aggregates increase, rotation is increased to keep the aggregates in suspension (~25 rpms)[83]. Spheroids from both primary cells as well as a variety of cell lines have been formed using this method. Heterotypic spheroids can be formed by co-culture of different cell types. Long term culture is possible and culture conditions can be controlled by perfusion which is useful for controlling differentiation[84]. The method produces aggregates in a low shear environment. Although the yield is high, there can be variability in spheroid size. While some advances in tracking the aggregates have been made[85], it remains difficult to monitor the assembly of spheroids in real-time.

1.5.2.1.6 External Force

The external force method uses any force to concentrate mono-dispersed cells into a high density that facilitates cell aggregation. External forces used are electric fields, magnetic force, and ultrasound (**Figure 1-6F**). For electric fields, positive dielectrophoresis in a low conductivity iso-osmotic solution is used to concentrate cells[86]. For magnetic fields,

cells are incubated with magnetic cationic liposomes (MCLs) containing a magnetite core (Fe_3O_4) [87, 88]. After endocytosis, the cells can be formed into specific patterns using magnetic fields. For ultrasound, an ultrasound standing wave trap is used to concentrate cells and facilitate their aggregation[89]. Cell adhesion is often very nonspecific and it can be difficult to control spheroid size. The physiological changes to the cells caused by these external forces are not well characterized.

1.5.2.1.7 Cell Sheets

In addition to spheroids, multi-cellular cell sheets have been produced by culturing cells on a polymer, such as poly (N-isopropylacrylamide) (PNIPAAm), which is thermo-responsive. changing its hydrophilicity and hydrophobicity with a change in temperature[90]. Lowering the temperature to 20ºC for one hour causes the polymer to change from hydrophobic to hydrophilic, thus causing the release of a contiguous sheet of cells. To form spheroids, small cell sheets that have been released can be further incubated on a non-adhesive surface where they will compact and form spheroids (**Figure 1-6G**). The cell sheet method has been used with hepatocytes[90], endothelial cells[91], cardiomyocytes[92, 93], epithelial cells, and mesenchymal stem cells for use in cartilage engineering[94]. Additionally, co-culture of multiple cell types has been achieved by creating layers of cell sheets from different cell types, and then allowing the multi-layered sheet to assemble into a spheroid[91, 95].

1.5.2.1.8 Micro-fluidics

When using micro-fluidics, cells are flowed through a micro-channel network into micro-chambers where they are partitioned and exposed to micro-rotational flow that causes cells to aggregate[96] (**Figure 1-6H**). The method works for primary cells, cell lines, and co-culture of multiple cell types[97, 98]. Micro-fluidic devices allow for high throughput

production of size controlled spheroids for high throughput analysis, as many of these platforms are equipped with biosensors for real-time imaging and monitoring of the system[99, 100]. Additionally, the perfusion system allows for tight control of the fluid shear stresses and the concentration of soluble factors surrounding the spheroids[100, 101].

1.5.2.1.9 Micro-molded Nonadhesive Hydrogels

Micro-molded nonadhesive hydrogels have been used to form spheroids as well as microtissues with different shapes[102, 103]. This method uses computer aided design software and rapid prototyping to form micro-molds that contain an array of cylindrical pegs with rounded tops. Nonadhesive hydrogels (agarose or polyacrylamide) are then cast from these micro-molds (**Figure 1-6I**). After the micro-molded gels are seeded, the cells settle to the bottom of the recesses, are unable to attach to the nonadhesive hydrogel, and cell-to-cell interactions drive the formation of a single spheroid in each recess. This technology has been used to form spheroids using many different cell types including primary cells and cell lines from a variety of tissues including, skin, brain, ovary, liver, heart, and breast[62, 102, 104-106]. The method can be scaled up to create up to 822 spheroids in a single mold, with homogenous shape, size, and cell composition. These factors are easily controlled by adjusting the number of cells, and the ratio of the cell mixture seeded onto the micro-molded hydrogel. Cells can be imaged as they self-assemble and it's easy to change media and add drugs, antibodies, or growth factors. In addition to spheroids, micro-mold designs have been used to direct the self-assembly of cells to more complex shapes such as rods, toroids, or honeycombs[103] (**Figure 1-7A-E**).

1.5.2.2 Methods for Working with Spheroids

1.5.2.2.1 Imaging

3D spheroids are more challenging to image than thin flat cells grown on conventional 2D cultures, but they offer new opportunities for more high content biological information. The spherical structure of the spheroid with its radial symmetry provides opportunities for mapping cell functions to these gradient and 3D microenvironments.

All of the conventional methods of microscopy have been used to image spheroids. Scanning electron microscopy (SEM) has been used to obtain low and high resolution images of the surface of spheroids. Low resolution images reveal cell size, shape and organization on the surface, whereas high resolution images reveal important biological structures such as pores and micro-villi. Conventional brightfield, and phase contrast microscopy have been used to image the x and y dimensions of spheroids and time lapse has been used to view and quantify the self-assemble of spheroids and microtissues of other shapes[103]. Spheroids have a significant z dimension and so side view microscopy has been used to image spheroid height[107, 108]. Due to their thickness and lack of transparency, none of these methods are able to obtain adequate images of the interior of the spheroid.

To view their interior, spheroids have been fixed, sectioned and stained with a variety of conventional dyes (e.g., hematoxylin and eosin) antibodies, small molecules and fluorescent molecules. Images of these sections provide valuable information about a single slice through the interior of a spheroid. In some cases, serial sections of the same spheroid have been used to reconstruct 3D organization. As an alternative to these labor intensive approaches, confocal fluorescence microscopy has been used to obtain thin

optical sections of fluorescently stained spheroids. These images can be rendered to create a high resolution 3D reconstruction of the spheroid and it's interior. However, the maximum penetration depth of confocal microscopy is about 50□m. Two photon fluorescence microscopy overcomes this limitation and has been used to obtain optical sections and a high resolution 3D reconstruction of the entire spheroid. Recently, a new microscopy technique, light sheet based fluorescence microscopy (LSFM), has been used to image fluorescently labeled spheroids to produce a high resolution 3D reconstruction[54]. Our lab recently reported an easy method to use wide field fluorescent images to construct a 3D map of fluorescence on multiple spheroids as well time lapse data[108]. The method was used to quantify the kinetics of self-sorting that occurs when two different cell types self-assemble.

1.5.2.2.2 Assays for Spheroid Growth

Multiple methods have been used to quantify spheroid growth and the response to growth factors and drug treatments. Like, 2D cell culture, the enzymatic disaggregation of spheroids and the direct counting of cells has been used to quantify growth. However, the technique can be tedious and spheroids are difficult to disaggregate. Measuring the x, y dimension of spheroids from brightfield images has been used to quantify spheroid growth. Care must be taken since spheroids may appear to be near perfect spheres in conventional microscopy, when in fact, they are oblate spheroids whose z dimension can be less than their x, y dimensions. Colorimetric dyes, such as the tetrazolium salt WST-1 [2-(4-Iodophenyl)-3-(4-nitrophenyl)-5-(2, 4-disulfophenyl)-2H-tetrazolium], as well as measuring DNA content or ATP levels have been used to measure growth. To determine where cell proliferation occurs in 3D, spheroids have been sectioned or visualized via

confocal microscopy and immuno-stained for standard proliferation markers such as Ki-67 or bromodeoxyuridine labels.

1.5.2.2.3 Mathematical Modeling of Spheroids

Mathematical simulations have been developed to understand various aspects of spheroid formation and spheroid function. Self-assembly and the process of self-sorting that occurs when two different cell types segregate as they self-assemble has been modeled by several groups[109-111]. One such model, the differential adhesion hypothesis (DAH) posits that cell types self-segregate due to differences in cell-to-cell adhesion or apparent surface tension, with those cells of highest cohesion (like-to-like adhesion) sorting to the inside of a spheroid and those cells with lower cohesion sorting to the outside[56, 57, 73, 112]. Based on finite element computer simulations, the differential interfacial tension hypothesis (DITH) factors in contributions from cytoskeletal components and cell adhesion molecules[113]. Most recently, self-sorting has been modeled using an order parameter, which is based on a geometrically driven argument to describe the relationship between heterotypical interface length and the system size[114].

Mathematical models have also been formulated for cancer biology to describe the concentration gradients and the microenvironments formed in spheroids, as models of avascular tumors. These models propose mechanisms of tumor cell growth, differentiation, proliferation, and apoptosis based on the concentration of oxygen, nutrients, and metabolites at different radial points within the spheroid. Studies have correlated experimental data and simulations with the transcriptional activity of spheroids in hypoxic and normoxic conditions[115, 116]. Other models explain the mechanism by which cancer cells metastasize and continuum mathematics has been used to understand the mechanisms that control invasive cell behaviors[117]. Additional models simulate

cancer cell invasion by treating cells as individual units since invasion is thought to be created by interactions between single cells and their surrounding matrix[117-119].

Mathematical models have been developed for drug transport in spheroids. The diffusion distance of a drug in a monolayer of cells is short compared to in vivo tissues, whereas a drug must penetrate multi-layers of cells before reaching the center of a tumor[120]. Cells in monolayer do not adequately replicate the cell-to-cell interactions necessary to form well know bio-obstacles to drug transport such as tight junctions[121]. Lastly, it has been recognized for over 40 years that cancer cells grown in 2D are unusually sensitive to drug treatment than the same cells grown in 3D. Other models based on tumor spheroids have been used to quantify the effects of diffusion barriers in multi-layer tissues such as cellular compaction, gap junctions, and cellular efflux systems[122]. Advanced modeling predicts the pharmacokinetics of cancer drug candidates while accounting for the cellular determinants that affect these parameters[123].

1.5.3. Applications of Spheroids and Microtissues

1.5.3.1 Spheroids as Models for Basic Science

Self-assembly is thought to mimic naturally occurring processes and when two different cell types self-assemble, they often self-sort and compartmentalize to separate regions of the spheroid. This is similar to one cell population spreading over the other during morphogenesis and gastrulation. As so, microtissues produced via self-assembly have been used to elucidate the mechanisms of these phenomena in developmental biology[55, 124, 125].

The molecular events controlling self-assembly have been studied using spheroids. Cadherins are critical to self-assembly and varying levels of cadherins can control self-sorting, such that transfected cells with high cadherin levels sort to the center

of a spheroid, surrounded by cells with lower cadherin levels[56, 73]. In addition to cadherins, our lab has shown that connexins (Cx43), another surface adhesion molecule, helps mediate self-assembly[104]. Connexins form gap junctions that directly couple cells to one another and the adhesive function of gap junctions contributes to self-assembly on par with the adhesive effects of cadherins[104]. Recently, our lab has also shown that pannexin-1 (Panx1), a surface molecule with topographical similarities to connexins, controls self-assembly, but not via surface adhesion. Panx-1 forms channels that do not dock with other channels. Instead, Panx-1 channels act as pores leaking ATP which activates purinergic receptors (P_2X_7) causing actin reorganization via elevated calcium levels[105]. Our lab and others have shown that the cytoskeleton is an active player in self-assembly[107, 126, 127]. Drug targeting of actomyosin dependent cell tension (Y-27632, a rho kinase inhibitor) slows the rate of self-assembly and alters self-sorting[126]. Drugs that target myosin-2 (blebbistatin) and the actin network (cytochalasin, Y-27632) block or slow self-assembly of hepatocytes into functional tissue-like structures, and reduce liver-specific activities[127-129].

It is becoming increasingly clear that surface adhesion molecules and the cytoskeletal network act in concert to control self-assembly and self-sorting and that the mechanical forces of cell-to-cell interactions play a role in these processes[64]. Multi-cellular microtissues mimic the in vivo 3D mechano-environment and new designs in microtissues are useful for understanding normal as well as pathologic conditions of mechanobiology. Our lab recently reported an assay to quantify for the first time the forces of self-assembly[107]. Cells self-assembled a toroid-shaped microtissue that moved up a nonadhesive cone. The mass of the toroid and its rate of movement up the cone were

used to calculate cell power, the work expended in the process against the force of gravity. Toroids of fibroblasts exerted tenfold more power than toroids of hepatocytes, 4.3±1.7 pJ/hr and 0.31±0.01 pJ/hr, respectively. Moreover, drug targeting of actomyosin dependent cell tension resulted in a greater than 50% reduction in cell power for both cell types, demonstrating the crucial role of the cytoskeleton. In addition to quantifying the contribution of specific proteins and proteins systems, the toroid-on-cone assay is useful for understanding drug actions and how cell mixtures behave in a 3D mechanical environment[107]. Recently, the toroid-on-cone assay was used to quantify heterotypic cell mixtures and uncovered a new role for TGF-β1[130]. Another microtissue design used by our lab to investigate 3D cell mechanics is the loop ended dogbone[102]. The tensile forces of self-assembly in this mechanically constrained design cause fibroblasts to elongate over 30 times their initial diameter. These microtissues break due to these forces, but they can be stabilized by drugs that target the cytoskeleton (Y-27632 and blebbistatin a myosin II inhibitor).

1.5.3.2 Spheroids in Cancer Research and Drug Discovery

Tumor spheroids have been used as an in vitro model to mimic the complexity of tumors[131]. Mixed spheroids have been used to study tumor-stromal cell interactions and the cells in these mixed spheroids have a more in vivo cell shape, architecture, and gene expression profiles[132, 133]. For example, breast cancer cells co-cultured with fibroblasts showed an invasive phenotype and formed a tissue more similar to primary breast cancer tissue in terms of protein expression in the cancer cells (pancytokeratins, p53, E-cadherin) and the fibroblasts (vimentin) compared [134]. Three dimensional tumor-endothelial cell models have been used to measure the angiogenic and metastatic

potential of tumor cells and the presence of endothelial cells makes tumor cells more resistant to chemotherapy and radiation[135, 136].

One important use of spheroids is as a model for drug discovery and drug transport. Cancer cells are much more drug resistant when grown as spheroids versus monolayer[121]. For example, the IC_{50} of paclitaxel and cisplatin in spheroids is 100-fold higher than the IC_{50} in mono-layers of the same cells. Similar results have been found with antibodies, siRNA, and immunotoxins[137-140]. This result is, due in part, because of drug penetration, but also due to the cellular phenotype induced by differences in hypoxia, proliferation, cell-to-cell contacts, and gene expression at different locations within a spheroid, much like a tumor[141, 142]. Tumor spheroids have been used to measure drug penetration in 3D by using fluorescence of anthracyclines such as doxorubicin, or autoradiography of radio-labeled drugs[143, 144]. 3D models based on human cells have the potential to lead to high-throughput and high-content screening to predict the responsiveness of individual tumors to different therapy regimens.

1.5.3.3 Spheroids in Tissue Engineering

Spheroids are increasingly being used in tissue engineering for a variety of different organs and tissues[145]. Spheroids produced from primary rat and mouse cardiomyocytes, as well as a mixed population of cells, beat with a natural rhythm for up to three weeks because the cells are electrically coupled[146]. Self-assembled constructs of human chondrocytes, as well as pluripotent stem cells differentiated towards a chondrogenic lineage are under consideration for use in tissue engineering[147]. Compared to cells seeded on a matrix, spheroids of chondrocytes have histological, biochemical, and biomechanical properties more similar to native cartilage[148]. The mechanical properties of cartilage largely depend on the organization of extracellular matrix, and

self-assembled spheroids attain total collagen and sulfated glycosaminoglycans amounts closer to cartilage than those that made with cells on scaffolds[69, 149].

In addition to uses in toxicity testing, liver spheroids may have an application in a bioartificial liver device. Hepatocytes cultured in 2D lose differentiated function, but hepatocytes cultured as spheroids retain their polarity, form tight junctions, possess microvilli-lined channels that resemble bile canaliculi and have liver-like function[150]. Spheroids of the human cell line, HepG2, retained key detoxifying functions required of the liver. Co-culture of primary rat hepatocyte cells with hepatic stellate cells have liver like functionality for over 2 months in culture[151]. Spheroids of other complex tissues and organs have been formed. Pancreatic epithelial cells have been shown to self-assemble a hollow 3D structure [152, 153]. Dissociated cells from the retina self-assemble and self-sort to form distinct cell layers that resemble the retina's architecture complete with photo receptors[154].

1.5.3.4 Spheroids as Building Blocks

Presently, the biggest challenge to the field of tissue engineering is the in vitro fabrication of large tissue constructs with a high density of living cells, similar to natural organs [155, 156]. Nearly all of the clinical successes in tissue engineering are *relatively thin tissues (< 2 mm), where the transport of* oxygen, nutrients, and metabolic waste *critical for cell viability occurs by simple diffusion [155]. Likewise,* spheroid diameter is limited to 200-400 microns due to the constraints of diffusion. Human umbilical cord endothelial cells (HUVECs) have been used to coat spheroids and the endothelial cells migrate to the core and developed a capillary-like network[157]. These endothelialized spheroids have been fused to form a larger vascularized tissue that could integrate with the host vascular system after implantation[158]. Likewise, when human mesenchymal stem cells that were

differentiated towards an osteogenic lineage were mixed with HUVECs, they formed a pre-vascular network within 10 days[66, 159].

The emerging field of bio-printing and bio-fabrication is seeking to address the issue of large tissue constructs and is using spheroids as building blocks to try and fabricate organs in vitro. Bio-printers, adapted from inkjet printing and rapid prototyping technologies, have been used to fabricate living structures via a layer-by-layer printing of living cells along with an extracellular matrix (ECM) material [160-166]. Computer control of the deposition process in the x, y and z dimensions enables the fabrication of complex-shaped living structures, complete with the beginnings of a vascular tree. Spheroids loaded in a cartridge are printed as the "bio-ink" along with an ECM substrate which serves as the "bio-paper". After printing, spheroids attach to the ECM substrate and fuse with neighboring spheroids to form a contiguous 3D structure[164, 165]. Control over cell position with a building block is important when building large complex 3D structures[161, 167]. The relative position of different cell types within spheroids as well as spheroids that have been fused is beginning to be controlled. Likewise, endothelialized spheroids have been used to create microvessels after fusion and the relationship between spheroid size and capillary formation has also been investigated[168].

1.5.3.4 Microtissues with Complex Shapes as Building Blocks

We and others have investigated the use of building blocks of different shapes for the purpose of bio-fabrication. In addition to spheroids, multi-cellular sheets produced on a thermo-reponsive polymer have been used for numerous cell types including smooth muscle cells and cardiomyocytes[169]. Layers of cardiac cell sheets have been used to engineer functional 3D tissues that can be transplanted to improve cardiac function after

myocardial infarction[93]. Cell sheets have been wrapped around a mandrel to create a tubular structure and cell sheets have been layered to create a thicker tissue[170].

Non-adhesive micro-molds have been used to direct the self-assembly process so that cells form non-spherical multi-cellular microtissues[102, 103]. Micro-molds have been used to form microtissues in the shape of rods, toroids, loop-ended dogbones, and honeycombs (**Figure 1-7A-E**). Rod or cylinder shaped microtissues have also been used in micro-extrusion, a variation of bio-printing. Cylinder shaped microtissues loaded in a cartridge are slowly extruded and sliced into blocks that will round up into spheroids as a method to produce spheroid building blocks.

Non-adhesive micro-molds have also been used to produce more complex building blocks in the shape of a toroid[102]. These structures with high cell densities are interesting because they have a lumen, so cells are located within diffusion distance of a top /bottom surface or the surface of a lumen. Lumen diameter is initially controlled by micro-mold design and when multi-cellular toroids are harvested from the micro-molds, they undergo slow, but predictable changes to their shape and lumen diameter which can be used in their design as a building block[171]. Moreover, harvested toroids can fuse with one another in a process that is complete within 72 hours and toroids can be used as building units to make a large multi-layered multi-torus structure. In this fused structure, the lumens began to form an interconnected network of open space, mimetic of a vascular network[171]. Nonadhesive micro-molds have also been used to form a large honeycomb structure (2 cm), a single structure with rings of interconnected cells around lumens[172]. As a potential building unit, the honeycomb can be significantly larger in the *x* and y dimensions, while the cross section of the cellular portion of any part of the honeycomb

can be kept small, so as to not exceed the critical diffusion distance needed to maintain cell viability.

1.5.4 Summary and Conclusions

Multi-cellular spheroids provide many advantages over traditional monolayer culture of cells and have the potential to impact numerous facets of biomedical research. Although challenges exist when working with spheroids, they are promising in vitro models for basic and developmental biology, cancer biology, drug discovery and toxicology studies, as well as tissue engineering. These microtissues have proved to be realistic models of both normal and diseased tissues in vitro. While advances in spheroid formation, imaging, and assays to work with spheroids have been made, there is still a need for optimization and standardization of these protocols and development of more widely adopted endpoint analytical measurements.

1.5.5 Expert Opinion

There is little doubt that the biology and biochemistry of spheroids is significantly closer to natural tissues and organs than a thin monolayer of cells grown on a stiff plastic dish. This was first recognized over 40 years ago, when cancer cells grown in 2D were shown to be far more sensitive to radiation and drug treatment than spheroids, a result that more closely mimics the resistance of tumors in vivo. Nevertheless, 2D cell culture rapidly expanded its importance and is now widely adopted in all areas of biological research and drug discovery. The explosion in 2D cell culture was driven by the ease and convenience of culturing cells in 2D and easy methods to nourish, image, manipulate and assay cultured cells. Despite having more relevant biological information, spheroids have lagged behind 2D cell culture, because the methods for culturing spheroids were cumbersome, difficult to control and the assays as well as microscopy techniques to

analyze spheroids were equally difficult or nonexistent. New and more convenient methods have been developed for the formation of spheroids. It's now easy to produce large numbers of spheroids of uniform size, control the size of spheroids, produce spheroids of two or more different cell types, produce spheroids from tumor cells as well as normal human cells, and even produce spheroids that are not simple spheres. Multi-cellular toroids, rods and honeycombs are now possible. In addition to being straightforward and convenient, these methods have been adapted to high throughput formats. Moreover, advances in microscopy, fluorescent probes and biochemical assays have made spheroids more amenable to investigation. Thus, it's becoming easier to extract the rich biological content that multi-cellular spheroids can supply.

Spheroids have more biological information because they are a living assembly of cells that signal one another and actively respond to the signals they generate. As the cells aggregate, they move upon each other and pairs of cell types can even self-sort as they self-assemble or cells can form hollow spheres. They maximize cell-to-cell contact, form numerous adhesions between surface adhesion molecules and even form direct cell couplings such as gap junctions. They exert biomechanical forces that change the shape, cytoskeleton and function of the cells. They secrete biochemical signals that alter gene expression and cell function. They synthesize, secrete and assemble numerous extracellular matrix proteins in response to all these signals and this ECM also signals cells. They establish 3D gradients of nutrients, metabolites and cell signals as well as barriers to the transport of molecules. In short, the repertoire of cell functions in a multi-cellular spheroid is not constrained; cells are freed to assemble an in vivo-like 3D environment.

In contrast, 2D plastic substrates constrain the repertoire of cell functions. Cells adhere more strongly to the substrate than they do to each other. Cells spread to form a very thin and highly adherent monolayer whose shape is a poor replicate of cell shape in vivo. Cell-to-cell interactions and cell-to-cell signaling are minimized because attachment to the substrate dominates the 2D environment. Cells are exerting forces against and moving on an unyielding and unnaturally stiff substrate that is, from a biology perspective, unresponsive. This is true of cells on typical flat planar substrates or synthetic polymeric substrates that are in the form of fibers or foams. Likewise, the same is true, to some extent, for scaffolds or gels of natural proteins such as collagen or laminin. ECM bio-molecules do provide more biological information than synthetic polymers and cells will respond to these cues, but the information is not as dynamic, nor as biologically complex, as the exchange of signals that occurs when cells are in direct contact. Moreover, the bio-molecules in these scaffolds are often in random organizations, whereas the ECM produced by cells in contact with other cells is influenced by the mechanical and biochemical signals emanating from surrounding cells. Thus, multi-cellular spheroids are superior replicas of the in vivo environment because they maximize the cell-to-cell interactions that elicit the greatest repertoire of cell functions. Non-living substrates, (synthetic and natural) that interfere with cell-to-cell interactions can constrain cells, thereby limiting the repertoire of cell functions.

The new methods of forming spheroids and microtissues are expanding their use and driving new applications. By addressing the limitations and constraints to the biology of cells cultured on plastic, microtissues are beginning to emerge as more realistic and more predictive platforms for in vitro toxicity testing and drug discovery.

The use of mixed spheroids with two or more different cell types is an especially exciting development because it takes another step closer to the in vivo environment . The robust biology of microtissues will also impact the fields of cell transplantation and tissue engineering by providing a stable and functional unit suitable for transplantation or use as building blocks for the biofabrication of larger tissue constructs.

1.5.6 Article Highlights

- 3D spheroids produced via self-assembly, in a scaffold-free environment, mimic the function and architecture of in vivo tissues making them important in vitro models.
- New and more convenient methods to produce spheroids have expanded their use in biomedical research.
- In addition to producing spheroids, non-adhesive micromolds can direct the self-assembly of microtissues with complex shapes, creating new opportunities.
- New biochemical assays and microscopy techniques have been developed to image and analyze 3D spheroids.
- Spheroids are commonly used in cancer biology to understand cancer-stromal cell interactions and mechanisms of cancer metastasis.
- Mathematical models are being used to understand how cells aggregate and self assemble as well as how drugs diffuse into spheroids.
- Due to their high biological content, spheroids are being used in high-throughput and high-content formats for toxicology testing and drug discovery.
- Spheroids with tissue specific functionalities have been produced for cardiac, cartilage, bone, hepatic and pancreatic tissues.

- Advances have been made in vascularizing spheroids, but this remains a major challenge to the field of tissue engineering.
- Spheroids and microtissues with complex shapes are being used as building blocks for fabricating large tissue constructs.

1.6 Specific Aims

Specific Aim 1 - To develop an assay to quantify fluorescence in 3D microtissues using wide-field fluorescent microscopy.

3D microtissues are superior to mono-layers of cells grown in 2D because 3D better replicates tissue function and also replicates the natural microenvironments of in vivo tissues and organs.3D microtissues replicate gradients of nutrients, metabolic waste products, and oxygen better than a thin layer of 2D cells. 3D also replicates the cellular barriers and obstacles to drug diffusion that are important for a drug's efficacy.

With the growing use of 3D cell culture methods, and their increasing importance, there is a need for new *in vitro* quantitative methods of analysis needed when working with these cultures, as analysis is often rate limiting. As for microscopy, there is a need to measure and calculate the concentration of a fluorescent molecule at any point in the 3D volume of a 3D microtissue. It would be desirable to use wide-fluorescent images of 3D microtissues, to extract reliable quantitative information to measure and predict the concentration of a fluorescent molecule at any point in the volume of the 3D microtissue.

Specific Aim 2 – To quantify the effect of transport pump inhibition on the uptake, transport, and penetration through 3D microtissues.

Drug uptake, transport, diffusion and elimination from tissues are important properties governing the efficacy and potential toxicity of drugs and drug candidates. Efflux transporters, such as Pgp, are well-known regulators of drug bioavailability and their modulation, either intentionally via inhibitors or unintentionally via the side effects of certain drugs, can have profound pharmacological effects. Some efflux transporters can be up-regulated by solid tumors causing multi-drug resistance, so there is an active interest to identify more effective inhibitors for use in chemotherapy. Thus, there is a need for new *in vitro* models to predict drug toxicity and unwanted drug-drug interactions

and a need for models to discover new and more effective inhibitors of efflux transporters associated with multi-drug resistance. Although mono-layers of cells have been useful for defining some of these transport parameters and have been used to identify inhibitors of efflux pumps, such as Pgp.

There is growing recognition that 2D cell culture may not adequately replicate the biological complexities of the 3D *in vivo* environment. A quantitative assay to measure the uptake and transport through 3D microtissues would be useful to the field, and with the potential to be more effective at predicting the effects of efflux pump inhibitors to be used in the clinic.

Specific Aim 3 - To quantify the elimination rate of transporter substrates out of 3D microtissues.

It is well understood that the efficacy of a drug depends on its ability to reach its target at the desired concentration. And, drug concentration within a tissue is limited not only by the ability of the drug to enter and transport through the tissue, but also by how fast it is eliminated from the tissue. Drug efflux transporters, in particular P-glycoprotein (Pgp) of the ATP-Binding Cassette transporters are highly expressed in tissues critical for drug ADME-TOX, and act as a barrier to uptake and penetration while also acting to increase the rate of elimination. Pgp is highly expressed in the epithelia of the intestine, liver, and kidney, and also endothelium of the blood-brain barrier. This expression impacts the pharmacological behavior of all drugs by limiting uptake and penetration into tissues and effecting the oral bioavailability, intestinal absorption, hepatobilliary and urinary excretion. The disposition of a large number of drugs is modulated by Pgp and efflux transporters since their substrates include a broad range of chemically diverse substrates used for a variety of therapeutic applications. Since the ADME-TOX is crucial

to the clinical success of a drug, early in vitro screening in drug discovery is needed to select against drugs that negatively affect ADME-TOX, or that can predict the potential of clinically significant drug-transporter and drug-drug interaction yet still prove effective.

Thus, there is a need for new quantitative *in vitro* screening assays to better predict the *in vivo* actions of new drug candidates and their elimination from specific tissues or organs, which could be addressed using 3D microtissues, to better mimic the tissue geometries and complexities of the body. 3D tissues also has the potential of studying the effect of mixed cell populations, within one aggregate, to these processes.

1.7 References

1. Chen CJ, Chin JE, Ueda K, Clark DP, Pastan I, Gottesman MM, Roninson IB. Internal Duplication and Homology with Bacterial Transport Proteins in the Mdr1 (P-Glycoprotein) Gene from Multidrug-Resistant Human Cells. *Cell* **1986**;*47* 381-389.

2. Kuwano M, Toh S, Uchiumi T, Takano H, Kohno K, Wada M. Multidrug Resistance-Associated Protein Subfamily Transporters and Drug Resistance. *Anti-cancer drug design* **1999**;*14* 123-131.

3. Smith PC, Karpowich N, Millen L, Moody JE, Rosen J, Thomas PJ, Hunt JF. Atp Binding to the Motor Domain from an Abc Transporter Drives Formation of a Nucleotide Sandwich Dimer. *Molecular cell* **2002**;*10* 139-149.

4. Aller SG, Yu J, Ward A, Weng Y, Chittaboina S, Zhuo R, Harrell PM, Trinh YT, Zhang Q, Urbatsch IL, Chang G. Structure of P-Glycoprotein Reveals a Molecular Basis for Poly-Specific Drug Binding. *Science* **2009**;*323* 1718-1722.

5. Higgins CF, Linton KJ. The Atp Switch Model for Abc Transporters. *Nature structural & molecular biology* **2004**;*11* 918-926.

6. Linton KJ. Structure and Function of Abc Transporters. *Physiology (Bethesda)* **2007**;*22* 122-130.

7. Loo TW, Bartlett MC, Clarke DM. Substrate-Induced Conformational Changes in the Transmembrane Segments of Human P-Glycoprotein. Direct Evidence for the Substrate-Induced Fit Mechanism for Drug Binding. *The Journal of biological chemistry* **2003**;*278* 13603-13606.

8. Juliano RL, Ling V. A Surface Glycoprotein Modulating Drug Permeability in Chinese Hamster Ovary Cell Mutants. *Biochimica et biophysica acta* **1976**;*455* 152-162.

9. Flens MJ, Zaman GJ, van der Valk P, Izquierdo MA, Schroeijers AB, Scheffer GL, van der Groep P, de Haas M, Meijer CJ, Scheper RJ. Tissue Distribution of the Multidrug Resistance Protein. *The American journal of pathology* **1996**;*148* 1237-1247.

10. Goldman B. Multidrug Resistance: Can New Drugs Help Chemotherapy Score against Cancer? *Journal of the National Cancer Institute* **2003**;*95* 255-257.

11. Gottesman MM, Fojo T, Bates SE. Multidrug Resistance in Cancer: Role of Atp-Dependent Transporters. *Nature reviews. Cancer* **2002**;*2* 48-58.

12. Gottesman MM, Pastan I, Ambudkar SV. P-Glycoprotein and Multidrug Resistance. *Current opinion in genetics & development* **1996**;*6* 610-617.

13. Minotti G, Menna P, Salvatorelli E, Cairo G, Gianni L. Anthracyclines: Molecular Advances and Pharmacologic Developments in Antitumor Activity and Cardiotoxicity. *Pharmacological reviews* **2004**;*56* 185-229.

14. Tsuruo T, Iida H, Tsukagoshi S, Sakurai Y. Overcoming of Vincristine Resistance in P388 Leukemia in Vivo and in Vitro through Enhanced Cytotoxicity of Vincristine and Vinblastine by Verapamil. *Cancer research* **1981**;*41* 1967-1972.

15. Ho RH, Kim RB. Transporters and Drug Therapy: Implications for Drug Disposition and Disease. *Clinical pharmacology and therapeutics* **2005**;*78* 260-277.

16. Theis JG, Chan HS, Greenberg ML, Malkin D, Karaskov V, Moncica I, Koren G, Doyle J. Assessment of Systemic Toxicity in Children Receiving Chemotherapy with Cyclosporine for Sarcoma. *Medical and pediatric oncology* **2000**;*34* 242-249.

17. Ferry DR, Traunecker H, Kerr DJ. Clinical Trials of P-Glycoprotein Reversal in Solid Tumours. *Eur J Cancer* **1996**;*32A* 1070-1081.

18. Szakacs G, Varadi A, Ozvegy-Laczka C, Sarkadi B. The Role of Abc Transporters in Drug Absorption, Distribution, Metabolism, Excretion and Toxicity (Adme-Tox). *Drug discovery today* **2008**;*13* 379-393.

19. Williams JA, Bauman J, Cai H, Conlon K, Hansel S, Hurst S, Sadagopan N, Tugnait M, Zhang L, Sahi J. In Vitro Adme Phenotyping in Drug Discovery: Current Challenges and Future Solutions. *Current opinion in drug discovery & development* **2005**;*8* 78-88.

20. Dietrich CG, Geier A, Oude Elferink RP. Abc of Oral Bioavailability: Transporters as Gatekeepers in the Gut. *Gut* **2003**;*52* 1788-1795.

21. Chan LM, Lowes S, Hirst BH. The Abcs of Drug Transport in Intestine and Liver: Efflux Proteins Limiting Drug Absorption and Bioavailability. *European journal of pharmaceutical sciences : official journal of the European Federation for Pharmaceutical Sciences* **2004**;*21* 25-51.

22. Varma MV, Perumal OP, Panchagnula R. Functional Role of P-Glycoprotein in Limiting Peroral Drug Absorption: Optimizing Drug Delivery. *Current opinion in chemical biology* **2006**;*10* 367-373.

23. Leslie EM, Deeley RG, Cole SP. Multidrug Resistance Proteins: Role of P-Glycoprotein, Mrp1, Mrp2, and Bcrp (Abcg2) in Tissue Defense. *Toxicology and applied pharmacology* **2005**;*204* 216-237.

24. Gibson CJ, Hossain MM, Richardson JR, Aleksunes LM. Inflammatory Regulation of Atp Binding Cassette Efflux Transporter Expression and Function in Microglia. *The Journal of pharmacology and experimental therapeutics* **2012**;*343* 650-660.

25. Breedveld P, Beijnen JH, Schellens JH. Use of P-Glycoprotein and Bcrp Inhibitors to Improve Oral Bioavailability and Cns Penetration of Anticancer Drugs. *Trends in pharmacological sciences* **2006**;*27* 17-24.

26. Elferink RO, Groen AK. Genetic Defects in Hepatobiliary Transport. *Biochimica et biophysica acta* **2002**;*1586* 129-145.

27. Xia CQ, Milton MN, Gan LS. Evaluation of Drug-Transporter Interactions Using in Vitro and in Vivo Models. *Current drug metabolism* **2007**;*8* 341-363.

28. Peng SX, Ritchie DM, Cousineau M, Danser E, Dewire R, Floden J. Altered Oral Bioavailability and Pharmacokinetics of P-Glycoprotein Substrates by Coadministration of Biochanin A. *Journal of pharmaceutical sciences* **2006**;*95* 1984-1993.

29. Sarkadi B, Homolya L, Szakacs G, Varadi A. Human Multidrug Resistance Abcb and Abcg Transporters: Participation in a Chemoimmunity Defense System. *Physiological reviews* **2006**;*86* 1179-1236.

30. Perez-Tomas R. Multidrug Resistance: Retrospect and Prospects in Anti-Cancer Drug Treatment. *Current medicinal chemistry* **2006**;*13* 1859-1876.

31. Goldstein LJ, Galski H, Fojo A, Willingham M, Lai SL, Gazdar A, Pirker R, Green A, Crist W, Brodeur GM, et al. Expression of a Multidrug Resistance Gene in Human Cancers. *Journal of the National Cancer Institute* **1989**;*81* 116-124.

32. Trock BJ, Leonessa F, Clarke R. Multidrug Resistance in Breast Cancer: A Meta-Analysis of Mdr1/Gp170 Expression and Its Possible Functional Significance. *Journal of the National Cancer Institute* **1997**;*89* 917-931.

33. Vecchio SD, Ciarmiello A, Potena MI, Carriero MV, Mainolfi C, Botti G, Thomas R, Cerra M, D'Aiuto G, Tsuruo T, Salvatore M. In Vivo Detection of Multidrug-Resistant (Mdr1) Phenotype by Technetium-99m Sestamibi Scan in Untreated Breast Cancer Patients. *European journal of nuclear medicine* **1997**;*24* 150-159.

34. Izquierdo MA, van der Zee AG, Vermorken JB, van der Valk P, Belien JA, Giaccone G, Scheffer GL, Flens MJ, Pinedo HM, Kenemans P, et al. Drug Resistance-Associated Marker Lrp for Prediction of Response to Chemotherapy and Prognoses in Advanced Ovarian Carcinoma. *Journal of the National Cancer Institute* **1995**;*87* 1230-1237.

35. Schneider J, Jimenez E, Marenbach K, Marx D, Meden H. Co-Expression of the Mdr1 Gene and Hsp27 in Human Ovarian Cancer. *Anticancer research* **1998**;*18* 2967-2971.

36. Chan HS, Thorner PS, Haddad G, Ling V. Immunohistochemical Detection of P-Glycoprotein: Prognostic Correlation in Soft Tissue Sarcoma of Childhood. *Journal of clinical oncology : official journal of the American Society of Clinical Oncology* **1990**;*8* 689-704.

37. Green SK, Frankel A, Kerbel RS. Adhesion-Dependent Multicellular Drug Resistance. *Anti-cancer drug design* **1999**;*14* 153-168.

38. Durand RE, Olive PL. Resistance of Tumor Cells to Chemo- and Radiotherapy Modulated by the Three-Dimensional Architecture of Solid Tumors and Spheroids. *Methods in cell biology* **2001**;*64* 211-233.

39. Ambudkar SV, Dey S, Hrycyna CA, Ramachandra M, Pastan I, Gottesman MM. Biochemical, Cellular, and Pharmacological Aspects of the Multidrug Transporter. *Annual review of pharmacology and toxicology* **1999**;*39* 361-398.

40. Schuetz EG, Beck WT, Schuetz JD. Modulators and Substrates of P-Glycoprotein and Cytochrome P4503a Coordinately up-Regulate These Proteins in Human Colon Carcinoma Cells. *Molecular pharmacology* **1996**;*49* 311-318.

41. Bartlett NL, Lum BL, Fisher GA, Brophy NA, Ehsan MN, Halsey J, Sikic BI. Phase I Trial of Doxorubicin with Cyclosporine as a Modulator of Multidrug Resistance. *Journal of clinical oncology : official journal of the American Society of Clinical Oncology* **1994**;*12* 835-842.

42. Advani R, Fisher GA, Lum BL, Hausdorff J, Halsey J, Litchman M, Sikic BI. A Phase I Trial of Doxorubicin, Paclitaxel, and Valspodar (Psc 833), a Modulator of Multidrug Resistance. *Clinical cancer research : an official journal of the American Association for Cancer Research* **2001**;*7* 1221-1229.

43. Fracasso PM, Brady MF, Moore DH, Walker JL, Rose PG, Letvak L, Grogan TM, McGuire WP. Phase Ii Study of Paclitaxel and Valspodar (Psc 833) in Refractory Ovarian Carcinoma: A Gynecologic Oncology Group Study. *Journal of clinical oncology : official journal of the American Society of Clinical Oncology* **2001**;*19* 2975-2982.

44. Brouwer KL, Keppler D, Hoffmaster KA, Bow DA, Cheng Y, Lai Y, Palm JE, Stieger B, Evers R. In Vitro Methods to Support Transporter Evaluation in Drug Discovery and Development. *Clinical pharmacology and therapeutics* **2013**;*94* 95-112.

45. Li AP. Screening for Human Adme/Tox Drug Properties in Drug Discovery. *Drug discovery today* **2001**;*6* 357-366.

46. Varma MV, Ashokraj Y, Dey CS, Panchagnula R. P-Glycoprotein Inhibitors and Their Screening: A Perspective from Bioavailability Enhancement. *Pharmacological research : the official journal of the Italian Pharmacological Society* **2003**;*48* 347-359.

47. Homolya L, Hollo Z, Germann UA, Pastan I, Gottesman MM, Sarkadi B. Fluorescent Cellular Indicators Are Extruded by the Multidrug Resistance Protein. *The Journal of biological chemistry* **1993**;*268* 21493-21496.

48. Deeley RG, Westlake C, Cole SP. Transmembrane Transport of Endo- and Xenobiotics by Mammalian Atp-Binding Cassette Multidrug Resistance Proteins. *Physiological reviews* **2006**;*86* 849-899.

49. Adachi Y, Suzuki H, Sugiyama Y. Comparative Studies on in Vitro Methods for Evaluating in Vivo Function of Mdr1 P-Glycoprotein. *Pharmaceutical research* **2001**;*18* 1660-1668.

50. Yamazaki M, Neway WE, Ohe T, Chen I, Rowe JF, Hochman JH, Chiba M, Lin JH. In Vitro Substrate Identification Studies for P-Glycoprotein-Mediated Transport: Species Difference and Predictability of in Vivo Results. *The Journal of pharmacology and experimental therapeutics* **2001**;*296* 723-735.

51. Rautio J, Humphreys JE, Webster LO, Balakrishnan A, Keogh JP, Kunta JR, Serabjit-Singh CJ, Polli JW. In Vitro P-Glycoprotein Inhibition Assays for Assessment of Clinical Drug Interaction Potential of New Drug Candidates: A Recommendation for Probe Substrates. *Drug metabolism and disposition: the biological fate of chemicals* **2006**;*34* 786-792.

52. Lee CH. Differential Regulation of P-Glycoprotein Genes in Primary Rat Hepatocytes by Collagen Sandwich and Drugs. *Journal of cellular biochemistry* **2002**;*86* 12-20.

53. Lepist EI, Gillies H, Smith W, Hao J, Hubert C, St Claire RL, 3rd, Brouwer KR, Ray AS. Evaluation of the Endothelin Receptor Antagonists Ambrisentan, Bosentan, Macitentan, and Sitaxsentan as Hepatobiliary Transporter Inhibitors and Substrates in Sandwich-Cultured Human Hepatocytes. *PloS one* **2014**;*9* e87548.

54. Pampaloni F, Reynaud EG, Stelzer EH. The Third Dimension Bridges the Gap between Cell Culture and Live Tissue. *Nat Rev Mol Cell Biol* **2007**;*8* 839-845.

55. Kleinman HK, Philp D, Hoffman MP. Role of the Extracellular Matrix in Morphogenesis. *Curr Opin Biotechnol* **2003**;*14* 526-532.

56. Duguay D, Foty RA, Steinberg MS. Cadherin-Mediated Cell Adhesion and Tissue Segregation: Qualitative and Quantitative Determinants. *Dev Biol* **2003**;*253* 309-323.

57. Foty RA, Pfleger CM, Forgacs G, Steinberg MS. Surface Tensions of Embryonic Tissues Predict Their Mutual Envelopment Behavior. *Development* **1996**;*122* 1611-1620.

58. Moscona A, Moscona H. The Dissociation and Aggregation of Cells from Organ Rudiments of the Early Chick Embryo. *J Anat* **1952**;*86* 287-301.

59. Fukuda J, Nakazawa K. Orderly Arrangement of Hepatocyte Spheroids on a Microfabricated Chip. *Tissue Eng* **2005**;*11* 1254-1262.

60. Kelm JM, Fussenegger M. Microscale Tissue Engineering Using Gravity-Enforced Cell Assembly. *Trends Biotechnol* **2004**;*22* 195-202.

61. Kunz-Schughart LA, Schroeder JA, Wondrak M, van Rey F, Lehle K, Hofstaedter F, Wheatley DN. Potential of Fibroblasts to Regulate the Formation of Three-Dimensional Vessel-Like Structures from Endothelial Cells in Vitro. *Am J Physiol Cell Physiol* **2006**;*290* C1385-1398.

62. Desroches BR, Zhang, P., Choi, B., King, M.E., Maldonado, A.E., Li, W., Rago, A., Liu, G.X., Nath, N., Hartmann, K.M., Yang, B., Koren, G., Morgan, J.R., Mende, U. Functional Scaffold-Free 3d Cardiac Microtissues: A Novel Model for the Investigation of Heart Cells. *Am. J of Physiol.* **2012**.

63. Griffith LG, Swartz MA. Capturing Complex 3d Tissue Physiology in Vitro. *Nat Rev Mol Cell Biol* **2006**;*7* 211-224.

64. Pedersen JA, Swartz MA. Mechanobiology in the Third Dimension. *Ann Biomed Eng* **2005**;*33* 1469-1490.

65. Li J, He F, Pei M. Creation of an in Vitro Microenvironment to Enhance Human Fetal Synovium-Derived Stem Cell Chondrogenesis. *Cell Tissue Res* **2011**;*345* 357-365.

66. Rouwkema J, de Boer J, Van Blitterswijk CA. Endothelial Cells Assemble into a 3-Dimensional Prevascular Network in a Bone Tissue Engineering Construct. *Tissue Eng* **2006**;*12* 2685-2693.

67. Qihao Z, Xigu C, Guanghui C, Weiwei Z. Spheroid Formation and Differentiation into Hepatocyte-Like Cells of Rat Mesenchymal Stem Cell Induced by Co-Culture with Liver Cells. *DNA Cell Biol* **2007**;*26* 497-503.

68. Jahn K, Richards RG, Archer CW, Stoddart MJ. Pellet Culture Model for Human Primary Osteoblasts. *Eur Cell Mater* **2010**;*20* 149-161.

69. Giovannini S, Diaz-Romero J, Aigner T, Heini P, Mainil-Varlet P, Nesic D. Micromass Co-Culture of Human Articular Chondrocytes and Human Bone Marrow Mesenchymal Stem Cells to Investigate Stable Neocartilage Tissue Formation in Vitro. *Eur Cell Mater* **2010**;*20* 245-259.

70. Schrobback K, Klein TJ, Crawford R, Upton Z, Malda J, Leavesley DI. Effects of Oxygen and Culture System on in Vitro Propagation and Redifferentiation of Osteoarthritic Human Articular Chondrocytes. *Cell Tissue Res* **2011**.

71. Markway BD, Tan GK, Brooke G, Hudson JE, Cooper-White JJ, Doran MR. Enhanced Chondrogenic Differentiation of Human Bone Marrow-Derived Mesenchymal Stem Cells in Low Oxygen Environment Micropellet Cultures. *Cell Transplant* **2010**;*19* 29-42.

72. Castaneda F, Kinne RK. Short Exposure to Millimolar Concentrations of Ethanol Induces Apoptotic Cell Death in Multicellular Hepg2 Spheroids. *J Cancer Res Clin Oncol* **2000**;*126* 305-310.

73. Foty RA, Steinberg MS. The Differential Adhesion Hypothesis: A Direct Evaluation. *Dev Biol* **2005**;*278* 255-263.

74. Nyberg SL, Hardin J, Amiot B, Argikar UA, Remmel RP, Rinaldo P. Rapid, Large-Scale Formation of Porcine Hepatocyte Spheroids in a Novel Spheroid Reservoir Bioartificial Liver. *Liver Transpl* **2005**;*11* 901-910.

75. Frith JE, Thomson B, Genever PG. Dynamic Three-Dimensional Culture Methods Enhance Mesenchymal Stem Cell Properties and Increase Therapeutic Potential. *Tissue engineering. Part C, Methods* **2010**;*16* 735-749.

76. Han Y, Liu XM, Liu H, Li SC, Wu BC, Ye LL, Wang QW, Chen ZL. Cultivation of Recombinant Chinese Hamster Ovary Cells Grown as Suspended Aggregates in Stirred Vessels. *J Biosci Bioeng* **2006**;*102* 430-435.

77. Kelm JM, Timmins NE, Brown CJ, Fussenegger M, Nielsen LK. Method for Generation of Homogeneous Multicellular Tumor Spheroids Applicable to a Wide Variety of Cell Types. *Biotechnol Bioeng* **2003**;*83* 173-180.

78. Timmins NE, Nielsen LK. Generation of Multicellular Tumor Spheroids by the Hanging-Drop Method. *Methods Mol Med* **2007**;*140* 141-151.

79. Tung YC, Hsiao AY, Allen SG, Torisawa YS, Ho M, Takayama S. High-Throughput 3d Spheroid Culture and Drug Testing Using a 384 Hanging Drop Array. *Analyst* **2011**;*136* 473-478.

80. Enmon RM, Jr., O'Connor KC, Lacks DJ, Schwartz DK, Dotson RS. Dynamics of Spheroid Self-Assembly in Liquid-Overlay Culture of Du 145 Human Prostate Cancer Cells. *Biotechnol Bioeng* **2001**;*72* 579-591.

81. Metzger W, Sossong D, Bachle A, Putz N, Wennemuth G, Pohlemann T, Oberringer M. The Liquid Overlay Technique Is the Key to Formation of Co-Culture Spheroids Consisting of Primary Osteoblasts, Fibroblasts and Endothelial Cells. *Cytotherapy* **2011**;*13* 1000-1012.

82. Landry J, Bernier D, Ouellet C, Goyette R, Marceau N. Spheroidal Aggregate Culture of Rat Liver Cells: Histotypic Reorganization, Biomatrix Deposition, and Maintenance of Functional Activities. *J Cell Biol* **1985**;*101* 914-923.

83. Ingram M, Techy GB, Saroufeem R, Yazan O, Narayan KS, Goodwin TJ, Spaulding GF. Three-Dimensional Growth Patterns of Various Human Tumor Cell Lines in Simulated Microgravity of a Nasa Bioreactor. *In Vitro Cell Dev Biol Anim* **1997**;*33* 459-466.

84. Carpenedo RL, Sargent CY, McDevitt TC. Rotary Suspension Culture Enhances the Efficiency, Yield, and Homogeneity of Embryoid Body Differentiation. *Stem Cells* **2007**;*25* 2224-2234.

85. Manley P, Lelkes PI. A Novel Real-Time System to Monitor Cell Aggregation and Trajectories in Rotating Wall Vessel Bioreactors. *J Biotechnol* **2006**;*125* 416-424.

86. Sebastian A, Buckle AM, Markx GH. Tissue Engineering with Electric Fields: Immobilization of Mammalian Cells in Multilayer Aggregates Using Dielectrophoresis. *Biotechnol Bioeng* **2007**;*98* 694-700.

87. Ino K, Okochi M, Honda H. Application of Magnetic Force-Based Cell Patterning for Controlling Cell-Cell Interactions in Angiogenesis. *Biotechnol Bioeng* **2009**;*102* 882-890.

88. Okochi M, Takano S, Isaji Y, Senga T, Hamaguchi M, Honda H. Three-Dimensional Cell Culture Array Using Magnetic Force-Based Cell Patterning for Analysis of Invasive Capacity of Balb/3t3/V-Src. *Lab Chip* **2009**;*9* 3378-3384.

89. Liu J, Kuznetsova LA, Edwards GO, Xu J, Ma M, Purcell WM, Jackson SK, Coakley WT. Functional Three-Dimensional Hepg2 Aggregate Cultures Generated from an Ultrasound Trap: Comparison with Hepg2 Spheroids. *Journal of cellular biochemistry* **2007**;*102* 1180-1189.

90. Park KH, Na K, Kim SW, Jung SY, Chung HM. Phenotype of Hepatocyte Spheroids Behavior within Thermo-Sensitive Poly(Nipaam-Co-Peg-G-Grgds) Hydrogel as a Cell Delivery Vehicle. *Biotechnol Lett* **2005**;*27* 1081-1086.

91. Harimoto M, Yamato M, Hirose M, Takahashi C, Isoi Y, Kikuchi A, Okano T. Novel Approach for Achieving Double-Layered Cell Sheets Co-Culture: Overlaying Endothelial Cell Sheets onto Monolayer Hepatocytes Utilizing Temperature-Responsive Culture Dishes. *J Biomed Mater Res* **2002**;*62* 464-470.

92. Shimizu T, Yamato M, Isoi Y, Akutsu T, Setomaru T, Abe K, Kikuchi A, Umezu M, Okano T. Fabrication of Pulsatile Cardiac Tissue Grafts Using a Novel 3-Dimensional Cell Sheet Manipulation Technique and Temperature-Responsive Cell Culture Surfaces. *Circulation research* **2002**;*90* e40.

93. Sekine H, Shimizu T, Dobashi I, Matsuura K, Hagiwara N, Takahashi M, Kobayashi E, Yamato M, Okano T. Cardiac Cell Sheet Transplantation Improves Damaged Heart Function Via Superior Cell Survival in Comparison with Dissociated Cell Injection. *Tissue Eng Part A* **2011**;*17* 2973-2980.

94. Collett J, Crawford A, Hatton PV, Geoghegan M, Rimmer S. Thermally Responsive Polymeric Hydrogel Brushes: Synthesis, Physical Properties and Use for the Culture of Chondrocytes. *J R Soc Interface* **2007**;*4* 117-126.

95. Williams C, Xie AW, Yamato M, Okano T, Wong JY. Stacking of Aligned Cell Sheets for Layer-by-Layer Control of Complex Tissue Structure. *Biomaterials* **2011**;*32* 5625-5632.

96. Okuyama T, Yamazoe H, Mochizuki N, Khademhosseini A, Suzuki H, Fukuda J. Preparation of Arrays of Cell Spheroids and Spheroid-Monolayer Cocultures within a Microfluidic Device. *J Biosci Bioeng* **2010**;*110* 572-576.

97. Huang CP, Lu J, Seon H, Lee AP, Flanagan LA, Kim HY, Putnam AJ, Jeon NL. Engineering Microscale Cellular Niches for Three-Dimensional Multicellular Co-Cultures. *Lab Chip* **2009**;*9* 1740-1748.

98. Hsiao AY, Torisawa YS, Tung YC, Sud S, Taichman RS, Pienta KJ, Takayama S. Microfluidic System for Formation of Pc-3 Prostate Cancer Co-Culture Spheroids. *Biomaterials* **2009**;*30* 3020-3027.

99. Jin HJ, Cho YH, Gu JM, Kim J, Oh YS. A Multicellular Spheroid Formation and Extraction Chip Using Removable Cell Trapping Barriers. *Lab Chip* **2011**;*11* 115-119.

100. Agastin S, Giang UB, Geng Y, Delouise LA, King MR. Continuously Perfused Microbubble Array for 3d Tumor Spheroid Model. *Biomicrofluidics* **2011**;*5* 24110.

101. Toh YC, Zhang C, Zhang J, Khong YM, Chang S, Samper VD, van Noort D, Hutmacher DW, Yu H. A Novel 3d Mammalian Cell Perfusion-Culture System in Microfluidic Channels. *Lab Chip* **2007**;*7* 302-309.

102. Dean DM, Napolitano AP, Youssef J, Morgan JR. Rods, Tori, and Honeycombs: The Directed Self-Assembly of Microtissues with Prescribed Microscale Geometries. *FASEB J* **2007**;*21* 4005-4012.

103. Napolitano AP, Chai P, Dean DM, Morgan JR. Dynamics of the Self-Assembly of Complex Cellular Aggregates on Micromolded Nonadhesive Hydrogels. *Tissue Eng* **2007**;*13* 2087-2094.

104. Bao B, Jiang J, Yanase T, Nishi Y, Morgan JR. Connexon-Mediated Cell Adhesion Drives Microtissue Self-Assembly. *FASEB J* **2011**;*25* 255-264.

105. Bao B, Lai CP, Naus CC, Morgan JR. Pannexin1 Drives Multicellular Aggregate Compaction Via a Signaling Cascade That Remodels the Actin Cytoskeleton. *The Journal of biological chemistry* **2012**.

106. Krotz SP, Robins JC, Ferruccio TM, Moore R, Steinhoff MM, Morgan JR, Carson S. In Vitro Maturation of Oocytes Via the Pre-Fabricated Self-Assembled Artificial Human Ovary. *J Assist Reprod Genet* **2010**;*27* 743-750.

107. Youssef J, Nurse AK, Freund LB, Morgan JR. Quantification of the Forces Driving Self-Assembly of Three-Dimensional Microtissues. *Proc Natl Acad Sci U S A* **2011**;*108* 6993-6998.

108. Achilli TM, McCalla S, Tripathi A, Morgan JR. Quantification of the Kinetics and Extent of Self-Sorting in Three Dimensional Spheroids. *Tissue engineering. Part C, Methods* **2011**.

109. Zajac M, Jones GL, Glazier JA. Simulating Convergent Extension by Way of Anisotropic Differential Adhesion. *J Theor Biol* **2003**;*222* 247-259.

110. Poplawski NJ, Swat M, Gens JS, Glazier JA. Adhesion between Cells, Diffusion of Growth Factors, and Elasticity of the Aer Produce the Paddle Shape of the Chick Limb. *Physica A* **2007**;*373* 521-532.

111. Chen N, Glazier JA, Izaguirre JA, Alber MS. A Parallel Implementation of the Cellular Potts Model for Simulation of Cell-Based Morphogenesis. *Comput Phys Commun* **2007**;*176* 670-681.

112. Graner F, Glazier JA. Simulation of Biological Cell Sorting Using a Two-Dimensional Extended Potts Model. *Phys Rev Lett* **1992**;*69* 2013-2016.

113. Brodland GW. The Differential Interfacial Tension Hypothesis (Dith): A Comprehensive Theory for the Self-Rearrangement of Embryonic Cells and Tissues. *J Biomech Eng* **2002**;*124* 188-197.

114. Klopper AV, Krens G, Grill SW, Heisenberg CP. Finite-Size Corrections to Scaling Behavior in Sorted Cell Aggregates. *Eur Phys J E Soft Matter* **2010**;*33* 99-103.

115. Jiang Y, Pjesivac-Grbovic J, Cantrell C, Freyer JP. A Multiscale Model for Avascular Tumor Growth. *Biophys J* **2005**;*89* 3884-3894.

116. Ribba B, Saut O, Colin T, Bresch D, Grenier E, Boissel JP. A Multiscale Mathematical Model of Avascular Tumor Growth to Investigate the Therapeutic Benefit of Anti-Invasive Agents. *J Theor Biol* **2006**;*243* 532-541.

117. Ramis-Conde I, Drasdo D, Anderson AR, Chaplain MA. Modeling the Influence of the E-Cadherin-Beta-Catenin Pathway in Cancer Cell Invasion: A Multiscale Approach. *Biophys J* **2008**;*95* 155-165.

118. Quaranta V, Rejniak KA, Gerlee P, Anderson AR. Invasion Emerges from Cancer Cell Adaptation to Competitive Microenvironments: Quantitative Predictions from Multiscale Mathematical Models. *Semin Cancer Biol* **2008**;*18* 338-348.

119. Stein AM, Demuth T, Mobley D, Berens M, Sander LM. A Mathematical Model of Glioblastoma Tumor Spheroid Invasion in a Three-Dimensional in Vitro Experiment. *Biophys J* **2007**;*92* 356-365.

120. Mueller-Klieser W. Multicellular Spheroids. A Review on Cellular Aggregates in Cancer Research. *J Cancer Res Clin Oncol* **1987**;*113* 101-122.

121. Elliott NT, Yuan F. A Review of Three-Dimensional in Vitro Tissue Models for Drug Discovery and Transport Studies. *Journal of pharmaceutical sciences* **2011**;*100* 59-74.

122. Frieboes HB, Edgerton ME, Fruehauf JP, Rose FR, Worrall LK, Gatenby RA, Ferrari M, Cristini V. Prediction of Drug Response in Breast Cancer Using Integrative Experimental/Computational Modeling. *Cancer research* **2009**;*69* 4484-4492.

123. Sinek JP, Sanga S, Zheng X, Frieboes HB, Ferrari M, Cristini V. Predicting Drug Pharmacokinetics and Effect in Vascularized Tumors Using Computer Simulation. *J Math Biol* **2009**;*58* 485-510.

124. Kunwar PS, Siekhaus DE, Lehmann R. In Vivo Migration: A Germ Cell Perspective. *Annu Rev Cell Dev Biol* **2006**;*22* 237-265.

125. Yamada KM, Cukierman E. Modeling Tissue Morphogenesis and Cancer in 3d. *Cell* **2007**;*130* 601-610.

126. Dean DM, Morgan JR. Cytoskeletal-Mediated Tension Modulates the Directed Self-Assembly of Microtissues. *Tissue Eng Part A* **2008**;*14* 1989-1997.

127. Krieg M, Arboleda-Estudillo Y, Puech PH, Kafer J, Graner F, Muller DJ, Heisenberg CP. Tensile Forces Govern Germ-Layer Organization in Zebrafish. *Nat Cell Biol* **2008**;*10* 429-436.

128. Tzanakakis ES, Hansen LK, Hu WS. The Role of Actin Filaments and Microtubules in Hepatocyte Spheroid Self-Assembly. *Cell Motil Cytoskeleton* **2001**;*48* 175-189.

129. Nakamura M, Shinji T, Ujike K, Hirasaki S, Koide N, Tsuji T. Cytoskeletal Inhibitors, Anti-Adhesion Molecule Antibodies, and Lectins Inhibit Hepatocyte Spheroid Formation. *Acta Med Okayama* **2002**;*56* 43-50.

130. Youssef J, Chen P, Shenoy VB, Morgan JR. Mechanotransduction Is Enhanced by the Synergistic Action of Heterotypic Cell Interactions and Tgf-Beta1. *FASEB J* **2012**.

131. Sutherland RM. Cell and Environment Interactions in Tumor Microregions: The Multicell Spheroid Model. *Science* **1988**;*240* 177-184.

132. Birgersdotter A, Sandberg R, Ernberg I. Gene Expression Perturbation in Vitro--a Growing Case for Three-Dimensional (3d) Culture Systems. *Semin Cancer Biol* **2005**;*15* 405-412.

133. Kalluri R, Zeisberg M. Fibroblasts in Cancer. *Nature reviews. Cancer* **2006**;*6* 392-401.

134. Kaur P, Ward B, Saha B, Young L, Groshen S, Techy G, Lu Y, Atkinson R, Taylor CR, Ingram M, Imam SA. Human Breast Cancer Histoid: An in Vitro 3-Dimensional Co-Culture Model That Mimics Breast Cancer Tissue. *J Histochem Cytochem* **2011**;*59* 1087-1100.

135. Upreti M, Jamshidi-Parsian A, Koonce NA, Webber JS, Sharma SK, Asea AA, Mader MJ, Griffin RJ. Tumor-Endothelial Cell Three-Dimensional Spheroids: New Aspects to Enhance Radiation and Drug Therapeutics. *Transl Oncol* **2011**;*4* 365-376.

136. Debnath J, Brugge JS. Modelling Glandular Epithelial Cancers in Three-Dimensional Cultures. *Nature reviews. Cancer* **2005**;*5* 675-688.

137. Graff CP, Wittrup KD. Theoretical Analysis of Antibody Targeting of Tumor Spheroids: Importance of Dosage for Penetration, and Affinity for Retention. *Cancer research* **2003**;*63* 1288-1296.

138. Thurber GM, Schmidt MM, Wittrup KD. Antibody Tumor Penetration: Transport Opposed by Systemic and Antigen-Mediated Clearance. *Advanced drug delivery reviews* **2008**;*60* 1421-1434.

139. Wong HL, Shen Z, Lu Z, Wientjes MG, Au JL. Paclitaxel Tumor-Priming Enhances Sirna Delivery and Transfection in 3-Dimensional Tumor Cultures. *Mol Pharm* **2011**;*8* 833-840.

140. Sharkey RM, Goldenberg DM. Use of Antibodies and Immunoconjugates for the Therapy of More Accessible Cancers. *Advanced drug delivery reviews* **2008**;*60* 1407-1420.

141. Minchinton AI, Tannock IF. Drug Penetration in Solid Tumours. *Nature reviews. Cancer* **2006**;*6* 583-592.

142. Huang L, Ao Q, Zhang Q, Yang X, Xing H, Li F, Chen G, Zhou J, Wang S, Xu G, Meng L, Lu Y, Ma D. Hypoxia Induced Paclitaxel Resistance in Human Ovarian Cancers Via Hypoxia-Inducible Factor 1alpha. *J Cancer Res Clin Oncol* **2010**;*136* 447-456.

143. Kerr DJ, Wheldon TE, Kerr AM, Kaye SB. In Vitro Chemosensitivity Testing Using the Multicellular Tumor Spheroid Model. *Cancer Drug Deliv* **1987**;*4* 63-74.

144. Tannock IF, Lee CM, Tunggal JK, Cowan DS, Egorin MJ. Limited Penetration of Anticancer Drugs through Tumor Tissue: A Potential Cause of Resistance of Solid Tumors to Chemotherapy. *Clinical cancer research : an official journal of the American Association for Cancer Research* **2002**;*8* 878-884.

145. Layer PG, Robitzki A, Rothermel A, Willbold E. Of Layers and Spheres: The Reaggregate Approach in Tissue Engineering. *Trends Neurosci* **2002**;*25* 131-134.

146. Kelm JM, Ehler E, Nielsen LK, Schlatter S, Perriard JC, Fussenegger M. Design of Artificial Myocardial Microtissues. *Tissue Eng* **2004**;*10* 201-214.

147. Mahmoudifar N, Doran PM. Chondrogenesis and Cartilage Tissue Engineering: The Longer Road to Technology Development. *Trends Biotechnol* **2011**.

148. Revell CM, Reynolds CE, Athanasiou KA. Effects of Initial Cell Seeding in Self Assembly of Articular Cartilage. *Ann Biomed Eng* **2008**;*36* 1441-1448.

149. Hu JC, Athanasiou KA. A Self-Assembling Process in Articular Cartilage Tissue Engineering. *Tissue Eng* **2006**;*12* 969-979.

150. Abu-Absi SF, Friend JR, Hansen LK, Hu WS. Structural Polarity and Functional Bile Canaliculi in Rat Hepatocyte Spheroids. *Exp Cell Res* **2002**;*274* 56-67.

151. Riccalton-Banks L, Liew C, Bhandari R, Fry J, Shakesheff K. Long-Term Culture of Functional Liver Tissue: Three-Dimensional Coculture of Primary Hepatocytes and Stellate Cells. *Tissue Eng* **2003**;*9* 401-410.

152. Lehnert L, Trost H, Schmiegel W, Roder C, Kalthoff H. Hollow-Spheres: A New Model for Analyses of Differentiation of Pancreatic Duct Epithelial Cells. *Ann N Y Acad Sci* **1999**;*880* 83-93.

153. Lehnert L, Lerch MM, Hirai Y, Kruse ML, Schmiegel W, Kalthoff H. Autocrine Stimulation of Human Pancreatic Duct-Like Development by Soluble Isoforms of Epimorphin in Vitro. *J Cell Biol* **2001**;*152* 911-922.

154. Rothermel A, Biedermann T, Weigel W, Kurz R, Ruffer M, Layer PG, Robitzki AA. Artificial Design of Three-Dimensional Retina-Like Tissue from Dissociated Cells of the Mammalian Retina by Rotation-Mediated Cell Aggregation. *Tissue Eng* **2005**;*11* 1749-1756.

155. Griffith CK, Miller C, Sainson RC, Calvert JW, Jeon NL, Hughes CC, George SC. Diffusion Limits of an in Vitro Thick Prevascularized Tissue. *Tissue Eng* **2005**;*11* 257-266.

156. Khademhosseini A, Langer R, Borenstein J, Vacanti JP. Microscale Technologies for Tissue Engineering and Biology. *Proc Natl Acad Sci U S A* **2006**;*103* 2480-2487.

157. Kelm JM, Djonov V, Ittner LM, Fluri D, Born W, Hoerstrup SP, Fussenegger M. Design of Custom-Shaped Vascularized Tissues Using Microtissue Spheroids as Minimal Building Units. *Tissue Eng* **2006**;*12* 2151-2160.

158. Alajati A, Laib AM, Weber H, Boos AM, Bartol A, Ikenberg K, Korff T, Zentgraf H, Obodozie C, Graeser R, Christian S, Finkenzeller G, Stark GB, Heroult M, Augustin HG. Spheroid-Based Engineering of a Human Vasculature in Mice. *Nat Methods* **2008**;*5* 439-445.

159. Wenger A, Stahl A, Weber H, Finkenzeller G, Augustin HG, Stark GB, Kneser U. Modulation of in Vitro Angiogenesis in a Three-Dimensional Spheroidal Coculture Model for Bone Tissue Engineering. *Tissue Eng* **2004**;*10* 1536-1547.

160. Boland T, Mironov V, Gutowska A, Roth EA, Markwald RR. Cell and Organ Printing 2: Fusion of Cell Aggregates in Three-Dimensional Gels. *Anat Rec A Discov Mol Cell Evol Biol* **2003**;*272* 497-502.

161. Jakab K, Neagu A, Mironov V, Markwald RR, Forgacs G. Engineering Biological Structures of Prescribed Shape Using Self-Assembling Multicellular Systems. *Proc Natl Acad Sci U S A* **2004**;*101* 2864-2869.

162. Jakab K, Norotte C, Marga F, Murphy K, Vunjak-Novakovic G, Forgacs G. Tissue Engineering by Self-Assembly and Bio-Printing of Living Cells. *Biofabrication* **2010**;*2* 022001.

163. Mironov V, Boland T, Trusk T, Forgacs G, Markwald RR. Organ Printing: Computer-Aided Jet-Based 3d Tissue Engineering. *Trends Biotechnol* **2003**;*21* 157-161.

164. Mironov V, Visconti RP, Kasyanov V, Forgacs G, Drake CJ, Markwald RR. Organ Printing: Tissue Spheroids as Building Blocks. *Biomaterials* **2009**;*30* 2164-2174.

165. Smith CM, Stone AL, Parkhill RL, Stewart RL, Simpkins MW, Kachurin AM, Warren WL, Williams SK. Three-Dimensional Bioassembly Tool for Generating Viable Tissue-Engineered Constructs. *Tissue Eng* **2004**;*10* 1566-1576.

166. Wilson WC, Jr., Boland T. Cell and Organ Printing 1: Protein and Cell Printers. *Anat Rec A Discov Mol Cell Evol Biol* **2003**;*272* 491-496.

167. Rago AP, Dean DM, Morgan JR. Controlling Cell Position in Complex Heterotypic 3d Microtissues by Tissue Fusion. *Biotechnol Bioeng* **2009**;*102* 1231-1241.

168. McGuigan AP, Sefton MV. Vascularized Organoid Engineered by Modular Assembly Enables Blood Perfusion. *Proc Natl Acad Sci U S A* **2006**;*103* 11461-11466.

169. Yang J, Yamato M, Kohno C, Nishimoto A, Sekine H, Fukai F, Okano T. Cell Sheet Engineering: Recreating Tissues without Biodegradable Scaffolds. *Biomaterials* **2005**;*26* 6415-6422.

170. Ito A, Ino K, Hayashida M, Kobayashi T, Matsunuma H, Kagami H, Ueda M, Honda H. Novel Methodology for Fabrication of Tissue-Engineered Tubular Constructs Using Magnetite Nanoparticles and Magnetic Force. *Tissue Eng* **2005**;*11* 1553-1561.

171. Livoti CM, Morgan JR. Self-Assembly and Tissue Fusion of Toroid-Shaped Minimal Building Units. *Tissue Eng Part A* **2010**;*16* 2051-2061.

172. Tejavibulya N, Youssef J, Bao B, Ferruccio TM, Morgan JR. Directed Self-Assembly of Large Scaffold-Free Multi-Cellular Honeycomb Structures. *Biofabrication* **2011**;*3* 034110.

1.8 Figures

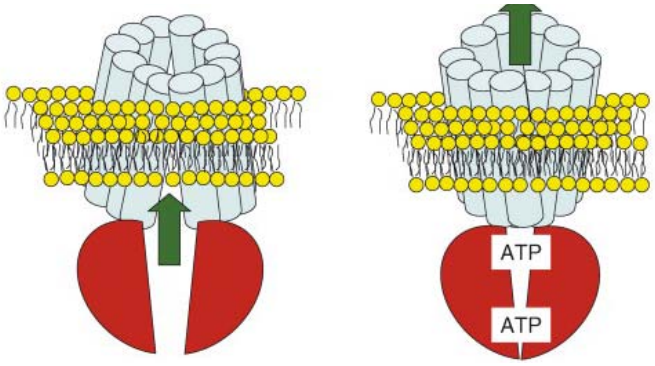

Figure 1-1. General structure and mechanism of ATP-binding cassette transporters. The 12 transmembrane helices form a central cavity in the cell membrane. In the left panel, the nucleotide binding domains are open and nucleotide-free, and the transmembrane helices provide an inward-facing conformation. ATP-driven hydrolysis results in the outward-facing conformation of the TMDs, and ultimately in the efflux of the substrate. (18)

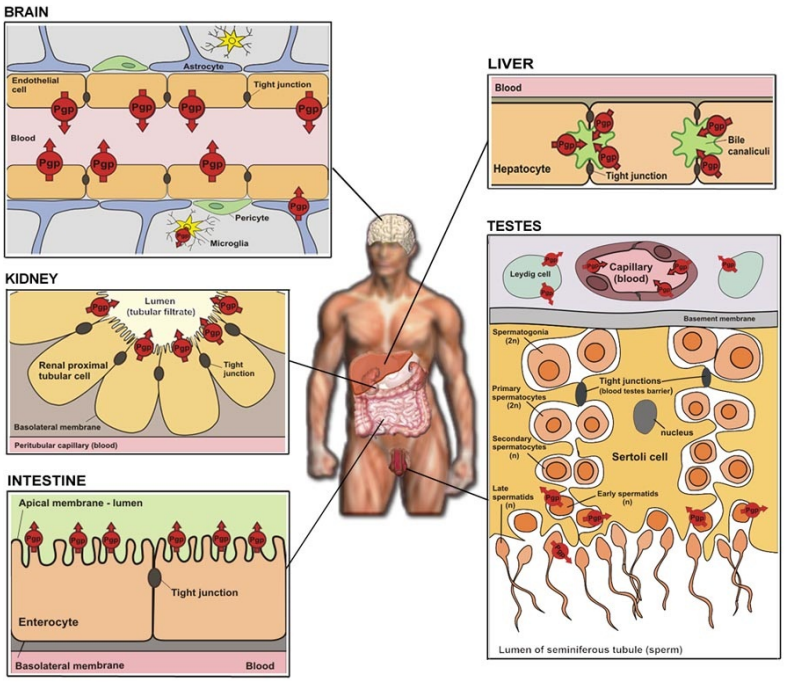

Figure 1-2. **P-glycoprotein has a wide tissue distribution in the body. In general, Pgp is located in tissues involved in the ADME-Tox of drugs (liver, kidney, and intestine), or at barriers to protect sensitive tissues (blood-brain barrier, testes, blood placental barrier). (78)**

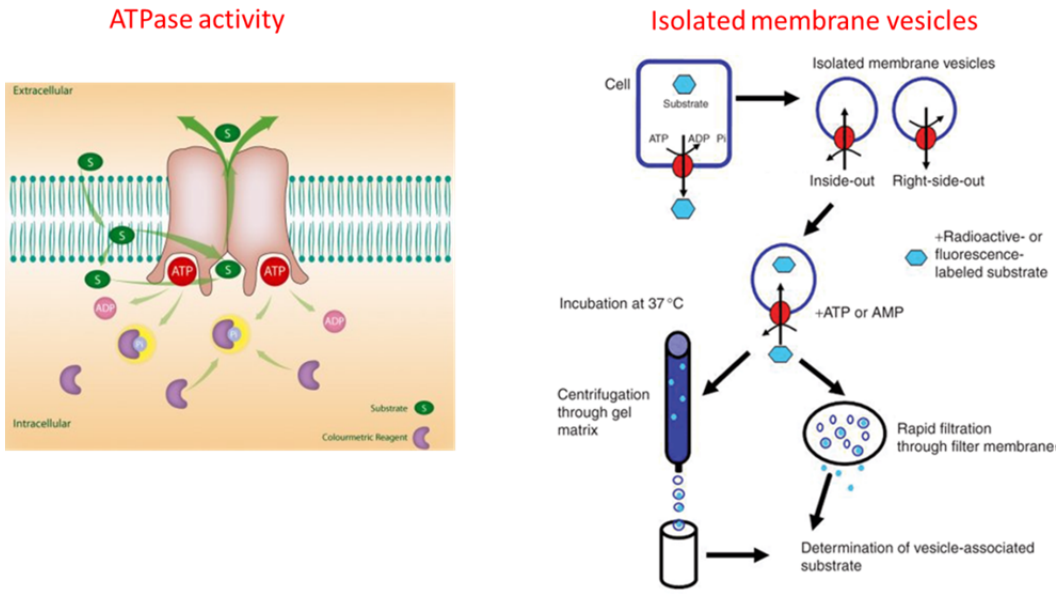

Figure 1-3. Membrane based *in vitro* methods. Here are diagrams explaining two of the membrane based *in vitro* assays to study transporter substrate and inhibitor interactions. On the left is the ATPase activity, and on the right is the inside-out membrane vesicle assay. (44)

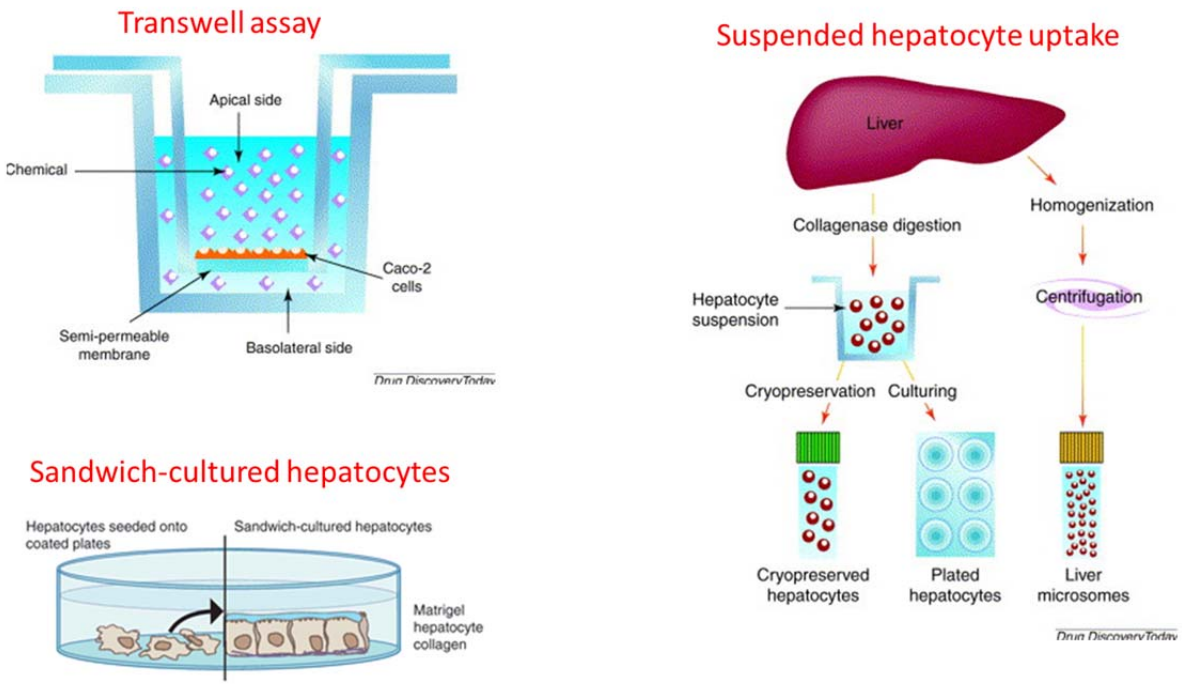

Figure 1-4. Cell based *in vitro* assays. Here are diagrams explaining three of the cell based *in vitro* assays to study transporter substrate and inhibitor interactions. On the left is the transcellular transport assay, and sandwich-cultured hepatocytes, and on the right are suspended hepatocytes to use in the cellular accumulation assay. (44,45)

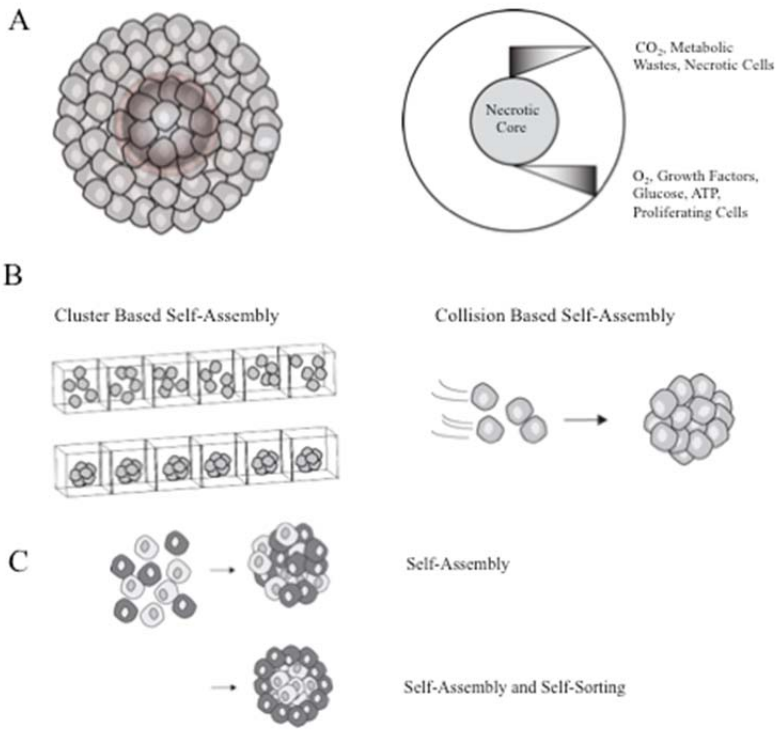

Figure 1-5. Spheroid gradients and modes of self-assembly. (A)The concentric organization of proliferating and necrotic cells in multicellular spheroids is influenced by the molecular gradients of soluble factors which are established by convection and diffusion within the spheroid microenvironment. (B) There are two main categories of spheroid bio-fabrication, cluster based and collision based self-assembly. In cluster based self-assembly, monodispersed cells are segregated into compartments, settle, and aggregate to form spheroids. In collision based self-assembly, suspended cells collide to form spheroids. (C) When certain mixed cell populations self-assemble, the specific pattern of segregation that occurs is referred to as self-sorting.

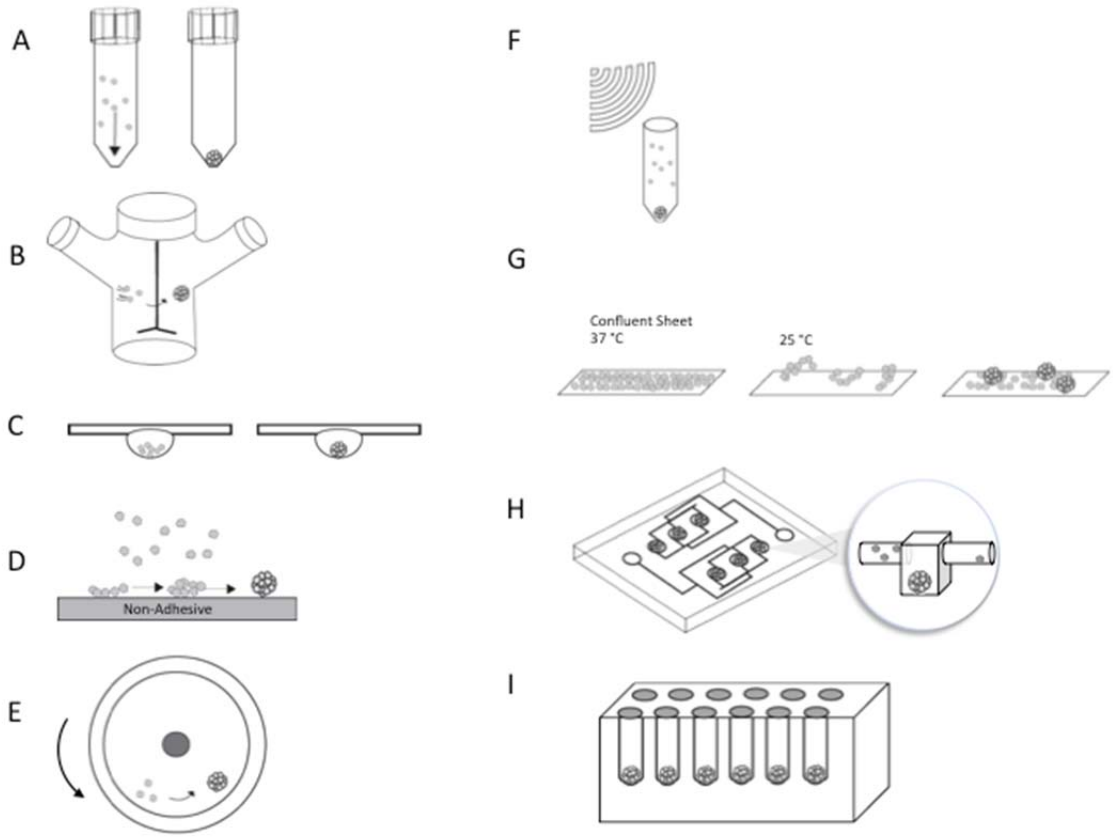

Figure 1-6. **Methods of spheroid bio-fabrication (A) Pellet Culture (B) Spinner Culture (C) Hanging Drop (D) Liquid Overlay (E) Rotating Wall Vessel (F) External Force (G) Cell Sheets (H) Microfluidics (I) Nonadhesive Hydrogel Micro-molds**

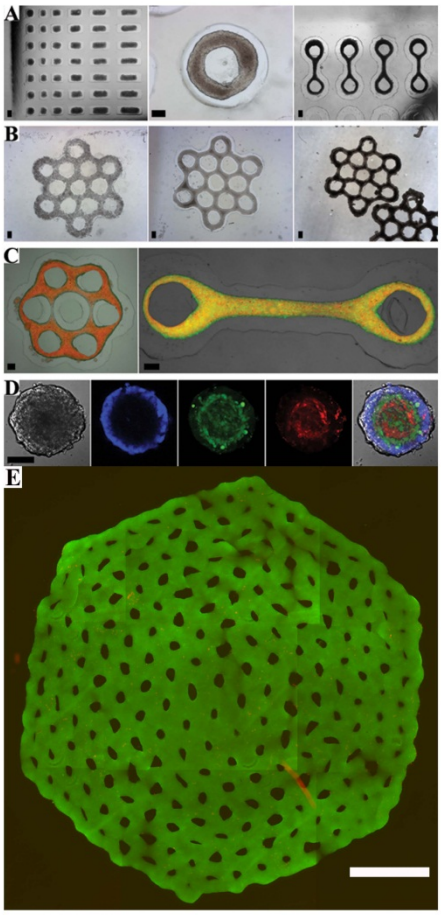

Figure 1-7. Micro-molded hydrogels can be used to direct the self-assembly of a number of shapes including rodes, toroids, loop-ended dogbones, and honeycombs. (A) Microtissues with complex geometries were self-assembled from various cell types: rat hepatoma (H35) rods (left), MCF-7 toroid (middle), and H35 loop-ended dog bones (right). (B) MCF-7 cells seeded into honeycomb recesses (left), formed a branched microtissue by 1 day (middle), and compacted slightly but retained the honeycomb shape for at least 3 days after removal from the mold (right). Mixed-cell populations produced multilayered microtissues with controlled shape. (C) Images of microtissues with normal human fibroblasts (NHF) (red) cores coated by an outer layer of H35 (green, left) or HUVEC (green, right). (D) Confocal microscopy images of self-sorting of three cell types within a 2-day-old tritypic spheroid. (E) The eight orbital honeycomb of NHG ($6x10^6$ cells) was stained with a live/dead assay after 24 hours to show viability. Scale bars are 200 µm (panels A-C), 100 µm (panel D), and 1800 µm (panel E). Figure permissions Biotechniques, and Biofabrication.

Chapter 2

2. Quantification of the Kinetics and Extent of Self-Sorting in Three Dimensional Spheroids

Toni-Marie Achilli, Stephanie McCalla, Anubhav Tripathi, and Jeffrey R. Morgan

The following chapter was published in Tissue Engineering Part C 2012 Apr;18(4):302-9. doi: 10.1089/ten.TEC.2011.0478. Epub 2011 Dec 16.

2.1 Abstract

The self-sorting of cells into distinct compartments in three-dimensional (3D) microtissues is a process critical to developmental biology, cancer metastasis, and tissue engineering. Although self-sorting has been studied since the 1950s, little quantitative data exists to describe this dynamic process. Here, we describe a recently developed assay designed to quantify the extent and kinetics of self-sorting in 3D. Mixtures of fluorescently labeled fibroblast (NHF) and hepatocyte (H35) cells were fluorescently labeled, red and green respectively, and seeded onto micro-molded nonadhesive hydrogels. The cells self-assembled into a spheroid and self-sorted with NHFs forming the central core and H35s forming the outer shell. A time course of fluorescent images were used to analyze the ratio of red (NHFs) and green (H35s) fluorescence in concentric hollow cylinders throughout a spheroid and was statistically compared to the fluorescent ratio of the perfectly sorted spheroid. We found that NHFs and H35s, at a 1:1 ratio, sorted to a final extent of 88 ± 3% at an initial rate of 0.36 ± 0.06% per minute and reached 50% self-sorted at 2.7 ± 0.3 hours. Studies with varying ratios of NHFs and H35s show that self-sorting and self-assembly are coincident in time when the proportion of NHFs are varied over a 6-fold range (14% to 85%). This method can thus be used to characterize the sorting behavior of additional pairs of cells, the effect of drugs and growth factors that may change the kinetics of the process, and bring an understanding to the cellular mechanisms which control self-sorting.

2.2 Introduction

In nonadhesive environments, cells will aggregate and form three dimensional (3D) multi-cellular microtissues[1]. In addition to aggregating, mixtures of different cell types will often segregate (self-sort), a process relevant to embryogenesis, morphogenesis, cancer metastasis, and tissue engineering[1-3]. Self-sorting has qualitatively been observed since the 1950s, and the process has been hypothesized to be the result of differences in surface adhesion molecules; the differential adhesion hypothesis (DAH)[2,4-7]. According to DAH, cells are discrete mobile units within a spheroid and cell types have differences in cohesive forces (like-to-like) and adhesive forces (unlike binding). Self-sorting occurs due to these differences with cells of highest cohesion in the core and cells with lower cohesion on the outside[2]. However, recent studies from a number of labs including our own, suggest that self-sorting is more complicated and involves the biomechanics of the cytoskeleton[8-10]. These studies showed that differences in cytoskeletal mediated tension between pairs of cells also resulted in self-sorting.

Nearly all studies of self-sorting have been qualitative in nature and there is little quantitative data on what is clearly a dynamic process. One problem is the limitations of using spinner cultures or rotational cultures to form spheroids[5,11,12]. Although, spheroids that have clearly self-sorted are produced at the end of the spinner culture method, it's impossible to monitor in real time the kinetics of self-assembly and self-sorting. Several groups have used simulations to model the process of self-sorting[13-16]. For example, most recently, self-sorting has been quantitatively described using an order parameter, which is based on a geometrically driven argument to describe the relationship between heterotypical interface length and the system size[13]. Additional simulations involve analysis of cell surface tension during the different states of reorganization using either

two dimensional lattice simulations or free particle simulations[14,16]. However, missing from the self-sorting field is quantitative empirical data on the kinetics of self-sorting, the extent of self-sorting and the quantification of various cellular systems (e.g, surface adhesion molecules versus cytoskeletal motors) to the process of self-sorting.

Using micro-molded nonadhesive hydrogels, we have qualitatively analyzed the self-sorting behavior of several cell types. In particular, we have extensively characterized the interaction and self-sorting of normal human fibroblasts (NHFs) and reuber-H35 rat hepatoma cells (H35s)[17]. In a heterotypic spheroid of NHFs and H35s, the NHFs will sort to the center forming a central core and the H35s will sort to the outside to form the outer shell. Here, we describe a newly developed assay to measure and quantify the kinetics and extent of self-sorting in 3D microtissues using epifluorescent microscopy. NHFs and H35s were labeled with red and green fluorescent tracking dyes, respectively. The mixture of cells was seeded onto micro-molded nonadhesive hydrogels and a time course of fluorescent images was taken using conventional and side view microscopy as the cell mixture self-assembled and self-sorted in 3D. The ratio of red and green fluorescence of concentric hollow cylinders was calculated, compared to a reference spheroid of similar size and shape that had perfectly sorted and a goodness-of-fit was used to determine sorting. We found that a 1:1 ratio (NHF:H35) self-sorted to a final extent of 88 ± 3% at an initial rate (v_o) of 0.36 ± 0.06 % per minute and the time to reach 50% self-sorted ($t_{1/2}$) was 2.7 ± 0.3 hours. When normalized to self-assembly, the rate of self-sorting and the rate of self-assembly were coincident in time. The method was further used to quantify how the rate and extent of self-sorting changed as the ratio of NHFs and H35s was varied in spheroids of similar size. This method provides important

quantitative data on the kinetics and extent of self-sorting, is applicable to any pairs of cell types, and can be used to investigate in detail the complex molecular and cellular process of self-sorting in 3D.

2.3 Materials and Methods

Design, Fabrication, and Casting of Micro-molds

Micro-molds were produced as described previously[17]. In brief, micro-molds were designed using the computer design software SolidWorks (SolidWorks Corporation, Concord, MA). Designs used for side view microscopy contained a single row of 21 recesses, each recess 400 μm in diameter and 800 μm in depth, From these files, wax molds were produced with a ThermoJet® rapid prototyping machine (3D Systems Corporation, Valencia, CA). Polyacrylamide gels used for side view microscopy were reproduced directly from the wax molds[18]. All chemicals, unless otherwise noted, were purchased from Sigma Aldrich (St. Louis, MO). A mixture of acrylamide/bis-acrylamide (29:1 ratio), ammonium persulfate (APS), 0.5 M Tris Buffer (pH 6.8), and Dulbecco's Modified Eagle's Medium (DMEM) (Invitrogen, Carlsbad, CA) was degassed. To initiate polymerization, N, N, N', N'-tetramethylethlyenediamine (TEMED) was added. The solution was mixed, pipetted into the wax mold, and a glass cover slip was placed on the mold to create a flat bottom on the gel. After 10 minutes, the hydrogel was removed from the mold, placed into sterile six-well plate, and washed with DMEM several times. Hydrogels were equiliberated overnight in DMEM before use.

Micro-molds used for conventional view inverted microscopy contained a 12 x 8 array of 96 recesses (MicroTissues, Inc., Providence, RI) and were sterilized by autoclaving. Hydrogels were cast from the micro-molds, using a 2% molten agarose solution, prepared by mixing sterile Ultrapure™ agarose (Invitrogen) powder and 0.9% saline, agarose was melted via the microwave oven and 0.25 mL was added to the micro-mold. After the

agarose gelled (~ 5 minutes), gels were transferred to a 24 well tissue culture plate where they were equilibrated in culture medium overnight.

Cell Culture and Hydrogel Seeding

Normal human fibroblasts (NHF) (passages 2-12), derived from neonatal foreskins, and reuber-H35 rat hepatoma cells (H35s) (Passages 6-14) were grown in DMEM (Invitrogen) supplemented with 10% fetal bovine serum (FBS) (Thermo Fisher Scientific, Waltham, MA) and 1% penicillin/streptomycin (Sigma) at 37° C with 10% CO_2. Cells were stained by incubation in DMEM 5 μM Cell Tracker Red CMPTX, Cell Tracker Green CMFDA, or Cell Tracker Blue CMAC (Invitrogen) for 50 minutes, medium was changed to serum-free DMEM and incubated for 30 minutes. Cells were then trypsinized according to standard protocol, counted and then mixed in the appropriate ratios of NHFs: H35s. The mixed population of cells were spun down at 800 rpm for 6 minutes, and resuspended in 100 μl of DMEM. For all ratios and experimental conditions the total number of cells was held constant. Each micro-molded hydrogel containing 96 recesses was seeded with a total of 0.15×10^6 cells per hydrogel. Cells were allowed to settle for 30 minutes, then 2 ml of fresh medium was added to each of the wells. Time-lapse microscopy was used to acquire images every 30 minutes for 15 hours at 37º C and a 10 % CO_2 atmosphere.

Microscopy and Image Analysis

Two forms of microscopy were used in this method. Horizontal view microscopy was used to validate the depth (z) of the spheroid. A Mitutouo FS-110 microscope altered

to lie on its back was used to view samples that were placed on a translational stage. Brightfield images were taken through the eyepiece of the camera using a Nikon Coolpix 900 digital camera. For conventional inverted microscope images (*x*-*y*), a Carl Zeiss Axio Observer Z1 equipped with an AxioCam MRm camera (Carl Zeiss MicroImaging, Thornwood, NY) and Xcite 120 XL mercury lamp (Exfo Life Sciences Division, Mississauga, Ontario) were used to obtain brightfield, phase contrast, and epi-fluorescent images. ImageJ Software (Rasband, W.S., ImageJ, NIH) was used to measure the height, major axis, and minor axis of the spheroid, as well as the fluorescent intensity of 10 μm shells across the spheroid.

Generation of Theoretical Curves for a Perfect Sort

A macro was developed to calculate the theoretical core-to-shell ratio for a range of spheroid sizes and shapes that had perfectly sorted. The known ratio between the total volume of the two cells in the spheroid is given by

$$K = \frac{n_c r_c^{\,3}}{n_s r_s^{\,3}} \qquad (1)$$

where r_c and n_c are the radius and number of the cell type that sorts to the core, and r_s and n_s are the radius and number of the cell type that sorts to the shell. The depth of the shell c can be determined using the relationship

$$\frac{K(abd)}{(1+K)} = (a-c)(b-c)(d-c) \qquad (2)$$

where a is the half-width, b is the half-height, and d is the half-depth of the spheroid. The spheroid was then broken into 10μm concentric shells (cylinders), and the volume of both cell types within each shell was determined by shell integration.

Quantification of Self-sorting

To quantify self-sorting at a given location in the spheroid, we locally calculated the deviation of the experimental value from the theoretical value of a perfectly sorted spheroid of comparable size and shape. This was repeated at each point along the experimental and theoretical curves. We determined the overall percent self-sorted at each time point using a goodness-of-fit of the experimental data to the theoretical model, using the coefficient of determination, R^2, such that,

$$R^2 = 1 - \frac{SS_{err}}{SS_{tot}} \tag{3}$$

where, SS_{tot} is the total sum of squares (proportional to the sample variance), and SS_{err} is the sum of squares of residuals. R^2 values are bounded between 0 and 1, such that 0 signifies no fit to the theoretical data and 1 signifies a perfect fit. R^2 values can be negative as well, when the model is not linear. A negative number indicates no fit between the theoretical and experimental data, and thus can be set to 0.

Statistical Analysis

T-tests were performed to determine statistical significance with p-values < 0.05 considered statistically significant.

2.4 Results and Discussion

To analyze the process of self-sorting, we seeded a cell mixture (1:1) of NHFs (labeled red) and H35s (labeled green) onto micro-molded agarose gels. The cells settled to the bottom of the recesses and fluorescent wide-field images were obtained over 15 hours as they self-assembled and self-sorted (**Figure 2-1**). The cells assembled from a thin layer of randomly distributed mono-dispersed cells settled at the bottom of each recess into a spheroid where NHFs formed the central core and H35s formed the outer shell of the spheroid. The processes of self-assembly and self-sorting both occurred during the 15 hour time frame and involved not only movement of cells in the *x*, *y*, and *z* dimensions, but also specific movements of the two different cell types relative to one another to achieve self-sorting.

To determine the uniformity of the spheroids, the size and the ratio of NHFs and H35 cells within each of the recesses at the initial (0 hours) and final (15 hours) time points were measured (**Figure 2-2**). The major (*x*) and minor (*y*) axes, respectively were 339 ± 13 μm and 347 ± 16μm at 0 hours, and 193 ± 9 μm and 190 ± 12 μm at 15 hours (n = 12). The sizes were uniform and the decrease in *x* and *y* axes over time indicated that the cells were self-assembling a 3D spheroid whose *z* axis was increasing. To quantify the changes in the *z* axis and determine if spheroid volume remained constant over time, we also obtained side view images of the spheroids. The computed volume at 0, 3, 6, 9, 12, and 15 hours was $2.5 \pm 0.6 \times 10^6$ μm^3. These data show that cell distribution in each recess was uniform with respect to total cell number which controls final spheroid size. Furthermore, the ratio of red to green fluorescent intensity was also uniform for each recess and remained constant. At time zero, the ratio was 0.873 ± 0.069 and after 15 hours the ratio was 0.861 ± 0.073 (n = 12). These data indicate that after 15 hours, the

cells formed an oblate spheroid of uniform size and volume in each recess. This verification of uniformity, allows us to calculate spheroid height and volume from conventional images of the *x* and *y* axes. Moreover, we know from previous work that if spheroids have a z height less than 205 μm, there is minimal loss of the red and green fluorescent signal.

To quantify self-sorting, we used the elliptical tool in ImageJ to draw a circular perimeter encompassing the entire spheroid **(Figure 2-3)**, and measured total red and green fluorescence. The perimeter was then eroded radially 10μm, and the fluorescence of each of the fluorophores was quantified for each 10μm shell until the radius was less than 10μm. Each 10μm shell was in fact a hollow cylinder that collected the fluorescence from the *x*, *y* as well *z* planes of the spheroid **(Figure 2-3)**. To determine the net fluorescence, the background fluorescence was calculated as fluorescence per area, and the cylinders were corrected for this accordingly. Net fluorescence was normalized to the total fluorescence in the spheroid to account for differences in exposure time, photobleaching, and fluorescent properties of the fluorophores. To determine the extent to which a spheroid was self-sorted, the ratio of relative red and green fluorescence in each 10μm cylinder was calculated. A core-to-shell ratio (NHF to H35) was used to ensure that the ratio was always a defined number. Randomness (unsorted) was defined by the geometry of the spheroid, as well as the size and ratio of the input cells. Since NHFs have a diameter of 20μm and H35s a diameter of 17μm, a 1:1 mix of these cells has a randomness ratio of 1.63. We defined self-sorting as a change from randomness, thus a mathematical change from 1.63, which could be either an increase or decrease from this value.

The opposite state of randomness is perfect self-sorting. Although the value for randomness is the same at all locations in the spheroid and is independent of spheroid shape, the theoretical value for perfect self-sorting varies at each radial location and is dependent on spheroid shape. To calculate these values for perfect self-sorting, we designed a visual basic macro that models the theoretical volume ratios of two different cell types that have formed a perfectly self-sorted spheroid of given shape. A perfectly self-sorted spheroid has a core of one cell type (NHFs) surrounded by a shell of the other cell type (H35s). The macro calculates the total volume of the core cells and the total volume of shell cells in each 10μm cylinder using a shell integration method, and then calculates the expected volume ratios (core cells/shell cells) for each cylinder.

During self-assembly, the shape of the spheroid undergoes significant changes. Over time, a thin layer of mono-dispersed cells settled in the bottom of each recess forms an oblate spheroid that progresses towards, but rarely reaches a perfect sphere. We used our macro to generate theoretical curves of the perfect sort for this shape evolution over time. From our experimental measurements, the starting *x, y* radii of 180 μm and *z* height of 30 μm progresses to a final spheroid with an *x, y* radii of 101 μm and *z* height of 95 μm which can be seen by the leftward shift of the endpoints of each curve (**Figure 2-3C)**. Corresponding experimental curves for each time point (**Figure 2-3D**) were generated and compared to the theoretical curves. To quantify the percent sorted, we calculated the deviation of the data from the theoretical values for a perfect sort at each radial location using the coefficient of determination R^2, with values bounded between 0 and 1, with 1 representing a perfect sort. The R^2 value is significant on its own, and we convert that value into a percent sorted, or percent correlated to the theory of the perfectly sorted.

We quantified the kinetics and extent of self-sorting of a 1:1 mix of NHFs and H35s and compared them to the kinetics of self-assembly. Self-assembly was quantified by measuring the decrease in radius which by 15 hours had decreased by 0.59 ± 0.03 % of its original length (**Figure 2-4**). At 15 hours, self-sorting was 88 ± 3 %. To compare the rates of self-assembly and self-sorting, we normalized the values and calculated the initial rate (v_o), the time to reach 50 % ($t_{1/2}$), and the time to reach steady state (t_{ss}). For self-assembly, v_o was 0.24 ± 0.08 % per minute, $t_{1/2}$ was 2.9 ± 0.4 hours, and t_{ss} was 8.5 ± 0.3 hours. For self-sorting, v_o was 0.36 ± 0.06 % per minute, $t_{1/2}$ was 2.7 ± 0.3 hours, and t_{ss} was 8.4 ± 0.5 hours. Thus, self-sorting and self-assembly in the 1:1 mix were coincident in time.

To determine if the ratio of input cells influenced self-assembly or self-sorting, we increased the proportion of NHF (NHF: H35, 10:1, 6:1, 4:1, 2:1, 1:1) and kept the total number of cells constant. With increasing NHFs, spheroid size remained constant with a larger core of NHFs and a decreased shell of H35s (**Figure 2-5).** As the proportion of NHFs was increased, there were no significant changes to the kinetics or extent of self-assembly (**Table 1**). There were no significant differences when the proportion of NHFs was reduced (1:2, 1:4), suggesting that the proportion of NHFs is not rate limiting over this range. With regards to self-sorting, as the proportion of NHFs was increased, t_{ss} was unaffected, but the $t_{1/2}$ was increased (6:1 = 3.8 ± 0.3 hrs, 10:1 = 6.4 ± 0.4 hrs) and the extent of self-sorting was decreased at the highest proportion (80 ± 6%). The expected size of a perfectly formed H35 shell at the highest proportion of NHFs is only 4-5 μm in thickness which may limit the accuracy of our measurement at this cell ratio.

When we increased the proportion of H35s (NHF: H35, 1:2, 1:4, 1:6, and 1:10), spheroid size was constant with a decreased core of NHFs and an increased shell thickness of H35s (**Figure 2-6**). At the highest proportions of H35s (1:6, 1:10) self-assembly was slowed and the extent of self-assembly was decreased. Likewise, self-sorting was also affected. The extent of self-sorting decreased for the highest proportion of H35s (1:10, 64 ± 6%) and both the t_{ss} and the $t_{1/2}$ increased for the highest proportions of H35s (1:6, 1:10), suggesting that when self-assembly is slowed by a rate limiting number of NHFs, the extent and rate of self-sorting are also slowed. However, over a significant range of different cell ratios (NHF: H35, 1:4, 1:2, 1:1, 2:1, 4:1), the rate and extent of self-assembly and self-sorting are constant. The method in this paper is the first to quantify the kinetics and extent of self-sorting of empirical data from easy to obtain fluorescent images of cells as they undergo self-sorting. Prior quantitative methods have focused mainly on using mathematical models to simulate the process of self-sorting[13-16]. Our method provides a straightforward means to quantify the sorting of any pair of cell types and to obtain quantitative data useful for investigating the mechanism of self-sorting and the cellular processes that control it.

To examine more closely the situation where the proportion of NHFs is small (NHF: H35, 1:10), phase contrast and fluorescent images were obtained and compared to the 1:4 mix (**Figure 2-7**). There were no obvious differences in spheroid size, but the fluorescent images showed differences in the organization of the NHF core. The NHF core in the 1:4 mix was tightly packed and surrounded by an H35 shell, whereas the NHF core in the 1:10 mix was more loosely packed with extensions into the H35 shell. This suggests that when NHF numbers are high, homotypic interactions cause the formation of

a tight core. Whereas, when NHF numbers are low, there are homotypic interactions to form a core, but also increased heterotypic interactions that give rise to NHF extensions into the shell. One possible explanation is that the tension environment changes when the percentage of NHFs is low. Prior work has shown that in high-tension states, fibroblasts rely on actomyosin contraction, but in low tension states, fibroblasts use microtubule-dependent dendritic extensions to provide mechanical structure to their environment[19,20].

2.5 Conclusions

In summary, we've developed an image based method to quantify the kinetics and extent of the self-sorting that occurs when two different cell types aggregate and self-assemble in a scaffold-free environment. The method is used with wide-field fluorescent images and can be used to quantify the initial rate (v_o), the time to reach 50 % ($t_{1/2}$) and the extent of self-sorting. Studies with varying ratios of NHFs and H35s show that self-sorting proceeds with kinetics identical to self-assembly and that self-sorting proceeds with the same kinetics when the proportion of NHFs are varied over a 6 fold range (14% to 85%). This method is applicable to the study of the self-sorting behavior of other pairs of cell types as well as drugs that might accelerate or inhibit self-sorting. As such, the method can help bring a quantitative understanding to the dynamics of self-sorting and the cellular mechanisms that control it. Self-sorted 3D microtissues with heterotypic cell interactions that mimic key physiological functions of native tissue and organs may have applications in drug discovery, toxicity testing and cell therapy.

2.6 Acknowledgements

This work was funded, in part, by a grant from the Rhode Island Science and Technology Advisory Council and NIH R01EB008664-01A1.

2.7 Disclosure Statement

J.R.M has an equity interest in MicroTissues, Inc. This relationship has been reviewed and managed by Brown University in accordance with its conflict of interest policies.

2.8 References

1 Moscona, A. & Moscona, H. The dissociation and aggregation of cells from organ rudiments of the early chick embryo. *J Anat* **86**, 287-301 (1952).

2 Foty, R. A., Pfleger, C. M., Forgacs, G. & Steinberg, M. S. Surface tensions of embryonic tissues predict their mutual envelopment behavior. *Development* **122**, 1611-1620 (1996).

3 Duguay, D., Foty, R. A. & Steinberg, M. S. Cadherin-mediated cell adhesion and tissue segregation: qualitative and quantitative determinants. *Dev Biol* **253**, 309-323 (2003).

4 Foty, R. A., Forgacs, G., Pfleger, C. M. & Steinberg, M. S. Liquid properties of embryonic tissues: Measurement of interfacial tensions. *Phys Rev Lett* **72**, 2298-2301 (1994).

5 Foty, R. A. & Steinberg, M. S. The differential adhesion hypothesis: a direct evaluation. *Dev Biol* **278**, 255-263, doi:S0012-1606(04)00804-8 [pii]

10.1016/j.ydbio.2004.11.012 (2005).

6 Steinberg, M. S. Mechanism of tissue reconstruction by dissociated cells. II. Time-course of events. *Science* **137**, 762-763 (1962).

7 Steinberg, M. S. Reconstruction of tissues by dissociated cells. Some morphogenetic tissue movements and the sorting out of embryonic cells may have a common explanation. *Science* **141**, 401-408 (1963).

8 Forgacs, G., Foty, R. A., Shafrir, Y. & Steinberg, M. S. Viscoelastic properties of living embryonic tissues: a quantitative study. *Biophys J* **74**, 2227-2234, doi:S0006-3495(98)77932-9 [pii]

10.1016/S0006-3495(98)77932-9 (1998).

9 Krieg, M. *et al.* Tensile forces govern germ-layer organization in zebrafish. *Nat Cell Biol* **10**, 429-436, doi:ncb1705 [pii]

10.1038/ncb1705 (2008).

10 Dean, D. M. & Morgan, J. R. Cytoskeletal-mediated tension modulates the directed self-assembly of microtissues. *Tissue Eng Part A* **14**, 1989-1997, doi:10.1089/ten.tea.2007.0320 (2008).

11 Foty, R. A simple hanging drop cell culture protocol for generation of 3D spheroids. *J Vis Exp*, doi:2720 [pii]

10.3791/2720 (2011).

12 Kelm, J. M. & Fussenegger, M. Microscale tissue engineering using gravity-enforced cell assembly. *Trends Biotechnol* **22**, 195-202, doi:10.1016/j.tibtech.2004.02.002 S0167779904000484 [pii] (2004).

13 Klopper, A. V., Krens, G., Grill, S. W. & Heisenberg, C. P. Finite-size corrections to scaling behavior in sorted cell aggregates. *Eur Phys J E Soft Matter* **33**, 99-103, doi:10.1140/epje/i2010-10642-y (2010).

14 Graner, F. & Glazier, J. A. Simulation of biological cell sorting using a two-dimensional extended Potts model. *Phys Rev Lett* **69**, 2013-2016 (1992).

15 Mombach, J. C., Glazier, J. A., Raphael, R. C. & Zajac, M. Quantitative comparison between differential adhesion models and cell sorting in the presence and absence of fluctuations. *Phys Rev Lett* **75**, 2244-2247 (1995).

16 Beysens, D. A., Forgacs, G. & Glazier, J. A. Cell sorting is analogous to phase ordering in fluids. *Proc Natl Acad Sci U S A* **97**, 9467-9471, doi:97/17/9467 [pii] (2000).

17 Dean, D. M., Napolitano, A. P., Youssef, J. & Morgan, J. R. Rods, tori, and honeycombs: the directed self-assembly of microtissues with prescribed microscale geometries. *FASEB J* **21**, 4005-4012, doi:fj.07-8710com [pii] 10.1096/fj.07-8710com (2007).

18 Youssef, J., Nurse, A. K., Freund, L. B. & Morgan, J. R. Quantification of the forces driving self-assembly of three-dimensional microtissues. *Proc Natl Acad Sci U S A* **108**, 6993-6998, doi:1102559108 [pii] 10.1073/pnas.1102559108 (2011).

19 Rhee, S. Fibroblasts in three dimensional matrices: cell migration and matrix remodeling. *Exp Mol Med* **41**, 858-865, doi:10.3858/emm.2009.41.12.096 (2009).

20 Grinnell, F. & Petroll, W. M. Cell motility and mechanics in three-dimensional collagen matrices. *Annu Rev Cell Dev Biol* **26**, 335-361, doi:10.1146/annurev.cellbio.042308.113318 (2010).

2.9 Figures and Tables

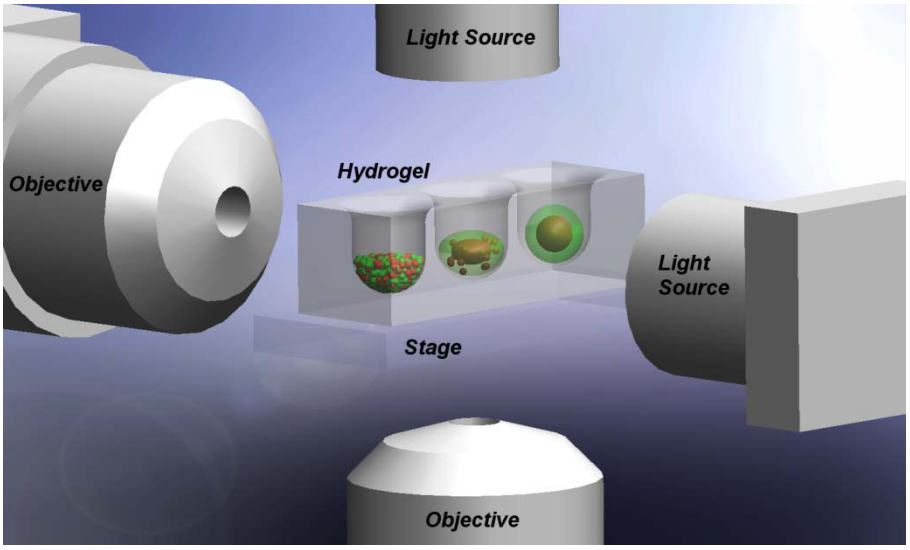

Figure 2-1. Experimental set-up of horizontal and normal view microscopy. Horizontal view (*z*) and normal view (inverted) (*x*,*y*) microscopy were used to capture time-lapse images of self-assembly and self-sorting.

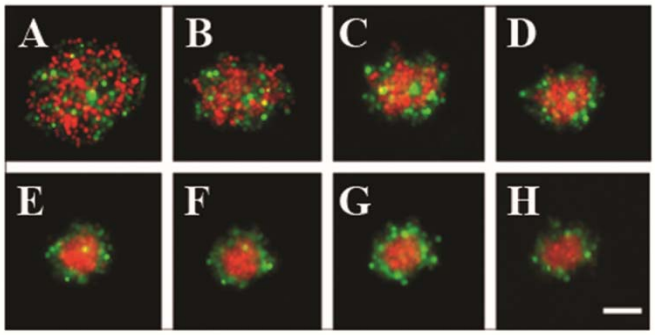

Figure 2-2. A mixture of NHFs and H35s self-assembled and self-sorted within 15 hours. A mixture (1:1) of NHFs (red) and H35s (green) self-assembled to form a 3D spheroid and self-sorted such that NHFs formed the central core and H35s formed the outer shell. Wide-field fluorescent images were obtained (A) immediately post seeding (0 hours), (B) 1 hour, (C) 2 hours, (D) 3 hours, (E) 6 hours, (F) 9 hours, (G) 12 hours, and (H) 15 hours after seeding. Scale bar = 100 µm.

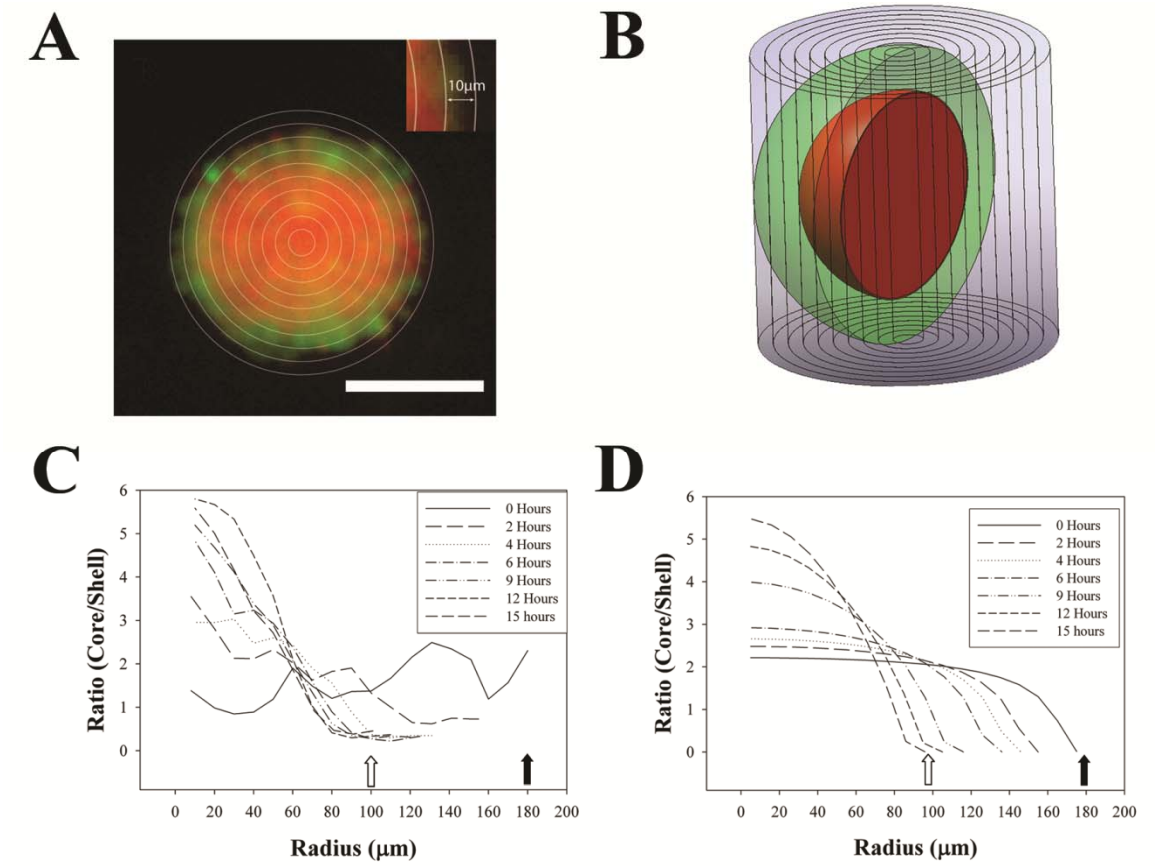

Figure 2-3. Quantification of self-sorting. For each wide-field fluorescent image, concentric 10 μm rings were drawn and the integrated fluorescence quantified for each 10 μm shell (inset). Shown is a fluorescent image of a 1:1 mix of NHFs (red) and H35s (green) after 6 hours of self-assembly (A). Each 10 μm shell, is a hollow cylinder through the spheroid as diagrammed (B). The center of the spheroid is a cylinder and not a hollow cylinder. The ratio of red to green fluorescence was computed for each cylinder of a 15 hour time series of fluorescent images of a 1:1 mix of NHFs and H35s. Starting *x, y* radii of 181 μm (filled arrow) and *z* radius of 30 μm changed to an *x, y* radii of 101 μm (open arrow) and *z* radius of 95 μm after 15 hours. Red to green ratio of each cylinder is plotted as a function of radial position (*x, y*) in the spheroid (C). As a reference, we calculated the expected red to green ratios of the radial cylinders of perfectly sorted spheroids of different sizes (D). This range of sizes coincided with the changes in shape of a spheroid self-assembling from a thin layer of cells to an oblate spheroid. Using the coefficient of determination, R^2, self-sorting was quantified by determining a goodness-of-fit of the experimental data of a spheroid of specific shape to the theoretical perfect sort of a spheroid of identical shape.

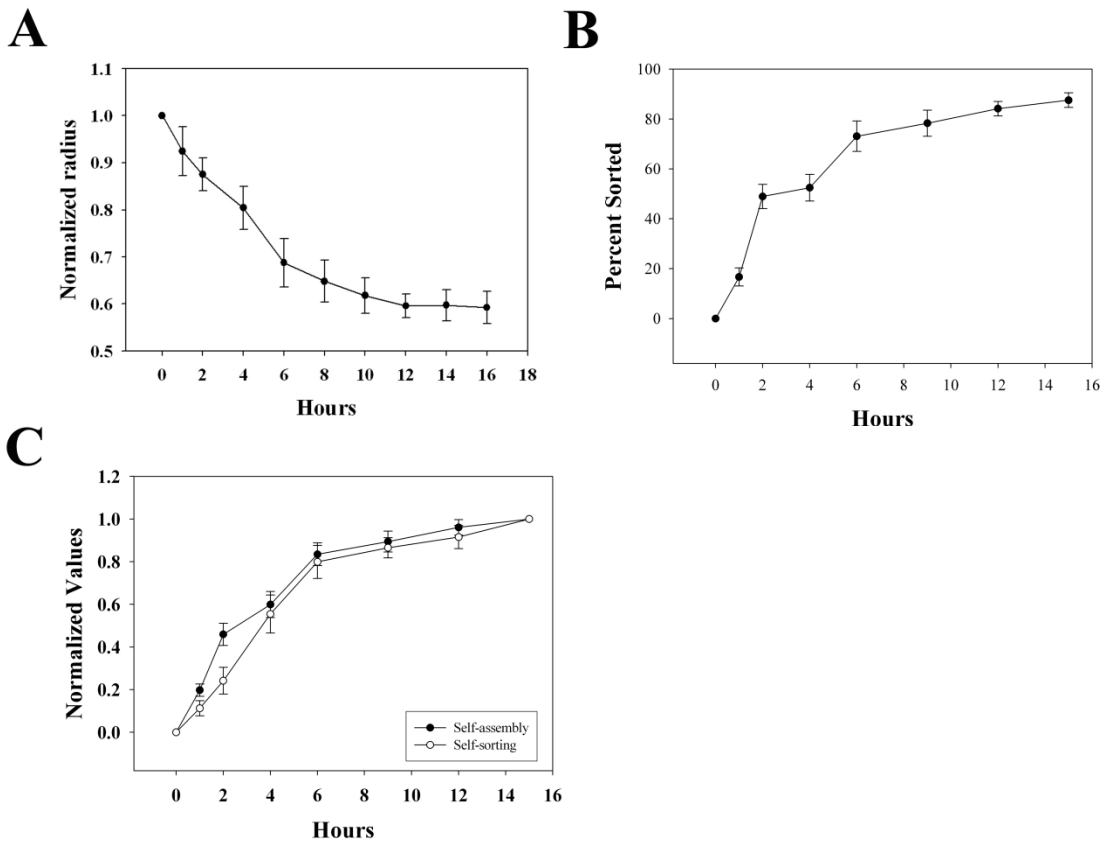

Figure 2-4. Self-assembly and self-sorting are coincident in time. Self-assembly (A) and self-sorting (B) of a 1:1 mix of NHFs and H35s were quantified. Self assembly was quantified by measuring the change in radius (*x*, *y* plane) of the spheroid over time. Self-sorting was quantified by determining a goodness-of-fit (R^2) of the experimental data of a spheroid of specific shape to the theoretical perfect sort of a spheroid of identical shape with values bounded between 0 and 1, with 1 representing a perfect sort. To directly compare their kinetics, self-assembly and self-sorting values were normalized to their starting and ending values and replotted (C). n=12 and error bars represent standard deviations.

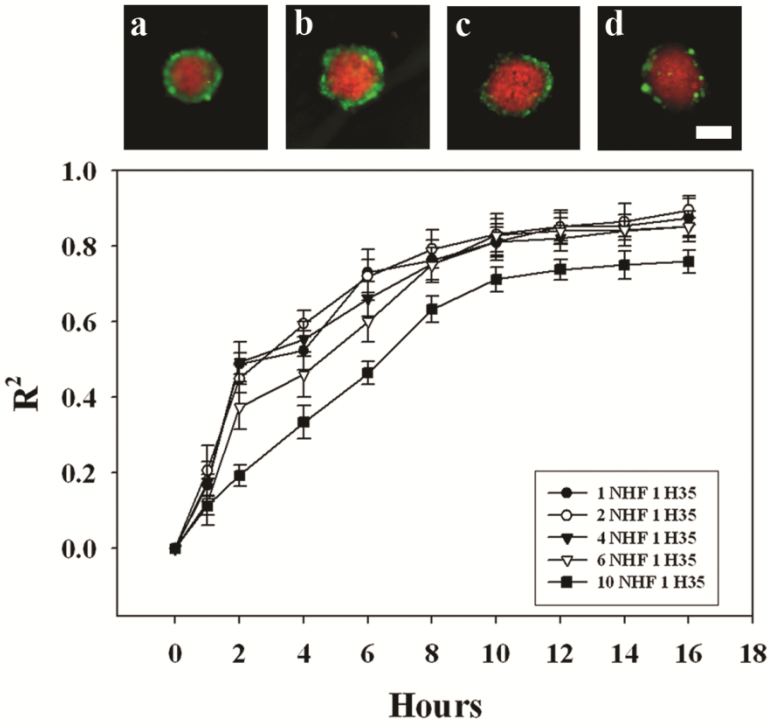

Figure 2-5. Increasing proportions of NHFs do not change the parameters of self-sorting. Varying ratios of NHFs and H35s were seeded in agarose hydrogels and self-assembly and self-sorting were quantified. 15 hour images (A) of NHF:H35 (red:green) ratios of 1:1 (A1), 2:1 (A2), 4:1 (A3), 6:1 (A4), and 10:1 (A5) show that even at higher proportions of NHF:H35, self-sorting still occured such that NHFs formed the inner core and H35s the outer shell. The kinetics of self-sorting for the 10:1 spheroids was significantly different from the other ratios (B). The general shape of the curve is the same, but the magnitude was decreased, as seen with the initial velocities ($P < 0.05$). All other parameters including the final extent of self-sorting, the time to reach 50 % sorted ($t_{1/2}$), and the time to reach steady state (t_{ss}) were not significantly different among the different ratios of NHF:H35. n=12 for all ratios, scale bar = 100 µm.

Ratio	Self-Sorting			Self-Assembly		
NHF:H35	v_o (% min^{-1})	$t_{1/2}$ (hrs)	Extent (%)	v_o (% min^{-1})	$t_{1/2}$ (hrs)	Extent (%)
1:10	0.4 ± 0.5	6.5 ± 0.5	64 ± 6	0.1 ± 0.2	6.4 ± 0.4	0.71 ± 0.04
1:06	0.4 ± 0.3	4.5 ± 0.7	84 ± 4	0.1 ± 0.3	4.1 ± 0.4	0.65 ± 0.05
1:04	0.4 ± 0.2	2.9 ± 0.2	84 ± 4	0.3 ± 0.4	2.9 ± 0.3	0.63 ± 0.07
1:02	0.4 ± 0.1	2.7 ± 0.3	86 ± 3	0.4 ± 0.2	2.3 ± 0.4	0.59 ± 0.05
1:01	0.4 ± 0.1	2.7 ± 0.3	88 ± 3	0.3 ± 0.1	2.9 ± 0.4	0.59 ± 0.03
2:01	0.4 ± 0.3	2.5 ± 0.4	90 ± 4	0.4 ± 0.2	2.5 ± 0.4	0.57 ± 0.03
4:01	0.4 ± 0.3	2.7 ± 0.2	86 ± 5	0.5 ± 0.3	2.6 ± 0.3	0.57 ± 0.04
6:01	0.4 ± 0.5	3.8 ± 0.3	85 ± 5	0.5 ± 0.3	2.9 ± 0.5	0.54 ± 0.03
10:01	0.4 ± 0.3	6.4 ± 0.6	80 ± 6	0.4 ± 0.3	2.7 ± 0.5	0.55 ± 0.04

Table 1. Kinetics and extent of self-sorting and self-assembly. Self sorting and self-assembly are coincident in time when spheroids are composed of between 14-85% NHFs.

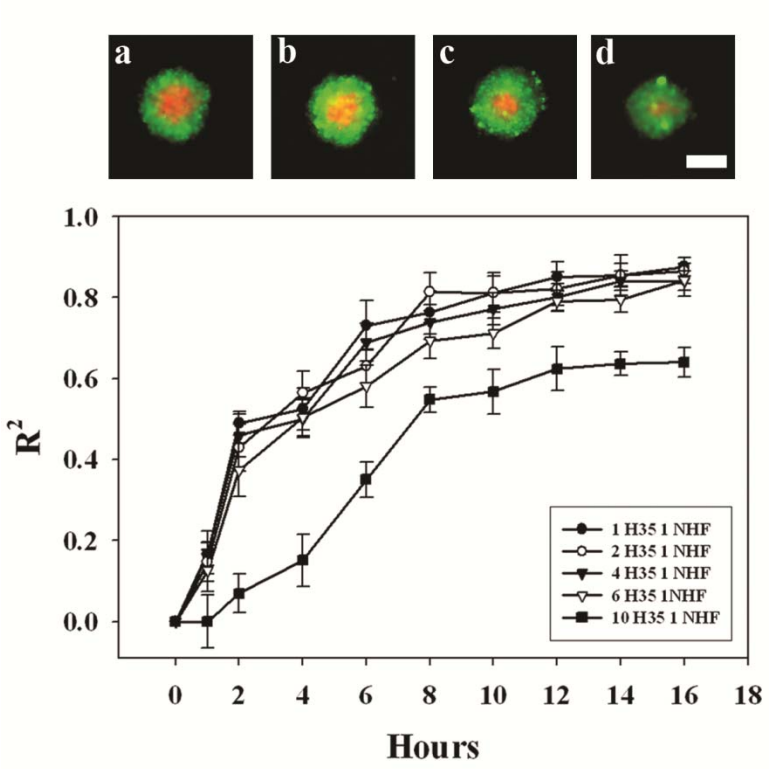

Figure 2-6. Increasing proportions of H35s reduce the rate and extent to which the cells self-sort. Images at 15 hours (A) showed at high proportions of H35:NHF (1:10) self-sorting was not as advanced as when the proportion of H35:NHF was lower. The kinetics of self-sorting for the 10:1 spheroids was significantly different from the other ratios (B) ($P < 0.01$), as well as for all other parameters including the final extent of self-sorting, the initial velocity (v_o), the time to reach 50 % sorted ($t_{1/2}$), and the time to reach steady state (t_{ss}). n=12 for all ratios, scale bar = 100 µm.

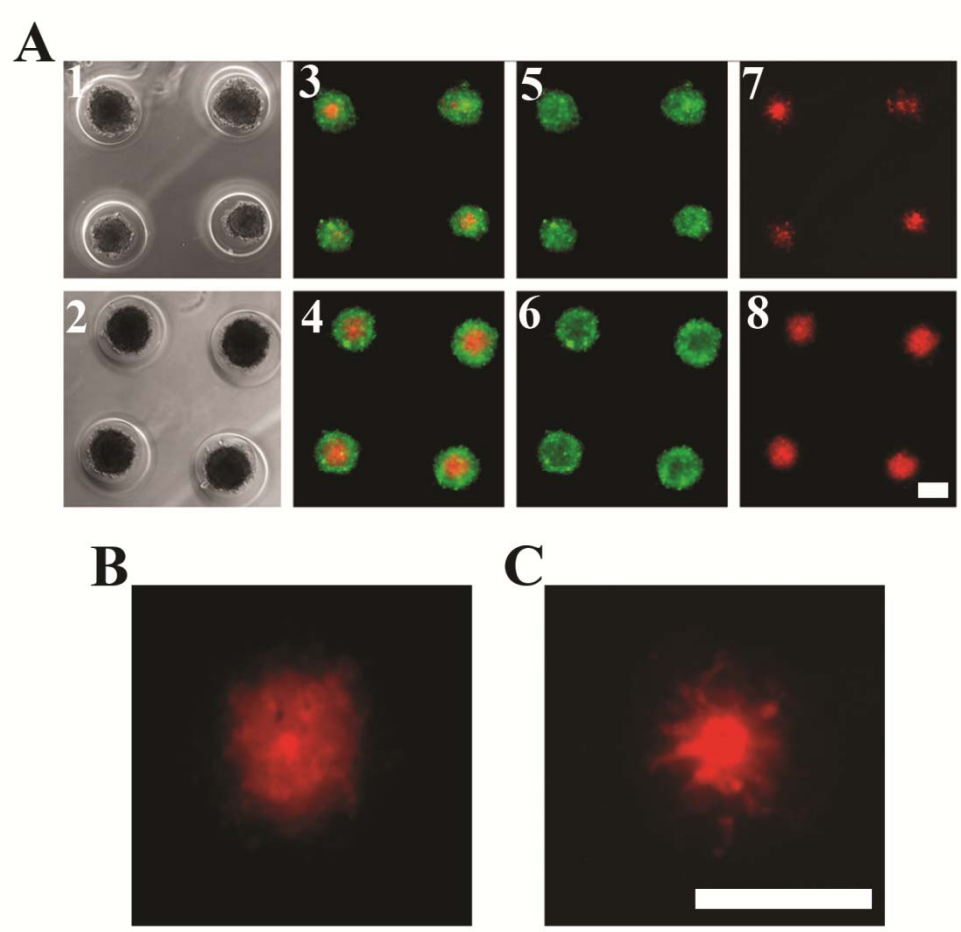

Figure 2-7. Heterotypic interactions increase when the proportion of NHFs is low. Phase contrast (A 1, 2) and fluorescence images (A 3-8) were obtained of NHF (red): H35 (green), 10:1 (A 1, 3, 5, 7) and 4:1 (A 2, 4, 6, 8) spheroids that self-assembled for 24 hours. Spheroids were similar in size and the corresponding mixed red and green fluorescence, green alone and red alone images show the spheroids have self-sorted. Higher magnification shows a tight NHF core in the 4:1 mix and looser NHF core with extensions into the H35 shell for the 10:1 mix. Scale bars = 200 µm.

Chapter 3

3. Multi-layer Spheroids to Quantify Drug Uptake and Diffusion in 3D

Toni-Marie Achilli, Stephanie McCalla, Julia Meyer, Anubhav Tripathi and Jeffrey R. Morgan

The following chapter is in revision after peer-review for Molecular Pharmaceutics.

3.1 Abstract

There is a need for new quantitative *in vitro* models of drug uptake and diffusion to help assess drug toxicity/efficacy as well as new more predictive models for drug discovery. We report a three-dimensional (3D) multi-layer spheroid model and a new algorithm to quantitatively study uptake and inward diffusion of fluorescent calcein via gap junction intercellular communication (GJIC). When incubated with calcein-AM, a substrate of the efflux transporter P-glycoprotein (Pgp), spheroids from a variety of cell types accumulated calcein over time. Accumulation decreased in spheroids over expressing Pgp (HEK-MDR) and was increased in presence of Pgp inhibitors (verapamil, loperamide, cyclosporin A). Inward diffusion of calcein was negligible in spheroids that lacked GJIC (OVCAR-3, SK-OV-3) and was reduced in the presence of an inhibitor of GJIC (carbenoxolone). In addition to inhibiting Pgp, verapamil and loperamide, but not cyclosporin A, inhibited inward diffusion of calcein, suggesting they also inhibit GJIC. The dose response curves of verapamil's inhibition of Pgp and GJIC were similar (IC_{50}: 8 μM). The method is amenable to many different cell types and may serve as a quantitative 3D model that more accurately replicates *in vivo* barriers to drug uptake and diffusion.

3.2 Abbreviations

ABC	ATP binding cassette
ADME-Tox	absorption, distribution, metabolism, excretion, and toxicity
CBX	carbenoxolone
DMEM	Dulbecco's modified Eagle's medium
FBS	fetal bovine serum
GJIC	gap junctional intercellular communication
Pgp	P-glycoprotein
RPMI	Roswell Park Memorial Institute medium

3.3 Introduction

A quantitative understanding of drug uptake and diffusion within tissues is an important aspect of successful drug development. At the cellular and multi-cellular level, diffusion is the primary mechanism for drug movement into cells, avascular tissues, and tumors (1, 2) However, diffusion is tightly controlled by biological barriers including the plasma membrane, transport proteins, vesicular systems, cell adhesion molecules, gap junctions, and cellular efflux pumps (1-3). The ability to cross these barriers *in vivo* is a key determinant of a drug's absorption, distribution, metabolism, excretion, and toxicity (ADME-Tox), and, ultimately, the success of the drug (4-7). From the route of administration to the site of action, a drug encounters barriers and transporters before reaching its target. The largest family of transporters is the ATP binding cassette (ABC) transporters, and P-glycoprotein (Pgp) is a member of this family (7-9). The Pgp transporter is localized to the plasma membrane of cells and is present in both normal and diseased tissues. Normally, Pgp helps to protect sensitive tissues from toxicity by facilitating efflux and preventing the intracellular accumulation of Pgp substrates (8-15). However, in diseased tissues and the cells of solid tumors, Pgp is sometimes up-regulated, increasing resistance to anti-cancer chemotherapeutics (10, 11). Many drugs of various pharmacological classes are substrates and sometimes inhibitors of this pump (8, 9).

Numerous inhibitors of Pgp have been identified, characterized *in vitro*, and evaluated in the clinic. Although effective *in vitro*, Pgp inhibitors have proven ineffective in the clinic, or have unexpected drug-drug interactions leading to increased toxicity (16, 17). There are three principal *in vitro* methods to characterize Pgp inhibitors: measurement of the efflux of radio-labeled compounds by a mono-layer of cells,

measurement of drug-stimulated ATPase activity of Pgp protein, and measurement of calcein-AM uptake by a mono-layer of cells (18-21). Mono-layers can measure inhibition of Pgp, but drug uptake and diffusion in these two-dimensional (2D) systems does not accurately replicate the complexity found in a 3D multi-cell layer environment. The diffusion distance for a drug into a mono-layer is relatively short compared to *in vivo* tissues, and biological barriers are not adequately replicated. Current methods to quantify 3D uptake and diffusion in tissues are cumbersome and include the use of microelectrode sensors or radio-labeled molecules, and are not amenable to higher throughput analyses (21-25).

In this paper, we have developed a new 3D multi-layer spheroid model to quantitatively study uptake and diffusion. Using calcein-AM and its fluorescent derivative, calcein, along with wide field fluorescent images, we have calculated the uptake and diffusion of calcein into spheroids of a variety of different cell types. Accumulation of total spheroid calcein was decreased when spheroids over expressed Pgp and was increased when spheroids were treated with known inhibitors of Pgp (verapamil, loperamide, and cyclosporin A). Inward diffusion of calcein was negligible in spheroids that lacked gap junctional intercellular communication (GJIC) and was reduced when spheroids were treated with a drug (carbenoxolone) known to block GJIC. We also found that two of the Pgp inhibitors (verapamil, loperamide) also inhibited inward diffusion of calcein, suggesting they are also inhibitors of GJIC.

3.4 Experimental Section

Design, Fabrication, and Casting of Micro-molds

Micro-molds used to form hydrogels for forming spheroids were designed using computer design software (SolidWorks Corporation, Concord, MA)(26, 27) Designs used for side-view microscopy contained a single row of 21 recesses with rounded bottoms, each recess 400 μm in diameter and 800 μm in depth. Wax molds were produced with a ThermoJet® rapid prototyping machine (3D Systems Corporation, Valencia, CA). Polyacrylamide gels were cast from the wax molds. All chemicals were purchased from Sigma Aldrich (St. Louis, MO). A mixture of acrylamide/*bis*-acrylamide (29:1 ratio), ammonium persulfate (APS), 0.5 M Tris buffer (pH 6.8), and Dulbecco's modified Eagle's medium (DMEM) (Invitrogen, Carlsbad, CA) was degassed. N,N,N',N'-tetramethylethlyenediamine was added to initiate polymerization. The solution was pipetted into the wax mold and covered with a cover slip to create a flat bottom on the gel. After 10 minutes, the hydrogel was removed from the mold, washed several times with DMEM, and incubated overnight in DMEM.

Cell Culture and Spheroid Formation

KGN cells, a human granulosa cell line, were grown in DMEM (28). OVCAR-3 and SK-OV-3 cells were grown in Roswell Park Memorial Institute medium (RPMI; Invitrogen). MCF-7 cells were kindly provided by Dr. Gottesman, NIH Bethesda, MD, and maintained in DMEM (29). HEK control and HEK transfected cells were obtained from Dr. Robey, NIH Bethesda, MD and cultured in EMEM (30). Both media were supplemented with 10% fetal bovine serum (FBS) (Thermo Fisher Scientific, Waltham,

MA) and 1% penicillin/streptomycin and grown at 37°C and 10% CO_2. Cells were trypsinized using 0.05% trypsin and resuspended to the desired cell concentration. Spheroids that were pre-stained were formed from cells incubated with 5 μM CellTracker™ Red CMPTX, CellTracker™ Green CMFDA, or CellTracker™ Blue CMAC (Invitrogen) in serum-free DMEM for 1 hour prior to trypsinization. 75 μl of the cell suspension was pipetted into the seeding chamber of each gel. Cells were allowed to settle for 20 minutes and 4 mL of medium was added. Cells self-assembled for 24 hours to form spheroids before experimentation.

Microscopy

Horizontal view microscopy was used to measure the height (z) of the spheroid from a Mitutouo FS-110 microscope altered to lie on its back. Samples were placed on a translational stage and brightfield images were taken through the eyepiece using a Nikon Coolpix 900 camera. For standard, x-y view images, a Carl Zeiss Axio Observer Z1 equipped with an AxioCam MRm camera (Carl Zeiss MicroImaging, Thornwood, NY), an Xcite 120 XL mercury lamp (Exfo Life Sciences Division, Mississauga, Ontario), and an incubation chamber (37ºC, 10% CO_2) was used to obtain brightfield, phase contrast, and epi-fluorescent images.

Image Analysis

Quantitative image analysis was performed using a custom MATLAB (Mathworks, Natick, MA) program. Briefly, fifty evenly spaced radii were drawn across each spheroid and fluorescence at each pixel was averaged. Background fluorescence

outside the spheroid was subtracted, taking into account that the fluorescence surrounding the spheroids decreased exponentially and was thus different for different points within the spheroid. Total spheroid fluorescence was determined by the integration of the fluorescent profiles (**Equation 2**). To compare data across experiments, we normalized the spheroids to the fluorescence per depth of single cells at the final time point.

The height (h) at each point in the spheroid was calculated using the formula for an ellipse with half-width a and half-height b, such that:

$$h(x) = b\sqrt{1-\left(\frac{x}{a}\right)^2} \tag{1}$$

The fluorescent intensity at each height was averaged over all spheroids stained with CellTracker™ dyes [red (n = 52), green (n = 74), and blue (n = 60)]. The total fluorescence at each point is the integrated fluorescence of all cells below it, expressed as:

$$F_t(x) = \int_0^{h(x)} C(x,z)\alpha p^2 dz \tag{2}$$

where $C(x, z)$ is the concentration of the fluorophore along the y = 0 plane, α is the emitted fluorescence per mole of fluorophore, and p is the resolution of one pixel (2 μm x 2 μm). The uniformly pre-stained spheroids have constant fluorophore concentration, C_o. The above integral shows that the total fluorescence is linearly related to the height of the spheroid below each point:

$$F_t = C_o \alpha p^2 h \tag{3}$$

Uptake of Calcein-AM and Diffusion of Calcein

To measure uptake and inward diffusion of calcein, medium was removed from the hydrogels containing self-assembled spheroids (24 hours), and replaced with serum-free DMEM containing 1 μM calcein-AM (Invitrogen). Fluorescent imaging of calcein began immediately and images were taken at regular intervals over 135 minutes at 37°C and 10% CO_2. To measure loss of calcein, hydrogels containing spheroids that had been incubated with calcein-AM for 135 minutes, thus loading the spheroids with calcein, were rinsed with DMEM and incubated in DMEM without calcein-AM. Images were taken once per hour for 11 hours, at 37°C and 10% CO_2.

Drug Treatment to Block P-Glycoprotein and Gap Junctions

Stock solutions of verapamil monohydrochloride hydrate, loperamide hydrochloride, and cyclosporin A (Sigma) (5 μg/ml, 100 μM, and 25 μM, respectively) were used to make working solutions in serum-free DMEM. Hydrogels were equilibrated with a drug-containing medium overnight at 37°C and 10% CO_2, and spheroids were self-assembled for 24 hours in their respective drug concentration. At these drug concentrations, self-assembly kinetics were unaltered. A working solution of carbenoxolone (CBX)(Sigma) was prepared by diluting appropriate volumes of a 10 mM stock solution into serum-free medium. Spheroids were assembled for 24 hours and then pre-treated with CBX for 5 hours prior to adding calcein-AM for the uptake assay. Medium containing drug and calcein-AM were used for the uptake assay.

Statistical Analysis

Two experimental groups were tested for significant variability between sample means using analysis of variance (ANOVA). If significant differences were established, we performed a Bonferroni *t*-test to determine significance.

3.5 Results

Determining the Critical Height for Imaging Spheroids

To quantify the distribution of fluorescent molecules in 3D spheroids using wide field fluorescence, we determined the limits to spheroid size (**Figure 3-1**). Pre-stained (CellTracker^{TM} dyes) mono-dispersed cells were seeded onto a micro-molded nonadhesive hydrogel, whereon they self-assembled spheroids after 24 hours. Using side view and conventional view microscopy, we obtained fluorescent images and *x*, *y*, *z* measurements of a size range of spheroids. Peak fluorescence intensity at the center or thickest location of the spheroid showed a linear relationship between spheroid height and fluorescence for all three fluorophores up to a critical spheroid height of 205 μm implying that 100% of the emitted fluorescent light (red, blue, green) was captured. Subsequent studies used spheroids below this critical height. We also used a MATLAB algorithm to generate an average 2D radial profile of fluorescence intensity from fifty radial lines and this average radial profile was parabolic, consistent with the predicted theoretical profile (**Equation 1**).

Uptake and Diffusion by Multi-layer Spheroids

To measure uptake and diffusion, spheroids were incubated with calcein-AM (1 μM) and images of fluorescent calcein were taken every fifteen minutes for 135 minutes (**Figure 3-2**). Calcein fluorescence in the entire spheroid increased rapidly over time and started to plateau after about 60 minutes. We used our MATLAB algorithm to generate an average 2D radial profile of fluorescence at each time point and this time series also

showed that total calcein fluorescence increased throughout the 135 minutes (area under curve). However, none of the 2D radial profiles attained the full parabolic curve seen with uniformly stained spheroids. Maximum calcein fluorescence was not in the center of the spheroid (point of greatest cell number), rather, it was located near the outer edge of the spheroid. This indicated that as uptake and inward diffusion occurred over time, the highest concentration of calcein was in the outer layer of the spheroid and calcein concentration decreased towards the spheroid core.

To deconvolve this fluorescent signal into an average 3D radial profile, the spheroid was estimated as a series of concentric spheres (multi-layers). Each layer (shell) was 14 μm in width and contained a homogenous concentration of fluorescent calcein (**Figure 3-2**). The total fluorescence $f(i)$ at X_i layer is sum of the fluorescence contribution from all shells at X_i. Mathematically, we can write the total fluorescence as

$$f(i) = 2\sum_{j=1}^{i} f_{norm}(j)\left[h(i+1, j) - h(i+1, j+1)\right] \quad (4)$$

Here, $f_{norm}(j)$ is the fluorescence/height in the ith shell and $h(i, j)$ is the height at point (X_i, Y_j). Note $h(i,i) = 0$ lies at the centerline of the spheroid. Hence, we determined $f_{norm}(i)$ by sequentially subtracting the fluorescence due to inner shells from the total fluorescence $f(i)$ at X_i. Equation (4) results in the following iterative formula:

$$f_{norm}(i) = \frac{1}{h(i+1,i)}\left[\frac{f(i)}{2} - \sum_{j=1}^{i-1} f_{norm}(j)\left[h(i+1, j) - h(i+1, j+1)\right]\right] \quad (5)$$

This analysis was used to plot calcein concentration as a function of 3D radius. The core was taken as ≥14 μm from the center in the smallest dimension to ensure the core contained whole cells. Even at later time points, the concentration of calcein in the core did not reach the same concentration as the outer shell, indicative of cellular barriers to diffusion. As calcein-AM is taken up by the cells of the outer spheroid layer, some is pumped out by the action of Pgp and some is converted to fluorescent calcein by intercellular esterases. This intercellular calcein diffuses to the inner layers of the spheroid via GJIC. It is important to note that calcein-AM surrounds the spheroid and this spheroid (r = 100 μm) occupies a volume of 4×10^6 μm^3. In the absence of a spheroid and the barriers it creates, calcein-AM and calcein would complete their diffusion into this volume of medium (Diffusivity = 260 & 500 $\mu m^2/s$, respectively) within ~ $t = r^2/D$ ~10-20 seconds. Thus, the spheroid is a complex barrier to calcein-AM and calcein diffusion.

To measure uptake and diffusion in spheroids of other cell types, we formed spheroids from HEK, MCF-7, OVCAR-3 and KGN cells, incubated them with calcein-AM and measured calcein over time from fluorescent images (**Figure 3-3**). From this time series, we computed total calcein fluorescence in the entire spheroid and the 2D and 3D radial profiles of calcein fluorescence. For all spheroids, total calcein accumulated rapidly over time and started to plateau after about 40- 60 minutes. However, the 2D and 3D radial profiles of calcein fluorescence were significantly different depending on cell type. KGN, MCF-7 and HEK spheroids showed the greatest diffusion of calcein into the core, whereas OVCAR-3 spheroids showed little if any calcein fluorescence in the core with most of the calcein confined to the outer layer. Spheroids made with SK-OV-3

cells, another ovarian cancer cell line that lacks GJIC had profiles similar to OVCAR-3 cells with little diffusion of calcein into the spheroid core (data not shown)(31).

To determine the effects of efflux pump over expression, we performed the calcein assay with HEK-MDR cells transfected with Pgp, an efflux pump known to transport calcein-AM (**Figure 3-4**). The rate of increase in total spheroid calcein fluorescence was significantly lower in spheroids of HEK-MDR cells versus parental HEK spheroids. In the presence of verapamil, an inhibitor of Pgp, total spheroid calcein fluorescence increased in untransfected cells which have some endogenous Pgp expression and increased significantly in HEK-MDR cells.

Multi-layer Uptake and Diffusion in the Presence of Pgp and GJIC Inhibitors

To determine the effects of verapamil on the diffusion of calcein, we measured the radial distribution of calcein (**Figure 3-5)**. A time series of 2D radial profiles showed that total spheroid fluorescence increased with verapamil treatment, consistent with inhibition of Pgp. However, the shape of the 2D radial profiles of verapamil-treated samples was different from untreated controls. Fluorescence of the outer layer versus the core was increased indicating more calcein in the outer layer of the drug-treated samples. Our 3D analysis showed that, in addition to increasing the total calcein in a spheroid, verapamil treatment altered the concentration gradient within the spheroid. Calcein concentration was increased in the outer layer, as would be expected by inhibition of the Pgp, but calcein concentration was not elevated in the core as a result of the increased levels in the outer layer. High levels of calcein in the outer layer should lead to increased levels in the core, but surprisingly, our 3D analysis showed that calcein levels in the core were higher in untreated samples than in those treated with verapamil.

To determine if other inhibitors of Pgp had similar effects, we tested loperamide and cyclosporin A (**Table I**). Total calcein in spheroids treated with loperamide (5 μM), cyclosporin A (25 μM) and verapamil (25 μM) was significantly increased compared to untreated controls, consistent with their activities as inhibitors of Pgp. Further, compared to untreated controls, levels of calcein were significantly increased in the outer shell of all drug treated spheroids.

To determine if inward diffusion of calcein was altered by any of the Pgp inhibitors, we used our 3D analysis to determine what fraction (%) of the total calcein was located in the outer shell versus the inner core. In verapamil and loperamide treated samples, the percentage of calcein in the outer shell was increased compared to control, while the percentage of calcein in the core was decreased. After treatment with cyclosporin A, calcein concentration increased in all compartments, such that the percentage of calcein in the shell and core compartments were not significantly different from their respective compartments in untreated samples. This indicates that cyclosporin A did not alter inward diffusion of calcein.

Since diffusion of calcein requires GJIC, we tested the effects of CBX (CBX) an inhibitor of gap junctions (32). As expected, CBX treatment decreased inward diffusion of calcein. After 135 minutes of uptake, only 0.5 ± 2 % of the total calcein was located in the core of spheroids treated with CBX (100 μM) versus 15 ± 3% in untreated spheroids (n = 18). Likewise, the fraction of calcein in the outer shell of CBX treated spheroids was increased versus untreated controls (52 ± 4% versus 27 ± 3%). In addition to altering inward diffusion of calcein, surprisingly, we found that CBX treatment increased the total amount of calcein fluorescence in the entire spheroid. After 135 minutes, total calcein in

CBX treated spheroids was increased 2.3 ± 0.4 fold versus untreated spheroids, suggesting that in addition to being an inhibitor of GJIC, CBX also inhibits Pgp.

Since verapamil and CBX inhibited both Pgp and GJIC, we did a dose response to compare their potencies (**Figure 3-6**). Spheroids were incubated with calcein-AM in the presence of varying doses of verapamil or CBX and fluorescent images obtained after 75 minutes. The 3D radial profiles revealed that increasing concentrations of verapamil and CBX both resulted in increased calcein uptake (area under curve), but that calcein was more localized to the outer shell with CBX treatment (shape of curve). To determine the dose response with respect to inhibition of Pgp, we plotted total spheroid calcein (n=15) as a function of drug concentration. For verapamil, half-maximal response was 8.5μM, whereas for CBX half-maximal response was 81μM. There was a linear dose response for CBX versus verapamil which rose rapidly and reached a plateau.

We used the same data to determine the dose response with respect to inhibition of GJIC by calculating a drug's ability to increase the fraction of calcein compartmentalized to the outer shell. For verapamil, half-maximal response with respect to GJIC inhibition was 8.6μM, similar to the concentration that elicited half-maximal inhibition of Pgp. For CBX, half-maximal response for GJIC inhibition was 9.4μM, significantly lower than the concentration that elicited half-maximal inhibition of Pgp.

To rule out the possibility that verapamil's inhibition of GJIC might be mediated by verapamil's calcium channel-blocking activity and mediated via a change in intracellular calcium, we tested nitrendipine, a highly-specific calcium channel blocker. Nitrendipine had no effect on calcein compartmentalization (data not shown).

To determine if CBX might be increasing total spheroid calcein by slowing the loss of calcein rather than by inhibiting Pgp, we measured the kinetics of calcein loss (**Figure 3-7**). Spheroids with and without CBX treatment were incubated with calcein-AM for 135 minutes. Medium with calcein-AM was then removed, replaced with fresh medium and fluorescent images taken for 20 hours to quantify the rate of calcein loss. Calcein fluorescence decreased at the same initial rate for control and CBX treated spheroids with half-lives of 5.3 hours and 5.9 hours respectively.

3.6 Discussion

Drug uptake, transport, diffusion and elimination from tissues are important properties governing the efficacy and potential toxicity of drugs and drug candidates. Efflux transporters, such as Pgp, are well-known regulators of drug bioavailability and their modulation, either intentionally via inhibitors or unintentionally via the side effects of certain drugs, can have profound pharmacological effects (4-7). Some efflux transporters can be up-regulated by solid tumors causing multi-drug resistance, so there is an active interest to identify more effective inhibitors for use in chemotherapy (10, 11). Thus, there is a need for new *in vitro* models to predict drug toxicity and unwanted drug-drug interactions and a need for models to discover new and more effective inhibitors of efflux transporters associated with multi-drug resistance. Although mono-layers of cells have been useful for defining some of these transport parameters and have been used to identify inhibitors of efflux pumps, such as Pgp (11, 18, 21), there is growing recognition that 2D cell culture may not adequately replicate the biological complexities of the 3D *in vivo* environment.

3D models have been used to investigate transport properties, molecular gradients, and cellular gradients, but often these methods require complex experimental and analytical procedures such as two-photon microscopy (33), radio-labeled probes (23), tissue sectioning (24), or mathematical models (34). The method described here readily lends itself to quantitative uptake and diffusion studies. Spheroids are uniform in size and spheroid geometry is well defined because in addition to measurements of the *x, y* dimensions, the *z* dimension is measured. Spheroids are surrounded by cell culture medium, thus uptake occurs uniformly around the entire surface area. Spheroids are all formed on the same optical plane, making it easy to obtain a time series of fluorescent

images from which data on kinetics can be obtained. Precise measurements of a spheroid's geometry and its radial symmetry, allowed us to develop an algorithm to calculate the radial distribution of a fluorescent molecule from wide field fluorescent images.

In this paper, we've used this model to quantify both the uptake and diffusion of fluorescent calcein. Calcein-AM, the non-fluorescent precursor of calcein is a substrate of the Pgp efflux pump and fluorescent calcein diffuses into the spheroid via GJIC connecting cell layers (35). We measured total calcein fluorescence in the entire spheroid and we measured the diffusion of calcein into the spheroid. Spheroids formed from a variety of cell lines all accumulated fluorescent calcein with time, but they differed with regards to their rate of calcein accumulation. When compared to untransfected control HEK spheroids, the rate of calcein accumulation was low in transfected HEK-MDR spheroids over expressing Pgp. This reduced rate could be reversed by the addition of verapamil, an inhibitor of Pgp. Likewise, when other inhibitors of Pgp were tested (loperamide and cyclosporin A), the rate of accumulation of total spheroid calcein was increased. Although all spheroids accumulated calcein, they differed with regards to how much calcein diffused into the core of the spheroid. Calcein failed to diffuse into spheroids of cells that lack GJIC such OVCAR-3 and SK-OV-3 (31). Likewise, when spheroids were treated with CBX, a well known inhibitor of GJIC (32, 35), calcein diffusion was also inhibited.

By quantifying both total spheroid calcein and the diffusion of calcein into the spheroid, we observed previously uncharacterized activities of some of the drugs we tested. For example, verapamil, loperamide, and cyclosporin A, are all well know

inhibitors of Pgp and all three increased total calcein in the spheroid. However, quantification of calcein diffusion into the spheroid showed that verapamil and loperamide inhibited diffusion, whereas cyclosporin A did not, calcein diffusion was the same as untreated controls. These results suggest that verapamil and loperamide also inhibit GJIC, an activity and novel finding not previously reported for these drugs.

Another unexpected activity that was found because we quantified both total spheroid calcein and calcein diffusion was CBX's inhibition of Pgp. As expected, CBX inhibited calcein diffusion by blocking GJIC, however, CBX also increased total spheroid calcein, consistent with inhibiting Pgp. We ruled out the possibility that CBX mediated its effects by decreasing the loss of total spheroid calcein. When we used both assays to compare the dose responses of verapamil and CBX, we found that while both drugs inhibited Pgp and GJIC, verapamil was more potent at inhibiting Pgp, whereas CBX was more potent and more effective at inhibiting GJIC. Verapamil is a competitive inhibitor of Pgp (8, 9) and interestingly, the dose response curve of verapamil's inhibition of Pgp and GJIC were very similar. The same dose (8 μM) elicited half maximal response for both activities. All transporters on KGN spheroids have not been fully characterized, nor have we determined if Pgp expression is in any way polarized in KGN spheroids. In addition to Pgp, calcein-AM is a substrate for MRPs/Mrps and calcein is a substrate for MRP. Endogenous levels of these other transporters could affect the level and distribution of calcein in the KGN spheroids as well as the response to various inhibitors. Doses of inhibitors were chosen with Pgp in mind. To help rule out the possibility that diffusion of Pgp inhibitors into the spheroids might be limiting, we exposed our mono-dispersed cells continuously to verapamil, loperamde and cyclosporin A while they were

self-assembling spheroids and when the spheroids were tested for uptake. We were unable to expose mono-dispersed cells to CBX because as we've shown previously, CBX's action on connexons disrupts self-assembly. (36)

Verapamil, loperamide and cyclosporin A are well known inhibitors of Pgp, but they are used clinically for other purposes at significantly lower doses. Verapamil blocks voltage-dependent calcium channels and is used to treat hypertension (37). When tested for the treatment of multi-drug resistance, low doses were ineffective and high doses caused cardiotoxicity (17, 38, 39). Interestingly, the KGN cells we tested express connexon 43, the same connexon expressed by cardiomyocytes (40) Loperamide is an opioid-receptor agonist whose primary use is the treatment of diarrhea, but it can also affect calcium levels and is a substrate for and an inhibitor of Pgp (18). Cyclosporin A, an immunosuppressant used to prevent graft rejection, had the most success with multi-drug resistance of retinoblastoma (41, 42). However, its immunosuppressant activity precluded further use and its non-immunosuppressant derivative has had little success in the clinic (43).

The 3D model described here can easily be extended to other cell types. We and others have shown that numerous cell types including primary human cells will self-assemble 3D spheroids including cardiomyocytes in this system (44). Moreover, mixtures of two different cell types often self-sort during self-assembly with one cell type forming the inner core and the other cell type forming the outer coating of the spheroid (45). These layered spheroids may be useful for replicating heterotypic cell interactions seen in more physiologic barriers to drug uptake. Lastly, 3D models may be useful for discovering new more effective inhibitors of efflux transporters responsible for multi-

drug resistance and helpful in the early identification of possible side effects and drug-drug interactions of drug candidates.

3.7 Conclusion

Multi-cellular spheroids more accurately replicate *in vivo* barriers to drug uptake and diffusion than 2D monolayers of cells. The quantitative model described here measures uptake and diffusion of calcein through multiple cell layers of a 3D spheroid and assesses the activities of both Pgp and GJIC with respect to efflux of calcein-AM and diffusion of calcein. The model has uncovered previously unknown effects of some drugs, is amenable to many different cell types and may be useful for the assessment of drug toxicity as well as a model for drug discovery.

3.8 Acknowledgements and Disclosures

This work was funded in part by the National Institute of Health (R01EB008664-01A1) and seed funds from the Johnson & Johnson Corporate Office of Science & Technology and the Brown Technology Ventures Office. Authors would also like to thank partial support from National Aeronautics and Space Agency (NASA) and the generous support of Donna McGraw Weiss '89 and Jason Weiss. J.R.M has an equity interest in Microtissues, Inc. This relationship has been reviewed and managed by Brown University in accordance with its conflict of interest policies.

3.9 References

1. Jang, S. H., Wientjes, M. G., Lu, D. & Au, J. L. Drug delivery and transport to solid tumors. *Pharm. Res.* **2003**, *20*, 1337-1350.
2. Minchinton, A. I. & Tannock, I. F. Drug penetration in solid tumours. *Nat. Rev. Cancer* **2006**, *6*, 583-592.
3. Elliott, N. T. & Yuan, F. A review of three-dimensional in vitro tissue models for drug discovery and transport studies. *J. Pharm. Sci.* **2011**, *100*, 59-74.
4. Szakacs, G., Varadi, A., Ozvegy-Laczka, C. & Sarkadi, B. The role of ABC transporters in drug absorption, distribution, metabolism, excretion and toxicity (ADME-Tox). *Drug Discov Today* **2008**, *13*, 379-393.
5. Shugarts, S. & Benet, L. Z. The role of transporters in the pharmacokinetics of orally administered drugs. *Pharm. Res.* **2009**, *26*, 2039-2054.
6. Varma, M. V., Ashokraj, Y., Dey, C. S. & Panchagnula, R. P-glycoprotein inhibitors and their screening: a perspective from bioavailability enhancement. *Pharmacol. Res.* **2003,** *48*, 347-359.
7. Giacomini, K. M. *et al.* Membrane transporters in drug development. *Nat. Rev. Drug Discov.* **2010**, *9*, 215-236.
8. Borst, P. and Oude Elferink, R. Mammalian ABC transporters in health and disease *Annu. Rev. Biochem*. **2002**, *71*, 537-592.
9. Ambudkar, S. V. *et al.* Biochemical, cellular, and pharmacological aspects of the multidrug transporter. *Annu. Rev. Pharmacol. Toxicol.* **1999**, *39*, 361-398.
10. Fojo, A. T. *et al.* Expression of a multidrug-resistance gene in human tumors and tissues. *Proc. Natl. Acad. Sci. U S A* **1987**, *84*, 265-269.
11. Szakacs, G., Paterson, J. K., Ludwig, J. A., Booth-Genthe, C. & Gottesman, M. M. Targeting multidrug resistance in cancer. *Nat. Rev. Drug Discov.* **2006**, *5*, 219-234.
12. Cecchelli, R. *et al.* Modelling of the blood-brain barrier in drug discovery and development. *Nat. Rev. Drug Discov.* **2007**, *6*, 650-661.
13. Fellner, S. *et al.* Transport of paclitaxel (Taxol) across the blood-brain barrier in vitro and in vivo. *J. Clin. Invest.* **2002**, *110*, 1309-1318.
14. Fromm, M. F. Importance of P-glycoprotein at blood-tissue barriers. *Trends Pharmacol. Sci.* **2004**, *25*, 423-429.
15. Letrent, S. P. *et al.* P-glycoprotein-mediated transport of morphine in brain capillary endothelial cells. *Biochem. Pharmacol.* **1999**, *58*, 951-957.

16. Sikic, B. I. *et al.* Modulation and prevention of multidrug resistance by inhibitors of P-glycoprotein. *Cancer Chemother. Pharmacol.* **1997**, *40* Suppl, S13-19 (1997).
17. Aszalos, A. Drug-drug interactions affected by the transporter protein, P-glycoprotein (ABCB1, MDR1) II. Clinical aspects. *Drug Discov. Today* **2007**, *12*, 838-843.
18. Polli, J. W. *et al.* Rational use of in vitro P-glycoprotein assays in drug discovery. *J. Pharmacol. Exp. Ther.* **2001**, *299*, 620-628.
19. Rautio, J. *et al.* In vitro p-glycoprotein inhibition assays for assessment of clinical drug interaction potential of new drug candidates: a recommendation for probe substrates. *Drug Metab. Dispos.* **2006**, *34*, 786-792.
20. Keogh, J. P. & Kunta, J. R. Development, validation and utility of an in vitro technique for assessment of potential clinical drug-drug interactions involving P-glycoprotein. *Eur. J. Pharm. Sci.* **2006**, *27*, 543-554.
21. Szeremy, P. *et al.* Comparison of 3 assay systems using a common probe substrate, calcein AM, for studying P-gp using a selected set of compounds. *J. Biomol. Screen.* **2011**, *16*, 112-119.
22. Nederman, T. Effects of vinblastine and 5-fluorouracil on human glioma and thyroid cancer cell monolayers and spheroids. *Cancer Res.* **1984**, *44*, 254-258.
23. Nederman, T. & Carlsson, J. Penetration and binding of vinblastine and 5-fluorouracil in cellular spheroids. *Cancer Chemother. Pharmacol.* **1984**, *13*, 131-135.
24. Risberg, B., Grontoft, O. & Westholm, B. Origin of carcinoma in secretory endometrium--a study using a whole-organ sectioning technique. *Gynecol. Oncol.* **1983**, *15*, 32-41.
25. Hwang, C. W., Wu, D. & Edelman, E. R. Physiological transport forces govern drug distribution for stent-based delivery. *Circulation* ***2001***, *104*, 600-605.
26. Youssef, J., Nurse, A. K., Freund, L. B. & Morgan, J. R. Quantification of the forces driving self-assembly of three-dimensional microtissues. *Proc. Natl. Acad. Sci. U S A* **2011**, *108*, 6993-6998.
27. Napolitano, A.P., Chai, P., Dean, D.M., Morgan, J.R. Dynamics of the Self-Assembly of Complex Cellular Aggregates on Micro-Molded Non-Adhesive Hydrogels. *Tissue Eng.* ***2007***, *13*, 2087-2094.
28. Nishi, Y. *et al.* Establishment and characterization of a steroidogenic human granulosa-like tumor cell line, KGN, that expresses functional follicle-stimulating hormone receptor. *Endocrinology* **2001**, *142*, 437-445.

29. Ford, J. M, Bruggemann, E.P., Pastan, I., Gottesman, M.M. and Hait, W. N. Cellular and biochemical characterization of thioxanthenes for reversal of multidrug resistance in human and murine cell lines. *Cancer Res*. **1990**, *50*, 1748-1756.

30. Robey,R. W., Lin, B., Qiu, J., Chan, L.L.Y, Bates, S.E. Rapid detection of ABC transporter interaction: Potential utility in pharmacology. *J. of Pharm. & Tox. Methods* **2011**, *63*, 217-222.

31. Hanna, E.A., *et al* Gap junctional intercellular comunication and connexin-43 expression in human ovarian surface epithelial cells and ovarian carcinoms *in vivo* and *in vitro*. *Carcinogenesis* **1999**, *20*, 1369-1373

32. Davidson, J.S., Baumgarten, I. M., Harley, E.H. Reverisible inhibition of intercellular junctional communication by glycyrrhetinic acid. *Biochem. Biophys. Res. Com.* **1986**, *134*, 29-36.

33. Gregor, T., Bialek, W., de Ruyter van Steveninck, R. R., Tank, D. W. & Wieschaus, E. F. Diffusion and scaling during early embryonic pattern formation. *Proc. Natl. Acad. Sci. U S A* **2005**, *102*, 18403-18407.

34. Kirkpatrick, J. P., Brizel, D. M. & Dewhirst, M. W. A mathematical model of tumor oxygen and glucose mass transport and metabolism with complex reaction kinetics. *Radia.t Res.* **2003**, *159*, 336-344.

35. Abbaci, M., Barberi-Heyob, M., Blondel, W., Guillemin, F., Didelon, J. Advantages and limitations of commonly used methods to assay the molecular permeability of gap junctional intercellular communication. *Biotechniques* **2008**, *45*, 33-61.

36. Bao, B., Jiang, J. Yanase, T., Nishi, Y., and Morgan, J.R. Connexon-mediated Cell Adhesion Drives Microtissue Self-assembly **2011**, *FASEB J*. 25: 255-264.

37. Lee, K. S. & Tsien, R. W. Mechanism of calcium channel blockade by verapamil, D600, diltiazem and nitrendipine in single dialysed heart cells. *Nature* **1983**, *302*, 790-794.

38. Ferry, D. R., Traunecker, H. & Kerr, D. J. Clinical trials of P-glycoprotein reversal in solid tumours. *Eur. J. Cancer* **1996**, *32A*, 1070-1081.

39. Tolcher, A. W. *et al.* Phase I crossover study of paclitaxel with r-verapamil in patients with metastatic breast cancer. *J. Clin. Oncol. **1996**, 14*, 1173-1184.

40. Bao, B., Jiang, J., Yanase, T., Nishi, Y. & Morgan, J. R. Connexon-mediated cell adhesion drives microtissue self-assembly. *FASEB J. **2011**, 25*, 255-264.

41. Chan, H. S. *et al.* Combining cyclosporin with chemotherapy controls intraocular retinoblastoma without requiring radiation. *Clin. Cancer Res.* **1996**, *2*, 1499-1508.

42. Fracasso, P. M. *et al.* Phase II study of paclitaxel and valspodar (PSC 833) in refractory ovarian carcinoma: a gynecologic oncology group study. *J. Clin. Oncol.* **2001,** *19*, 2975-2982.

43. Desroches, B.R., Zhang, P., Choi, B., Maldonado, A.E., Rago, A., Liu, G.X. Nath, N., King, M.E., Hartmann, K.M., Yang, B., Koren, G., Morgan, J.R. and Mende U. Functional Scaffold-free Cardiac Microtissues: A Novel Model for the Investigation of Heart Cells. *Am J Physiol*. *Heart Circ. Physiol.* **2012**, *302*: H22031-H220442.

44. Achilli, T. M., McCalla, S., Tripathi, A. & Morgan, J. R. Quantification of the kinetics and extent of self-sorting in three dimensional spheroids. *Tissue Eng. Part C Methods* **2012**, *18*, 302-309.

3.10 Figures

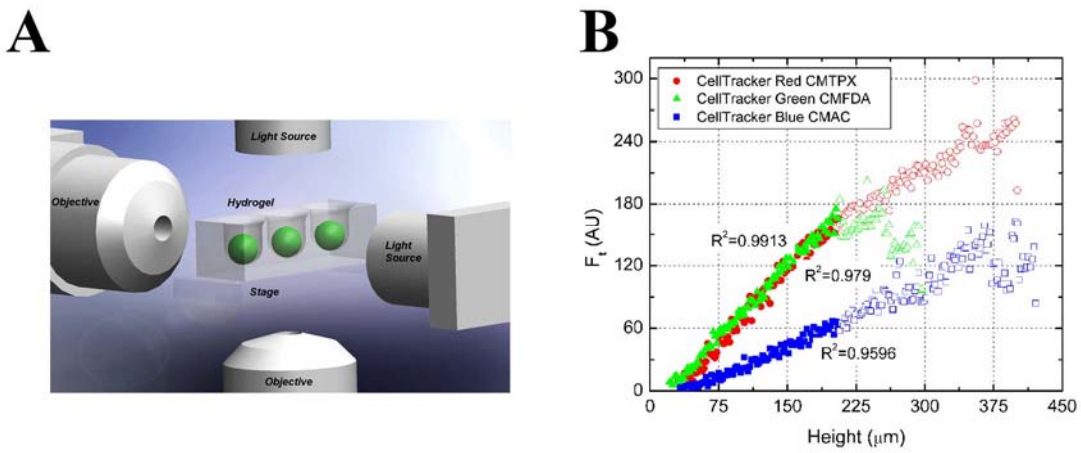

Figure 3-1. Experimental set-up to form spheroids and capture wide-field fluorescent images. Standard view (*x*, *y*) and side view (*z*) microscopy were used to obtain fluorescent images of spheroids self-assembled in a micro-molded nonadhesive hydrogel (A). Uniformly labeled spheroids of varying sizes were formed from cells stained with CellTracker™ green, red, or blue dyes, and fluorescent images were taken 24 hours after self-assembly. The height (*z* dimension) of spheroids of varying sizes that were uniformly labeled red (●), green (▲), or blue (■) were measured and plotted versus peak spheroid fluorescence at the position of maximum fluorescence, maximum cell density (spheroid center) (F_t (AU))(B). Up to a critical height of 205 μm, there is a linear relationship between spheroid height and total fluorescence.

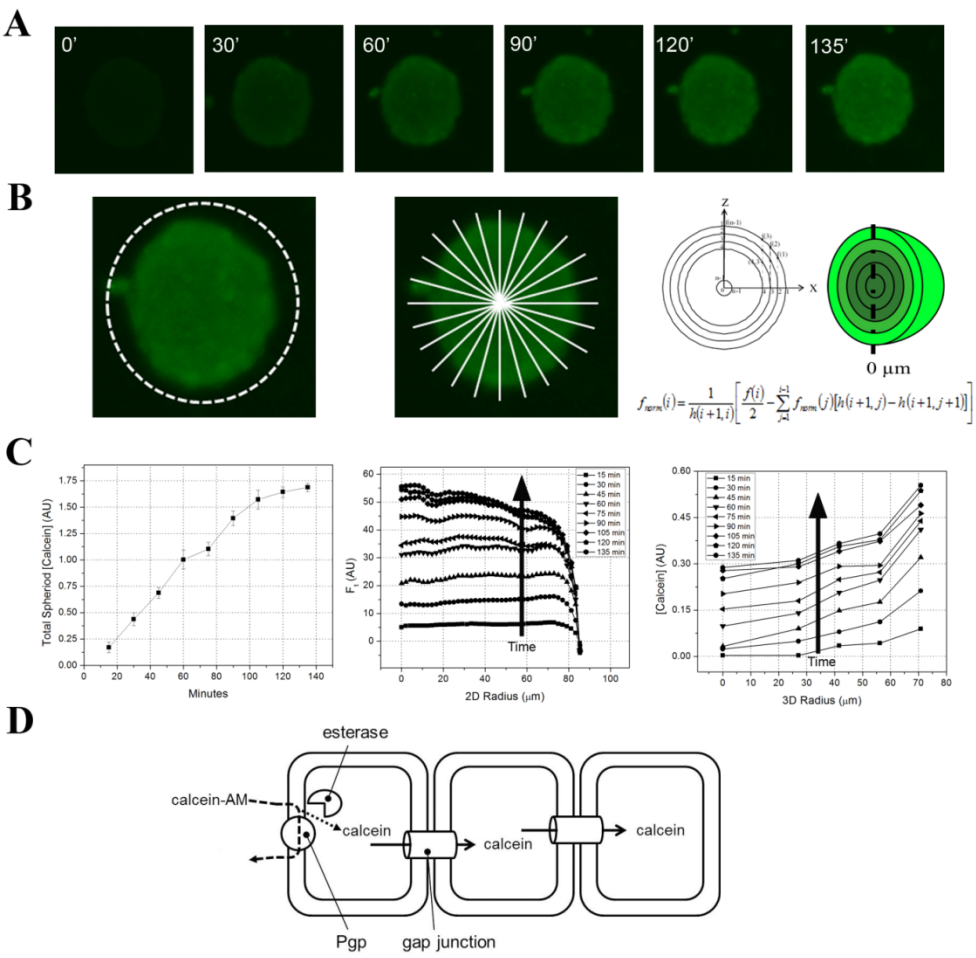

Figure 3-1. Quantification of uptake and diffusion of fluorescent calcein in multi-cellular spheroids. Spheroids of KGN cells were incubated with 1 µM calcein-AM and time-lapse fluorescent images taken over 135 minutes (A). The total spheroid calcein, the 2D radial distribution of calcein and the 3D radial distribution of calcein were calculated from the images (B, C). Schematic showing multiple cell layers of a spheroid connected by GJIC (D). Calcein-AM surrounding the spheroid is actively effluxed by Pgp, but some gains access to the cytoplasm where it is converted by esterases into fluorescent calcein that is trapped within the cell. Calcein can diffuse inward toward the spheroid core via GJIC connecting multiple cell layers.

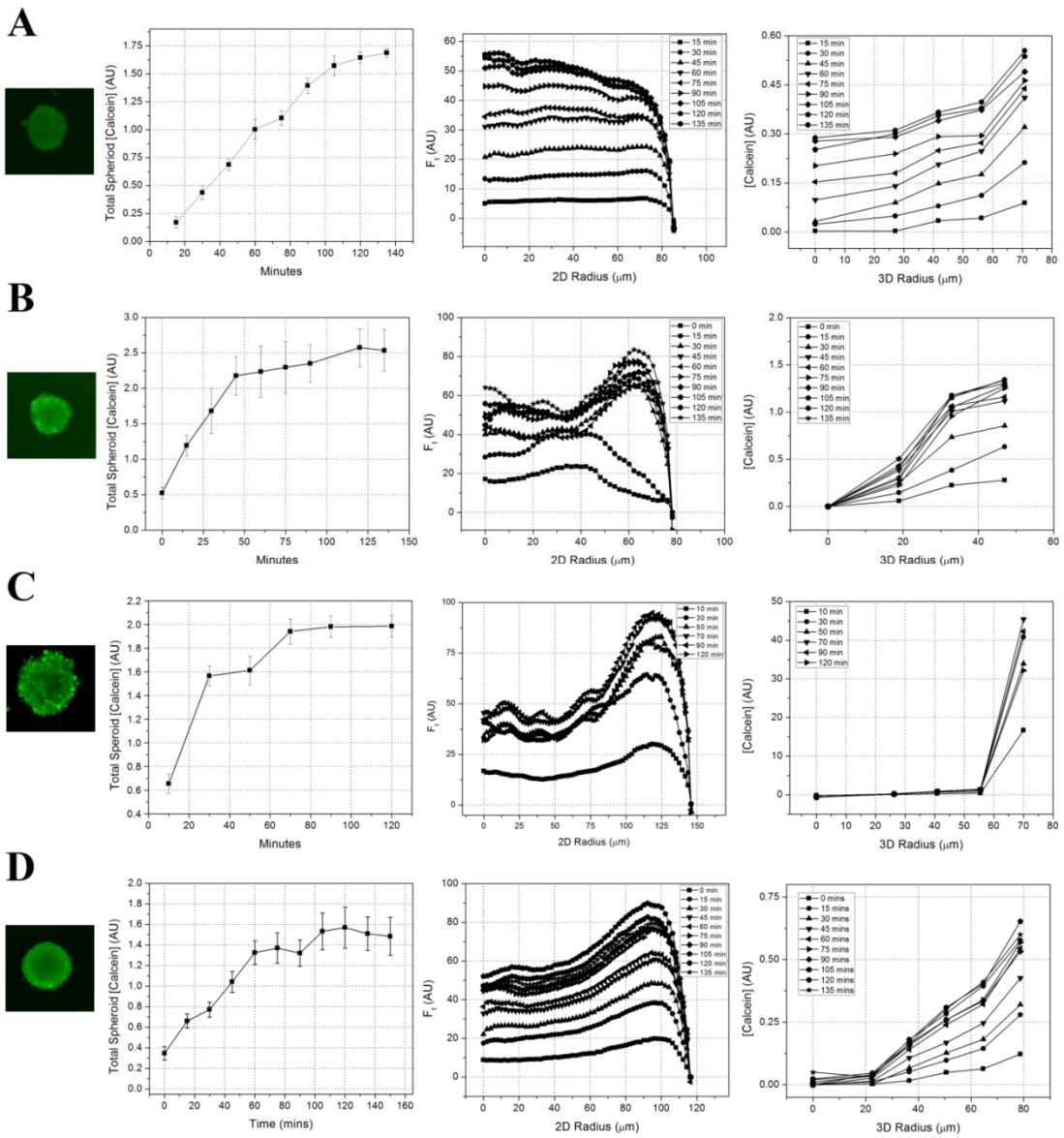

Figure 3-3. Uptake and diffusion of fluorescent calcein in multi-cellular spheroids. Spheroids of KGN (A), MCF-7 (B), OVCAR-3 (C) and HEK (D) cells were incubated with 1 μM calcein-AM and time-lapse fluorescent images taken over 135 minutes. Total calcein fluorescence in the entire spheroid was quantified over time (n = 15-26). Regardless of cell type used to form the spheroids, total spheroid calcein accumulated rapidly over time and started to plateau after about 40- 60 minutes. The 2D radial distribution of calcein within these spheroids at each time point was quantified and the resulting 3D radial distribution of calcein within these spheroids at each time point was also calculated. The 2D and 3D radial profiles were significantly different depending on cell type. KGN, MCF-7 and HEK spheroids showed the greatest diffusion of calcein into the core, whereas OVCAR-3 spheroids lacking GJIC showed little if any diffusion of calcein into the core with most of the calcein confined to the outer layer of cells.

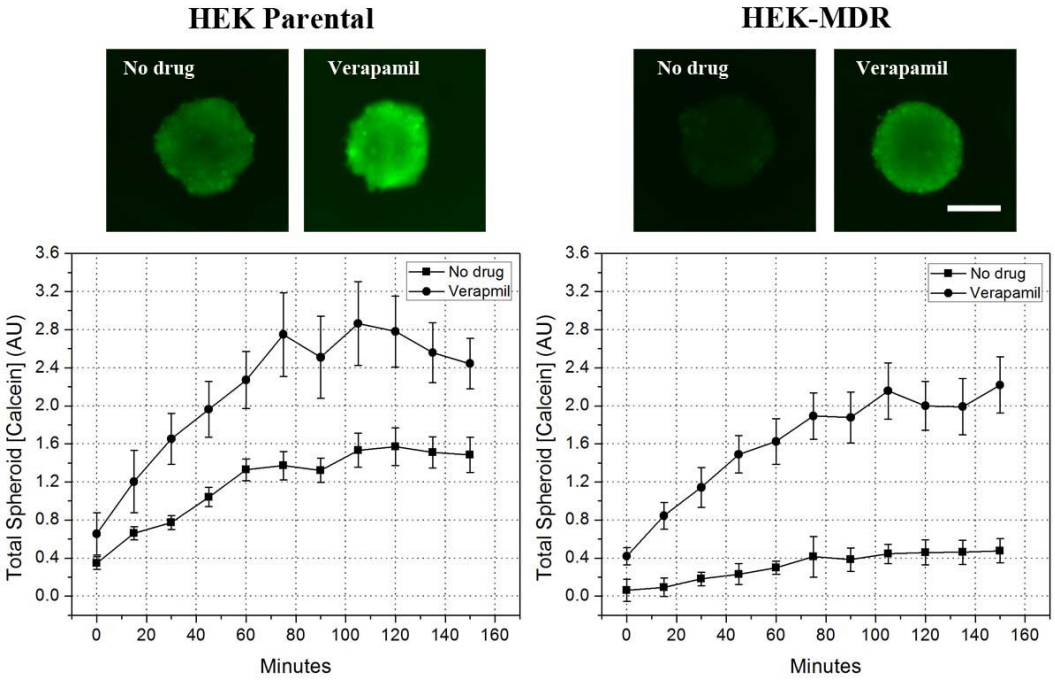

Figure 3-4. Efflux pump overexpression inhibits calcein uptake. Spheroids of HEK cells or HEK-MDR cells transfected to over express Pgp were incubated with 1 µM calcein-AM and time-lapse fluorescent images taken over 135 minutes. Images at 135 minutes. Scale bar 100µm. Total calcein fluorescence in the entire spheroid was quantified over time (n = 18). The rate of increase in total spheroid calcein was significantly lower in spheroids of HEK-MDR cells versus HEK spheroids. In the presence of verapamil (25µM), an inhibitor of Pgp, total spheroid calcein fluorescence increased in untransfected cells that have some endogenous Pgp and increased significantly in HEK-MDR cells over expressing Pgp.

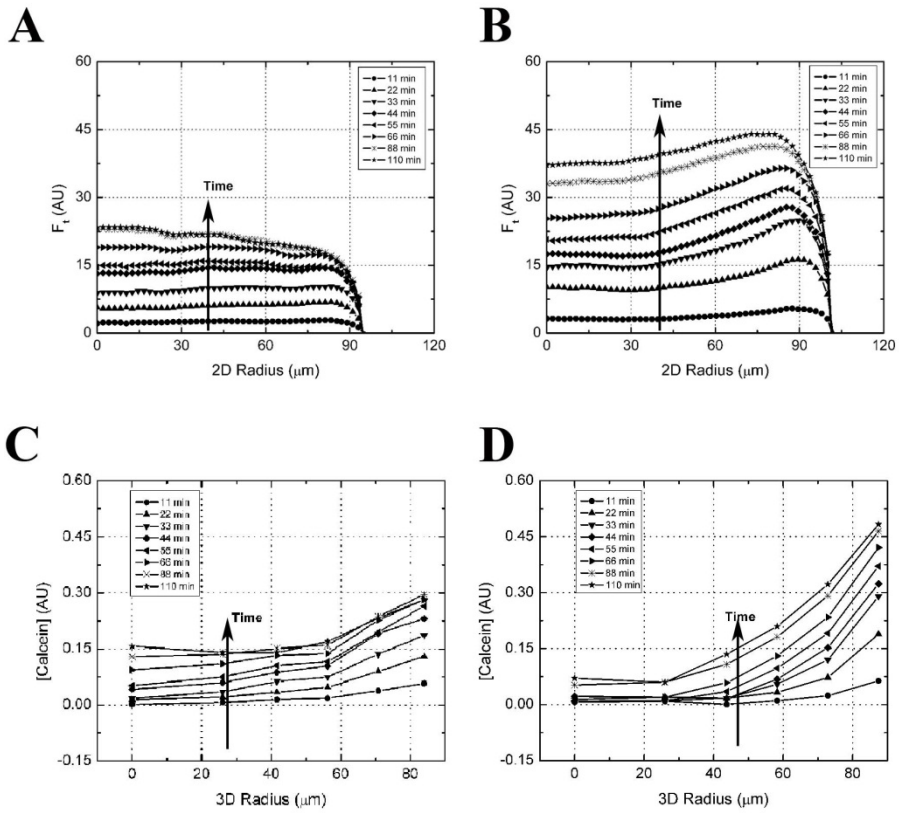

Table 1

	control		verapamil 25μm		loperamide 5μm		cyclosporin A 25μm	
	[Calcein]	%	[Calcein]	%	[Calcein]	%	[Calcein]	%
outer shell	0.40 ±0.05	26 ±2	1.12 ±0.14*	37 ±4*	0.98 ±0.16*	40 ±4*	1.33 ±0.21 *	32 ±5
inner core	0.19 ±0.05	13 ±2	0.11 ±0.03*	3 ±1*	0.1 ±0.4*	4 ±2*	0.72 ±0.16 *	17 ±4
Total	1.72 ±0.09		3.13 ±0.23*		2.41 ±0.18*		3.22 ±0.19*	

Figure 3-5. Verapamil increases total spheroid calcein, but decreases diffusion of calcein. KGN spheroids were incubated with 1 μM calcein-AM in the presence of verapamil (untreated, A, C), (25 μM, B, D), and images were taken every 11 minutes for 110 minutes. A time series of 2D radial profiles (A, B) shows that total fluorescence of all spheroids (F_t (AU)) increase with time. Verapamil treatment increases total spheroid fluorescence over untreated controls, but fluorescence is preferentially located in the outermost layer of cells. The quantitative 3D radial profiles of calcein concentration ([Calcein] (AU))(C, D) reveal that although verapamil increases uptake in the outer layer over control (every time point), calcein concentration at the center of the spheroid does not increase.

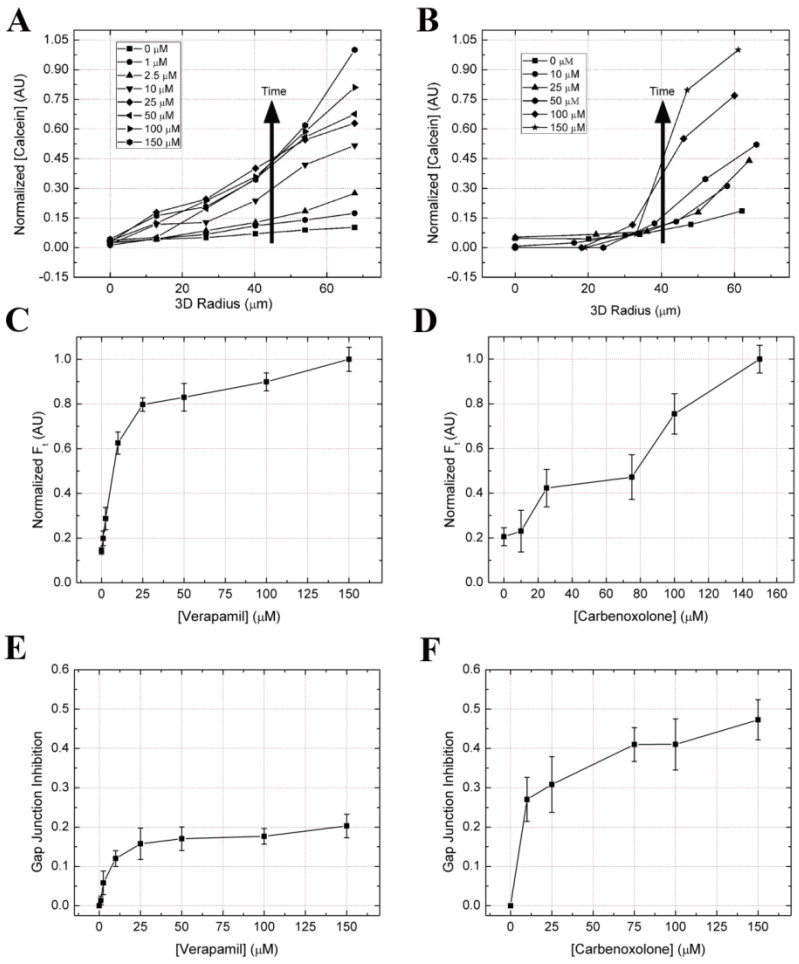

Figure 3-6. Dose responses of verapamil and CBX inhibition of Pgp and GJIC. KGN spheroids were incubated with1 μM calcein-AM in the presence of varying doses of verapamil (A, C, E) or CBX (B, D, F) and fluorescent images obtained after 75 minutes. The 3D radial profiles of drug treated spheroids (A, B) revealed that increasing concentrations of verapamil and CBX both resulted in increased calcein uptake, but that calcein was more localized to the outer shell with CBX treatment. To determine dose response with respect to inhibition of Pgp (C, D) total calcein uptake by spheroids (n=15) as a function of drug concentration is plotted. To aid comparison, data is normalized to the highest point. For verapamil, half-maximal response was 8.5μM, whereas for CBX half-maximal response was 81μM. To determine the dose response for GJIC inhibition (E, F), the drug's ability to increase the fraction of calcein compartmentalized to the outer shell was calculated. If the fraction of calcein was the same as the untreated control this was zero percent inhibition. If all calcein was confined to the outer shell this was 100% inhibition. For verapamil, half-maximal response was 8.6μM similar to the concentration that elicited half-maximal inhibition of Pgp. For CBX, half-maximal response for inhibition of GJIC was 9.4μM, significantly lower than the concentration that elicited half-maximal inhibition of Pgp. When comparing the maximal responses, CBX inhibited GJIC to a greater extent than verapamil.

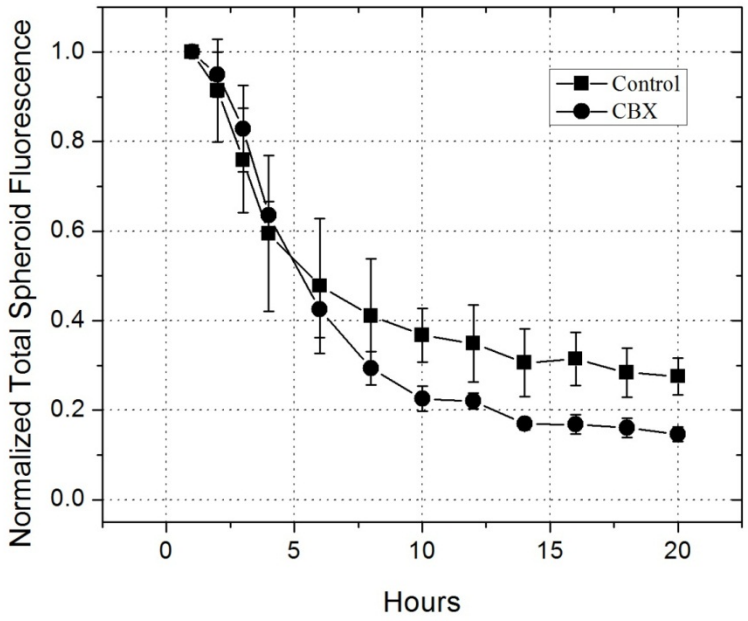

Figure 3-7. CBX does not increase total spheroid calcein by slowing calcein loss. KGN spheroids with and without CBX treatment were incubated with 1 µM calcein-AM for 135 minutes. Calcein-AM was then removed and replaced with drug-free medium. Images were taken once per hour for 20 hours to determine the rate of calcein loss and data normalized to the initial fluorescence. Loss from the entire spheroid was measured by the total spheroid fluorescence and decreased at the same initial rate for control and CBX treated spheroids.

Chapter 4

4. Quantification of Tissue Elimination from 3D Multi-Layer Spheroids

Toni-Marie Achilli and Jeffrey R. Morgan

The following chapter is in preparation to be submitted to Drug Metabolism and Disposition.

4.1 Abstract

Although several *in vitro* models exist to test new drug candidate for unwanted drug-transporter mediated interactions that affect ADME-Tox, there is a need to develop new models that can better replicate the complexity of the *in vivo* environment. In terms of tissue elimination, efflux transporters such as P-glycoprotein (Pgp) play a critical role. Here, we report the use of three-dimensional (3D) multi-layer spheroids to quantitatively study the elimination of fluorescent rhodamine 123 (rh123), a Pgp substrate, directly from these microtissues. When preloaded with rh123 spheroids from human embryonic kidney (HEK) cells eliminate the dye over time. Elimination was increased by spheroids overexpressing Pgp and was decreased when spheroids were treated with a known Pgp inhibitor, verapamil. Chimeric spheroids consisting of both high (HEK-MDR) and low (HEK-PC) cells were used as a controlled model to study the effect of increasing levels of Pgp on the elimination and half-life ($t_{1/2}$) of rh123 elimination. This method is amenable to many different cell types, containing any transporter, to study interactions of transporter substrates, and inhibitors. This assay has the potential to serve as a more predictive model for drug ADME-Tox evaluation, drug-drug or drug-transporter interactions, and multi-drug resistance

4.2 Introduction

It is well understood that the efficacy of a drug depends on its ability to reach its target at the desired concentration[1]. And, drug concentration within a tissue is limited not only by the ability of the drug to enter and transport through the tissue, but also by how fast it is eliminated from the tissue[2]. Drug efflux transporters, in particular P-glycoprotein (Pgp) of the ATP-Binding Cassette transporters are highly expressed in tissues critical for drug ADME-TOX, and act as a barrier to uptake and penetration while also acting to increase the rate of elimination. Pgp is highly expressed in the epithelia of the intestine, liver, and kidney, and also endothelium of the blood-brain barrier[3, 4]. This expression impacts the pharmacological behavior of all drugs by limiting uptake and penetration into tissues and effecting the oral bioavailability, intestinal absorption, hepatobilliary and urinary excretion[5-8]. The disposition of a large number of drugs is modulated by Pgp and efflux transporters since their substrates include a broad range of chemically diverse substrates used for a variety of therapeutic applications[9]. Since the ADME-TOX is crucial to the clinical success of a drug, early in vitro screening in drug discovery is needed to select against drugs that negatively affect ADME-TOX, or that can predict the potential of clinically significant drug-transporter and drug-drug interaction yet still prove effective.

The pharmacological importance of Pgp and ABC-transporters has resulted in the development of several in vitro assays used in drug development that tests for drug-transporter and drug-drug interactions[10, 11]. These assays are either membrane based biochemical assays or cell based assays, in which target drugs are tested to determine if they are either a substrate or an inhibitor of efflux pumps[8, 9, 12, 13]. Cell based assays

primarily use polarized genetically modified cell lines, in a monolayer, to measure the vectorial transport across a semi-permeable membrane, but they are often unable to replicate the transport processes of an intact tissue or organ[12, 14-16]. Primary cells from the isolation of tissues and organs are also explored as they express the full complement of transporters at physiologically relevant levels. The most complex of these techniques is the sandwich culture of hepatocytes which replicate efflux from these cells into the bile canaliculi, and have shown to predict a good correlation between in vitro and in vivo biliary clearance[17, 18]. To determine tissue elimination, or clearance, measurements are made from blood plasma or urinary concentration. From these values pharmacokinetic models are then used to calculate elimination values from individual organs. Rarely is elimination measured directly from the organ or tissue, only monolayers of cells or suspensions of cells are used. It is recognized the 2D cell culture does not replicate the complexities of the 3D in vivo environment.

In this paper, we have developed a new 3D multi-layer spheroid model to quantitatively study drug elimination out of tissues using rhodamine 123 along with wide-field time lapse fluorescent images. We have calculated important pharmacokinetic parameters such as elimination rate and half-life out of spheroids containing various levels of efflux transporters. We have shown that elimination rate is directly related to the expression level of the efflux pump, P-glycoprotein.

4.3 Materials and Methods

Cell Culture, Micro-molds and Spheroid Formation

Human Embryonic Kidney (HEK) cells (passages 2-12) were grown in EMEM (Corning, Corning, NY) supplemented with 10% fetal bovine serum (ThermoFisher Scientific, Waltham, MA) and 1% penicillin/streptomycin (Sigma-Aldrich, St. Louis, MO) at 37^0C with a 5% CO_2 atmosphere. HEK parental cells and HEK cells transfected to overexpress MDR1 (P-glycoprotein) and MRP19 (MRP) were maintained by culturing cells in 2 mg/mL of G418 (sigma) throughout the duration of the experiment (ref papers as source of cells).

Micro-molded agarose gels were used to form spheroids (Napolitano). A sterile 2% agarose (UltraPure™, Invitrogen, Carlsbad, CA) 0.9% saline solution was cast into micro-molds (MicroTissues, Inc., Providence, RI) that had been autoclave sterilized. After 5 minutes when the agarose had set, the micro-molded agarose gels were released from the molds and transferred to 24-well tissue culture plates. The micro-molded agarose gels were locked in place via the addition of a drop of molten agarose and equilibrated in culture medium overnight. A single micro-molded gel for forming spheroids had 96 round-bottomed recesses (400 μm diameter, 800 μm depth)in a 12x8 array.

To form spheroids, cells were trypsinized, counted, resuspended and 50 μL of the cell suspension (7×10^4 cells) was pipetted into the seeding chamber of each micro-molded gel. Cells were allowed to settle for 30 minutes; then 2 mL of serum-free medium was added to each of the wells. Cells used to analyze the sorting of mixed cell populations were prestained by incubation in EMEM with 5 μM CellTracker Red

CMPTX or Cell Tracker Green CMFDA (Invitrogen) for 50 minutes prior to trypsinization.

Loading and Elimination of Rhodamine 123

To measure the elimination of rhodamine 123 (rh123)(Sigma), spheroids were first loaded with the fluorescent dye. For loading, spheroids were harvested from the micro-molded gels after 24 hours of self-assembly, via gentle pipetting and transferred to a 24-well plate. Spheroids were incubated with EMEM containing the various concentrations of rhodamine 123 (1-4 μM) while gently shaking for 2 hours. Medium containing rh123 was removed, and spheroids were washed with phosphate buffered saline (PBS), harvested and seeded into new micro-molded gels that had been equilibrated with culture medium without rh123. Time-lapse fluorescent images were acquired every 15 or 30 minutes for 6-15 hours at 37^0C and 5% CO_2 atmosphere.

To inhibit MDR1 during loading of rh123, spheroids were treated with verapamil (100 μM) in EMEM during the 2 hour loading period. To inhibit MDR1 during the elimination phase, micro-molded gels were equilibrated with verapamil (100 μM) in EMEM overnight. Rh123 loaded spheroids were then seeded into these verapamil equilibrated gels and were further incubated in freshly prepared verapamil-containing medium during the measurements of rh123 elimination.

Microscopy and Image Analysis

For standard, *x-y* view images, a Carl Zeiss Axio Observer Z1 equipped with an AxioCam MRm camera (Carl Zeiss MicroImaging, Thornwood, NY), an Xcite 120 XL

mercury lamp (Exfo Life Sciences Division, Mississauga, Ontario), and an incubation chamber (37ºC, 5% CO_2) was used to obtain brightfield, phase contrast, and epi-fluorescent images. Quantitative image analysis was performed using a custom ImageJ (NIH) program. Briefly, spheroid perimeter was traced using the active contour function, EZSnake, and the total fluorescent intensity was quantified within the spheroid. A background of identical area was obtained from an adjacent area of the image and subtracted from the spheroid's total fluorescent intensity. To obtain % maximum fluorescence, the fluorescent intensity at each time point was normalized to the total fluorescent intensity at the initial time point.

To determine the time to eliminate 50% of the initial fluorescence ($t_{1/2}$), we linearized our data by taking the LN of the % maximum fluorescence over the first 6 time points of our experiment. From this, we determined the elimination rate constant (K_e) using the formula:

$$\boldsymbol{t_{1/2} = \frac{ln2}{K_e}}$$

Statistical Analysis

Two experimental groups were tested for significant variability between sample means using analysis of variance (ANOVA). If significant differences were established, we performed a Bonferroni *t*-test to determine significance.

4.4 Results

Quantification of Tissue Elimination by Spheroids

To measure tissue elimination, we devised an assay based on multi-cellular spheroids and fluorescent rhodamine 123 (rh123). Spheroids of HEK-PC cells were formed by seeding cells into micro-molded agarose gels. Twenty four hours later, spheroids were harvested by gentle pipetting of the seeding chamber and inversion of the gel. Spheroids were then incubated in rh123 (1μM) for 2 hours. The spheroids were removed from rh123, quickly washed, and seeded into new agarose gels where they were imaged every 15 minutes for 6 hours (**Figure 4-1**). Rh123 fluorescence in the entire spheroid declined over time, eliminating 80% of the initial loaded rh123 after 5 hours, with a $t_{1/2}$= 2.1 ± 0.3 hours for HEK-PC spheroids. As a comparison, a spheroid (r=100 μm) occupies a volume of $4x10^6$ μm^3. In the absence of the barriers created by these multi-cellular spheroids, rh123 would diffuse out of this volume (diffusivity in water =4.6 x 10^6 cm^2/s) within t= 25 seconds. Thus, the spheroid is a complex barrier to rh123 elimination.

To determine the distribution of rh123 throughout the 3D spheroid, we used our previously reported MATLAB algorithm that uses an iterative mathematical formula to deconvolve the total fluorescent signal by estimating the spheroid as a series of concentric spheres (shells) 14 μm in width (Achilli, et al). It then calculates the relative fluorescence in each of these compartments. This analysis showed that the spheroids were homogenously loaded with rh123 at the start of the elimination experiment (30 minutes after spheroid seeding). Moreover, when using this analysis to determine the rate of elimination from the inner core of the spheroid versus its outer shell, we found no

significant differences. Further, the elimination rates from the core and shell were the same as the rate from the entire spheroid.

Efflux Pump Expression Increases the Rate of rh123 Elimination

To determine the effects of MDR on elimination, we tested spheroids formed from cells over expressing MDR (HEK-MDR) and compared them to control spheroids made from untransfected cells (HEK-PC) or cells over expressing MRP (HEK-MRP). As before, spheroids were loaded by incubation with rh123 (1 μM) and fluorescence of the entire spheroid was measured over time (**Figure 4-2**). For spheroids of HEK-PC cells and HEK-MRP cells, the rates of rh123 elimination were comparable, $t_{1/2}$= 2.5 ± 3 and $t_{1/2}$= 2.5 ± 0.4, respectively. However, when subjected to the same protocol, loading of HEK-MDR spheroids with rh123 was undetectable.

To load HEK-MDR spheroids, we added verapamil (100 μM), an MDR inhibitor during the 2-hour incubation period with rh123. Verapamil was removed prior to measuring elimination. For comparison, HEK-PC and HEK-MRP spheroids were also loaded with rh123 in the presence of verapamil. HEK-MDR spheroids were successfully loaded with rh123 and their rate of elimination was significantly faster ($t_{1/2}$= 0.4 ± 0.2 hours) than both HEK-PC spheroids ($t_{1/2}$= 2.3 ± 0.4) and HEK-MRP spheroids ($t_{1/2}$=2.5 ± 0.3) which were indistinguishable. Thus, rh123 elimination is pump dependent.

To further refine verapamil's action in our assay, we incubated spheroids with verapamil (100 μM) during different phases of the rh123 elimination experiment. We measured the rate of elimination of spheroids that had been treated with verapamil during loading only; during loading and elimination; and during elimination only and compared

these rates to controls that were not exposed to verapamil (**Figure 4-3**). For all conditions, the rate of rh123 elimination by HEK-PC and HEK-MRP spheroids were the same. With no verapamil treatment or verapamil present only during loading, the rate of elimination was equal, $t_{1/2}$=1.7± 0.5 hours. Likewise, the rate of elimination was equal for HEK-PC and HEK-MRP spheroids spheroids when verapamil was present during elimination only or during loading and elimination, $t_{1/2}$= 19.1 ± 0.5. Compared to samples without verapamil, verapamil treatment did reduce the rate of elimination presumably through its action on baseline endogenous levels of MDR expressed by HEK-PC and HEK-MRP cells.

The importance of the timing of verapamil treatment was evident in the HEK-MDR spheroids. First, it was not possible to load HEK-MDR spheroids with rh123 unless it was present during loading. Second, when verapamil was present during elimination, the rate was significantly decreased versus when it was absent ($t_{1/2}$=2.8 ± 0.2 hours versus $t_{1/2}$=0.4 ± 0.2 hours).

Dependence of Elimination on rh123 Concentration

To determine if rh123 elimination was concentration dependent, we incubated HEK-PC, HEK-MRP, and HEK-MDR spheroids with increasing concentrations of rh123 (1, 2, 3, and 4 μM) for varying times (**Figure 4-4**). Measurement of the initial fluorescence in the spheroids showed that rh123 loading increased with increasing concentration of rh123 as well as increasing time of incubation. Under these conditions, we did not reach saturation. Next, we measured the elimination rates of these spheroids. As expected, the rate of elimination by HEK-MDR spheroids was significantly faster

compared to HEK-PC spheroids and, HEK-MRP. However, for all three types of spheroids elimination was unaffected by initial rh123 concentration.

To analyze the elimination kinetics of spheroids containing varying amounts of MDR, we formed mixed spheroids of comparable size, but containing varying ratios of HEK-PC cells and HEK-MDR cells. To determine if the cells self-sorted when mixed, HEK-PC cells were labeled with CellTracker green and HEK-MDR cells were labeled with CellTracker red, mixed (0%, 10%, 25%, 50%, 75%, 90%, and 100% MDR cells) and then seeded into micro-molded gels. Twenty four hours later, fluorescent images were obtained of the self-assembled spheroids. Unlike other pairs of cell types that self-sort to form a clear core and outer shell, HEK-PC cells and HEK-MDR were interspersed, but the HEK-PC cells did have a tendency to form small clusters, especially in spheroids with greater than 50% HEK-MDR cells.

To measure elimination, mixed spheroids were loaded with rh123 (1 μM), in the presence of verapamil (100 μM) to attain comparable initial loading and then transferred to drug free gels where time lapse fluorescent images were obtained. Images at 105 minutes (a time when all spheroids passed their $t_{1/2}$) showed decreasing total spheroid fluorescence as the proportion of HEK-MDR cells increased. It was also evident at this time point that some spheroids were no longer uniformly fluorescent. Fluorescence in spheroids containing less than 50% MDR cells was fairly homogenous, whereas fluorescence in spheroids with greater than 50% MDR cells had clusters of highly fluorescent cells and areas devoid of detectable fluorescence. These clusters of fluorescent cells, or islands of cells, corresponded to the sorting pattern of clusters of HEK-PC cells observed in the labeled mixed spheroids.

The rate of rh123 elimination by these mixed spheroids was measured by quantifying total spheroid fluorescence as a function of time and the $t_{1/2}$ was calculated for each mixture. The plot of half-life as a function of cell mixture showed that the rate of elimination was not a simple mix of the two cell types. The half-lives of the spheroids with 10% and 25% MDR cells were comparable to spheroids with no MDR cells. It was only after the mixture had 50% MDR cells and higher, that the rate of elimination was significantly increased and half-life decreased versus spheroids with no MDR cells.

4.5 Discussion

Increasing recognition of the role of transporters to the absorption, distribution, and elimination of many drugs, as well as their contribution to multi-drug resistance in cancer, has led to the development of several *in vitro* assays used to predict the effect of new drugs and to find new inhibitors of these pumps[4-6]. Additionally, the importance of identifying potential drug-drug interactions that change drug disposition, efficacy, or can lead to toxicity has led to regulatory agencies expecting new drug candidates to have been investigated to predict the risk of transporter-mediated DDIs. The current *in vitro* methods have been primarily membrane or 2D cell-based assays. With their expanding importance, it is critical to develop new, more predictive *in vitro* assays that can be used early in the drug discovery process.

In this paper we have developed a 3D model to quantify the elimination of fluorescent rhodamine 123 out of spheroid microtissues. Our 3D cell culture system allows us to create 100s of spheroids with uniform size and geometry on the same optical plane making them amenable to high throughput fluorescent time lapse microscopy, from which kinetic data can be calculated. Additionally, the microtissues are in culture medium which allows for uniform elimination out of the spheroid surface area. Here, we used human embryonic kidney (HEK) cells to make spheroids which allowed us to characterize our system with a well-known Pgp efflux pump substrate. We measured total rh123 fluorescence in the entire spheroid as it was eliminated from preloaded microtissues over time. This assays allowed us to calculate kinetic values such as the elimination rate and time to eliminate 50% of the rh123 ($t_{1/2}$). We calculated that the HEK spheroids had a $t_{1/2}$ = 2.13 hours which is significantly longer than the time it would

take for rh123 to freely diffuse out of a volume equal in size to our microtissue and therefore can be used to measure elimination.

Drug elimination can be defined to have both an active and passive component. The active component would be controlled primarily by active efflux transporters while the passive component would be a combination of diffusion, lipid solubility and permeability. We used HEK parental control microtissues which have a level of endogenous efflux pump expression. When we treat these cells with pump inhibitors, namely verapamil, we measure a significant decrease in the elimination rate of rh123. At the 100 μM verapamil dose we have reached a steady state in elimination rate which indicates we have sufficiently inhibited all of the endogenous verapamil sensitive pumps. Comparing the total elimination from the HEK-PC microtissues with and without verapamil treatment allows us to calculate both the active, or verapamil sensitive, as well was the passive, or verapamil insensitive transport. Here, we report the verapamil sensitive active elimination from the microtissues is 16X greater than the verapamil insensitive passive component of total elimination rate. To further examine the role of active elimination from tissues we measured the elimination rates from genetically modified Pgp overexpressing microtissues, and their modulation with verapamil. The effect of overexpression of Pgp resulted in a 5.25X increase in active elimination. Furthermore, we were able to quantify the effect of modulating active elimination in these overexpressed tissues, and although we were not able to reach total inhibition at clinically relevant verapamil concentrations we were able to decrease elimination 7.5X, which resulted in elimination rates similar to those observed in the HEK-PC tissues.

It is known that Pgp expression is differentially expressed throughout the body and that the expression within individual tissues is dynamically regulated[1, 3, 4]. Our 3D culture system allows us to make chimeric tissues consisting of mixtures of low and high pump cells, thus varying the expression level of Pgp in a controlled manner. We calculated elimination rates in tissues with increasing percentages of Pgp overexpressing cells, and measured an increase in the total elimination rate. Interestingly, our data showed that to increase total elimination the percentage of high pump expressing cells had to reach a threshold of greater than 25% before a significant change in elimination rate was observed. In mixtures containing less than 25% overexpressed cells the elimination kinetics were identical to control. These chimeric tissues with low and high pump cells interacting as one functional tissue rather than individual cells can only be replicated in the 3D environment. These mixed tissues are an important step in in vitro drug discovery assays as they can serve as models for different organs that express different levels of pumps, models for a single organ as pump expression changes, and as a tumor model with increasing levels of multi-drug resistance.

This 3D model to calculate elimination from tissues can easily be extended to include different cell types, different cell substrates, and different efflux pumps. As we and others have shown numerous cell types will self-assemble in our molds which would allow us to make microtissues from cells of various organs to measure elimination from. While there is a need for more predictive models of toxicity, drug-transporter, and drug-drug interactions, our model has the potential to predict these interactions and to model the ADME-TOX properties that are critical to a drugs success.

4.6 Conclusion

The quantitative model described is a novel *in vitro* assay that has the potential to be more predictive than current *in vitro* assays in determining pharmacokinetic parameters important to drug ADME-Tox, especially elimination, and drug-drug and drug-transporter interactions. Our 3D tissues can self-assemble into spheroids containing multiple cell types. These chimeric tissues can be engineered as models of increasing multi-drug resistance (high and low pump cells), models for different organs, models for the differential expression of transporters within one organ, or as models of tissues overexpressing multiple transporters.

4.7 Acknowledgements and Disclosures

This work was funded in part by the National Institute of Health (R01EB008664-01A1) and seed funds from the Johnson & Johnson Corporate Office of Science & Technology and the Brown Technology Ventures Office. Authors would also like to thank partial support from National Aeronautics and Space Agency (NASA) and the generous support of Donna McGraw Weiss '89 and Jason Weiss. J.R.M has an equity interest in Microtissues, Inc. This relationship has been reviewed and managed by Brown University in accordance with its conflict of interest policies.

4.8 References

1. Williams JA, Bauman J, Cai H, Conlon K, Hansel S, Hurst S, Sadagopan N, Tugnait M, Zhang L, Sahi J. In Vitro Adme Phenotyping in Drug Discovery: Current Challenges and Future Solutions. *Current opinion in drug discovery & development* **2005**;*8* 78-88.

2. Kuwano M, Toh S, Uchiumi T, Takano H, Kohno K, Wada M. Multidrug Resistance-Associated Protein Subfamily Transporters and Drug Resistance. *Anti-cancer drug design* **1999**;*14* 123-131.

3. Flens MJ, Zaman GJ, van der Valk P, Izquierdo MA, Schroeijers AB, Scheffer GL, van der Groep P, de Haas M, Meijer CJ, Scheper RJ. Tissue Distribution of the Multidrug Resistance Protein. *The American journal of pathology* **1996**;*148* 1237-1247.

4. Szakacs G, Varadi A, Ozvegy-Laczka C, Sarkadi B. The Role of Abc Transporters in Drug Absorption, Distribution, Metabolism, Excretion and Toxicity (Adme-Tox). *Drug discovery today* **2008**;*13* 379-393.

5. Dietrich CG, Geier A, Oude Elferink RP. Abc of Oral Bioavailability: Transporters as Gatekeepers in the Gut. *Gut* **2003**;*52* 1788-1795.

6. Chan LM, Lowes S, Hirst BH. The Abcs of Drug Transport in Intestine and Liver: Efflux Proteins Limiting Drug Absorption and Bioavailability. *European journal of pharmaceutical sciences : official journal of the European Federation for Pharmaceutical Sciences* **2004**;*21* 25-51.

7. Elferink RO, Groen AK. Genetic Defects in Hepatobiliary Transport. *Biochimica et biophysica acta* **2002**;*1586* 129-145.

8. Varma MV, Perumal OP, Panchagnula R. Functional Role of P-Glycoprotein in Limiting Peroral Drug Absorption: Optimizing Drug Delivery. *Current opinion in chemical biology* **2006**;*10* 367-373.

9. Varma MV, Ashokraj Y, Dey CS, Panchagnula R. P-Glycoprotein Inhibitors and Their Screening: A Perspective from Bioavailability Enhancement. *Pharmacological research : the official journal of the Italian Pharmacological Society* **2003**;*48* 347-359.

10. Xia CQ, Milton MN, Gan LS. Evaluation of Drug-Transporter Interactions Using in Vitro and in Vivo Models. *Current drug metabolism* **2007**;*8* 341-363.

11. Li AP. Screening for Human Adme/Tox Drug Properties in Drug Discovery. *Drug discovery today* **2001**;*6* 357-366.

12. Homolya L, Hollo Z, Germann UA, Pastan I, Gottesman MM, Sarkadi B. Fluorescent Cellular Indicators Are Extruded by the Multidrug Resistance Protein. *The Journal of biological chemistry* **1993**;*268* 21493-21496.

13. Deeley RG, Westlake C, Cole SP. Transmembrane Transport of Endo- and Xenobiotics by Mammalian Atp-Binding Cassette Multidrug Resistance Proteins. *Physiological reviews* **2006**;*86* 849-899.

14. Adachi Y, Suzuki H, Sugiyama Y. Comparative Studies on in Vitro Methods for Evaluating in Vivo Function of Mdr1 P-Glycoprotein. *Pharmaceutical research* **2001**;*18* 1660-1668.

15. Yamazaki M, Neway WE, Ohe T, Chen I, Rowe JF, Hochman JH, Chiba M, Lin JH. In Vitro Substrate Identification Studies for P-Glycoprotein-Mediated Transport: Species Difference and Predictability of in Vivo Results. *The Journal of pharmacology and experimental therapeutics* **2001**;*296* 723-735.

16. Rautio J, Humphreys JE, Webster LO, Balakrishnan A, Keogh JP, Kunta JR, Serabjit-Singh CJ, Polli JW. In Vitro P-Glycoprotein Inhibition Assays for Assessment of Clinical Drug Interaction Potential of New Drug Candidates: A Recommendation for Probe Substrates. *Drug metabolism and disposition: the biological fate of chemicals* **2006**;*34* 786-792.

17. Lee CH. Differential Regulation of P-Glycoprotein Genes in Primary Rat Hepatocytes by Collagen Sandwich and Drugs. *Journal of cellular biochemistry* **2002**;*86* 12-20.

18. Lepist EI, Gillies H, Smith W, Hao J, Hubert C, St Claire RL, 3rd, Brouwer KR, Ray AS. Evaluation of the Endothelin Receptor Antagonists Ambrisentan, Bosentan, Macitentan, and Sitaxsentan as Hepatobiliary Transporter Inhibitors and Substrates in Sandwich-Cultured Human Hepatocytes. *PloS one* **2014**;*9* e87548.

4.9 Figures

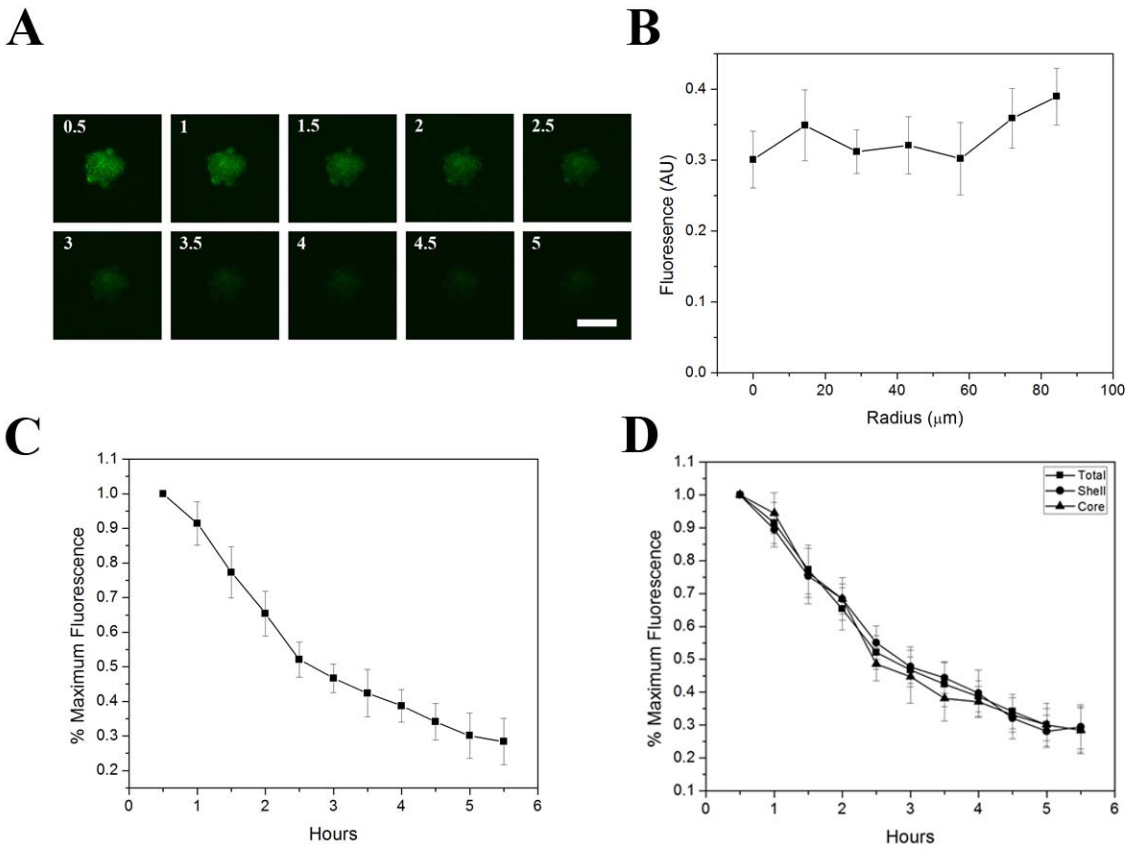

Figure 4-1. **Quantification of the elimination of rh123 in multi-cellular spheroids. Spheroids of HEK-PC cells were incubated for 2 hours with rh123 (1 μM), washed and seeded into micro-molded gels containing fresh medium. Time-lapse fluorescent images were taken over 6 hours (A). The radial distribution of rh123 fluorescence throughout the spheroid was found to be homogenous at the initial time point (t=30 minutes) (B). Rh123 fluorescence of the entire spheroid was quantified from the images to determine the rate of elimination(C). The same images were used in an image analysis program to determine the rate of elimination from the spheroid core versus the outermost shell of the spheroid (D).**

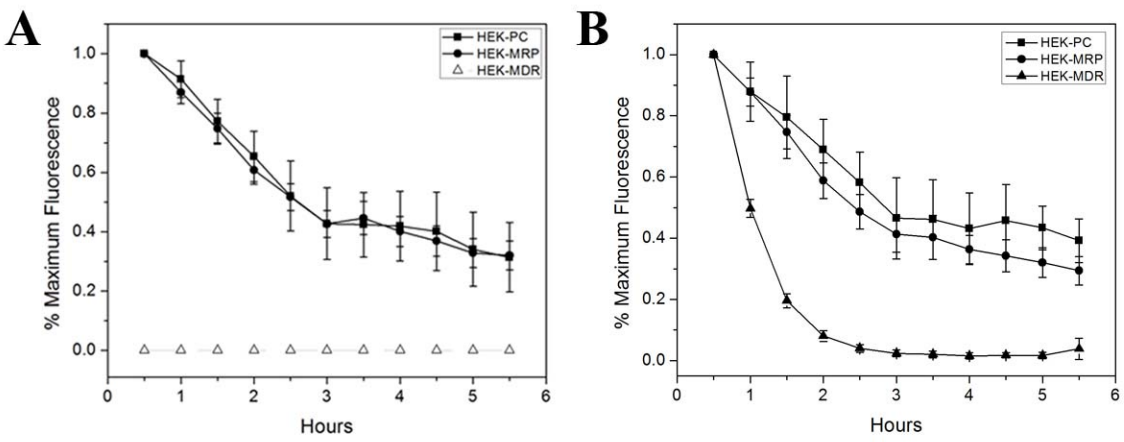

Figure 4-2. Over expression of MDR increases the rate of rh123 elimination. Spheroids of HEK-PC, HEK-MRP, and HEK-MDR cells were incubated with rh123 (1 μM), washed, seeded into micro-molded gels containing fresh medium and fluorescent images taken over 6 hours. Rh123 fluorescence in the entire spheroid was measured at each time point. Under these loading conditions, fluorescence was not detectable for HEK-MDR spheroids, whereas HEK-PC and HEK-MRP spheroids were loaded with rh123 and their rates of elimination were comparable (A). To facilitate loading, verapamil (100 μM) was added to all spheroids during the 2 hour incubation with rh123. HEK-MDR spheroids were successfully loaded and elimination was measured for all spheroids. HEK-MDR spheroids eliminated rh123 at a much faster rate than HEK-PC or HEK-MRP spheroids, with a $t_{1/2}$= 0.4 ± 0.2 hours compared to a $t_{1/2}$= 2.3 ± 0.4 and $t_{1/2}$= 2.5 ± 0.3 for HEK-MDR, HEK-PC, and HEK-MRP, respectively.

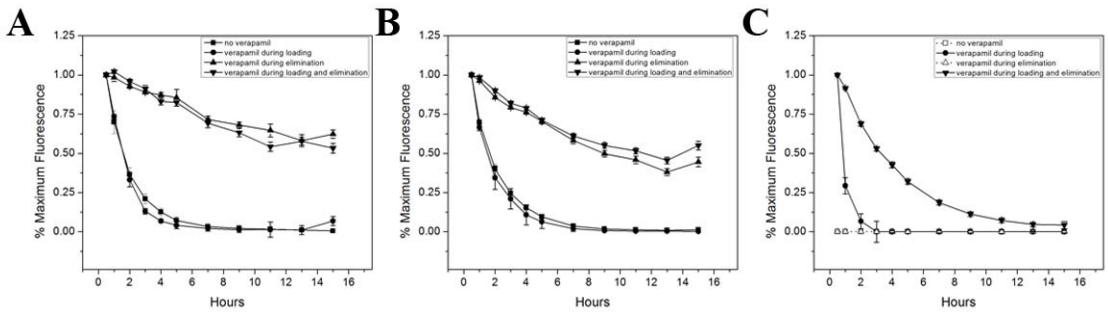

Figure 4-3. **Verapamil inhibition during elimination decreases elimination and increases the half life. To determine verapamil's effect on elimination, HEK-PC (A), HEK-MRP (B), and HEK-MDR (C), spheroids were incubated with verapamil at different phases of the elimination experiment: during loading only, during loading and elimination, or during elimination only. In control spheroids (HEK-PC and HEK-MRP), verapamil treatment during loading did not change the rate of elimination compared to spheroids not treated with verapamil. However, verapamil treatment during elimination significantly decreased the rate of elimination rate ($t_{1/2}$= 1.7 ± 0.5 to $t_{1/2}$= 19.1 ± 0.5). Additionally, the timing of verapamil treatment in HEK-MDR spheroids proved critical. Verapamil treatment during loading is necessary to load HEK-MDR spheroids with rh123, and verapamil treatment during elimination significantly reduced the rate of elimination ($t_{1/2}$=0.4 ± 0.2 versus $t_{1/2}$=2.8 ± 0.2).**

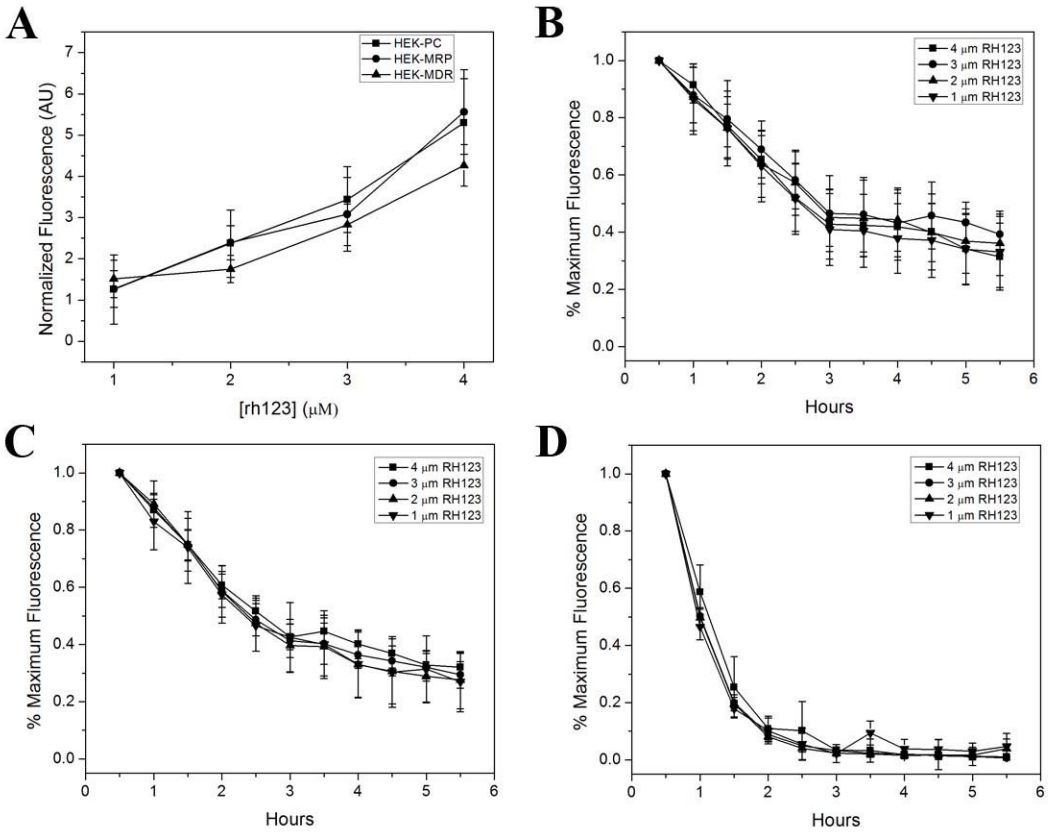

Figure 4-4. **Elimination of rh123 by HEK spheroids is not concentration dependent. HEK-PC, HEK-MRP, and HEK-MDR spheroids were incubated with varying concentrations of rh123 (1, 2, 3, and 4 μM) in the presence of verapamil (100 μM). At the initial time point (t=30 minutes), total fluorescence in each spheroid was quantified and normalized to spheroid volume. Increasing the concentration of rh123 and increasing the time of incubation resulted in increased rh123 loading for all three types of spheroids (A). Elimination was quantified for all three types of spheroids at each of the rh123 concentrations that had been loaded for 2 hours (B, C, D). For each spheroid type, the rate of elimination was not changed when loading of rh123 was increased. As expected, elimination by HEK-MDR spheroids was significantly faster than HEK-PC and HEK-MRP spheroids.**

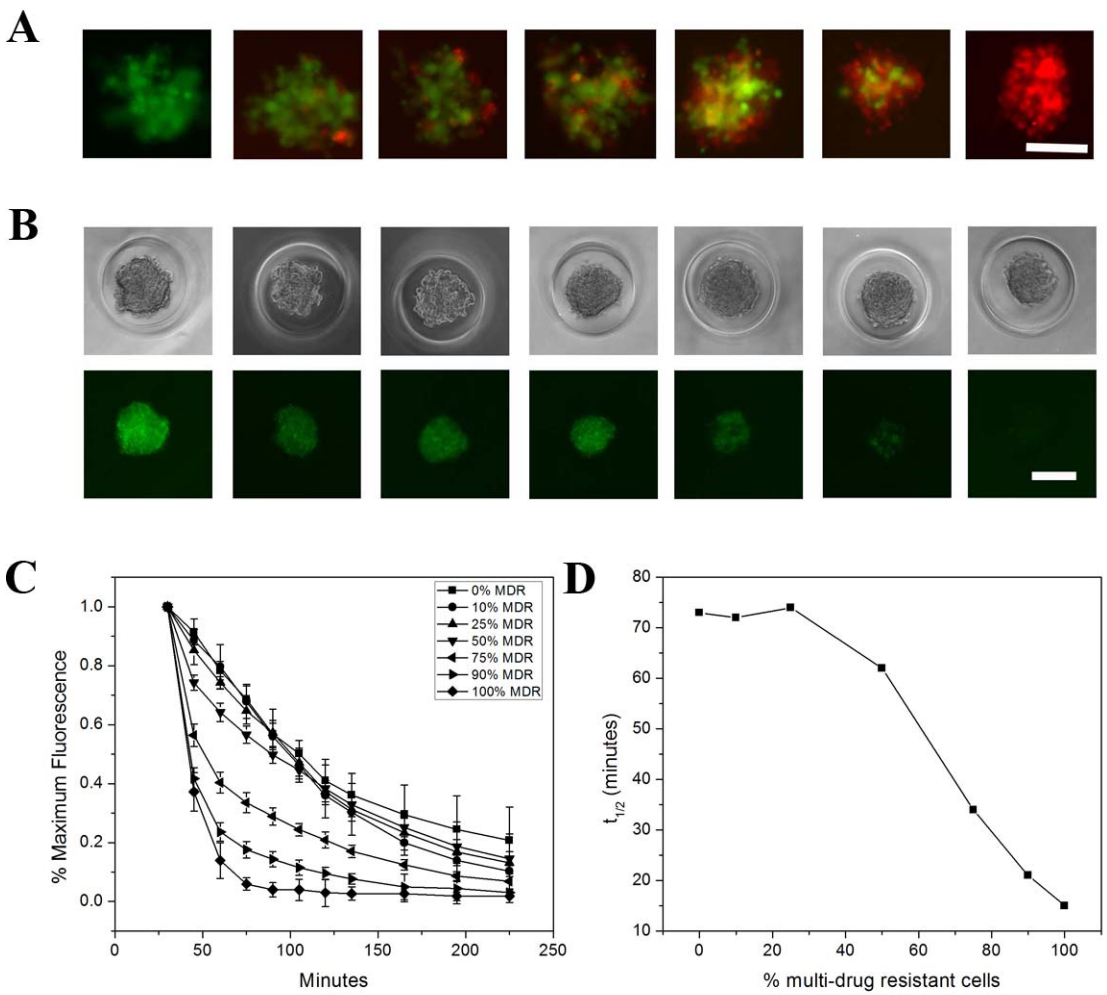

Figure 4-5. Increasing the proportion of MDR cells in a mixed spheroid increases the rate of rh123 elimination. Labeled HEK-PC cells (green) and labeled HEK-MDR cells (red) were mixed at different ratios and seeded into gels to form spheroids. Twenty four hours later, fluorescent images (A) and phase contrast images (B) show the cells have self-assembled mixed spheroids. Cells were not randomly distributed. Spheroids contained clusters of HEK-PC cells surrounded by HEK-MDR cells, especially when the percentage of HEK-MDR cells was greater than 50%. Mixed spheroids were loaded with rh123 (1 μM) in the presence of verapamil (100 μM) to achieve comparable loading and rh123 elimination was measured from fluorescent time-lapse images. Images at 105 minutes, showed that total spheroid fluorescence increased as the proportion of HEK-MDR cells was increased. Fluorescence was not evenly distributed throughout the spheroid for all mixes. For mixtures with greater than 50%HEK-MDR cells, there were clusters of highly fluorescent cells surrounded by cells with little to no fluorescence. Time lapse images were used to quantify the rate of rh123 elimination from the entire spheroid for this range of mixed spheroids (C). As the percentage of MDR cells increased in the mixed spheroids, the rate of elimination also increased. Likewise, the $t_{1/2}$ showed a similar trend, $t_{1/2}$ decreased as the percentage of MDR cells increased (D).

5. Conclusions and Future Directions

This thesis set out to investigate three specific aims: (1) to develop an assay to quantify fluorescence in 3D microtissues using wide-field fluorescent microscopy, (2) to quantify the effect of transport pump inhibition on the uptake, transport, and penetration through 3D microtissues, and (3) to quantify the elimination rate of transporter substrates out of 3D microtissues. These objectives were created so that ABC-transporters, here specifically P-glycoprotein, could be studied in a 3D environment that more closely replicates the *in vivo* environment to further define their role in the complex processes of multi-drug resistance and drug ADME-Tox.

Chapter 1 provided a review of the ABC family of transporters, with a particular emphasis on Pgp. This chapter discussed the mechanism by which ABC-transporters worked and their involvement in normal body physiology, the pharmacokinetics of drugs, and in cancer. Much of the review provided a discussion on the numerous *in vitro* assays that have been developed to determine if a test drug is wither a substrate or inhibitor of the pump, to determine the vectorial transport rate, and to predict potential drug-drug or drug-transporter mediated interactions. After this comprehensive review of the literature, it was apparent that missing from the *in vitro* toolbox of assays was a three-dimensional assay to study these complex interactions. This would be an important addition to the current assays, especially since it is well documented that transporter expression profiles vary depending on culture conditions, and that cancer cells are more resistant when cultured as 3D spheroids.

In chapter 2, a novel assay to quantify fluorescence in 3D microtissues using wide-field fluorescent microscopy for a broad range of application was developed. The application in chapter 2 was to quantify the self-sorting of a mixed population of cells

during the self-assembly process. We accomplished this by estimating the 3D spheroid as a series of fluorescent concentric shells, modeled by a custom Matlab algorithm that was developed. This assay is straightforward and amenable to high throughput analysis for several important applications. Additionally, since this assay is image-based and can quantify a time-lapse experiment we can obtain both endpoint and kinetic values critical to the analysis. Although the chapter only describes this assay in terms of the quantification of self-sorting of two cell types, the usefulness of the assay is in its potential for broad range applications, including quantifying the self-sorting of additional cell pairs, for use in drug discovery, and toxicity testing.

In chapter 3, we adapted our assay developed in chapter 2 for the particular use of creating a quantitative *in vitro* assay to measure the uptake and transport of fluorescent molecules through 3D microtissues as a more predictive model to study drug efficacy and toxicity during drug discovery. By using a known substrate (calcein-AM) of P-glycoprotein and known inhibitors (verapamil, loperamide, and cyclosporine A) we demonstrated the importance of studying the effects of uptake, and transport of substances, as well as the effects of modulators of the pumps in 3D. We showed that inhibition of Pgp could lead to unwanted side effects, such as decreased transport and penetration through the tissue, which can only be manifested in the 3D environment. The model uncovered previously unknown effects of some drugs, in particular we noted that transport through gap junctional communication is inhibited by some modulators of Pgp. Therefore, in addition to our assay measuring the uptake and transport through microtissues, our method is a new, more effective assay to measure gap junctional communication between cells. This new *in vitro* method has the potential for discovering

new more effective inhibitors of efflux transporters responsible for multi-drug resistance and would be useful in the early identification of potential side effects and DDIs of new drug candidates.

In chapter 4 we used another known Pgp substrate (rhodamine 123) to measure the importance of Pgp expression to the elimination of substrates. While elimination is a commonly quantified pharmacokinetic parameter, it is typically calculated via indirect methods such as the concentration of drug in the blood plasma and urine, and not directly from tissues and cells. This chapter also demonstrated the versatility of our system as we measured the elimination kinetics out of spheroids containing more than one cell type. These chimeric tissues, consisting of high and low expressing pump cells, can be used as models for different organs, the same organ with differential expression of transporters, or as tumor models with increasing levels of multi-drug resistance.

In total, we have developed important assays to determine the uptake, transport, and elimination from 3D microtissues. It is proposed that this assay can be used during drug discovery as a more predictive assay of drug-transporter mediated interactions and their effect on drug ADME-Tox, and as an assay to identify inhibitors of transporters to predict their efficacy in the *in vivo* environment. These assays have the potential to study a broad range of substrates and transporters.

5.1 A Novel Method to Obtain Quantitative High Content Information from Wide-Field Fluorescent Images of 3D Microtissues

We have invented a novel method to obtain quantitative high content information from wide field fluorescent images of 3D microtissues. The method can measure and calculate the concentration of a fluorescent molecule at any point in the 3D volume of a 3D microtissue. 3D microtissues are superior to mono-layers of cells grown in 2D because 3D better replicates tissue function and also replicates the natural microenvironments of in vivo tissues and organs. For example, 3D microtissues replicate gradients of nutrients, metabolic waste products, and oxygen better than a thin layer of 2D cells. 3D also replicates the cellular barriers and obstacles to drug diffusion that are important for a drug's efficacy. Our method uses wide fluorescent images of 3D microtissues, extracts reliable quantitative information from these images and uses equations and simulations to measure and predict the concentration of a fluorescent molecule at any point in the volume of the 3D microtissue. For example, our method can determine the concentration of a fluorescent molecule in the cells that form the outer shell of a 3D spheroid and compare that to the concentration of the fluorescent molecule in the center of the spheroid. Further, the method determines the gradient in concentration from outer shell to inner core of the fluorescent molecule. This quantitative information is important for many applications including drug discovery. For example, to be effective an anti-cancer drug must be able to diffuse through the outer shell of cells and reach sufficiently high concentrations to kill cancer cells in the center of the microtissue. There are barriers both passive and active that prevent this diffusion and invention 2 discussed below covers one of those applications. In addition to the cancer drug application, our method has a broad range of applications because there are many fluorescent molecules

(small molecules, green fluorescent proteins, etc) that have been engineered to report on various activities and functions of cells (calcium concentration, gene expression, etc). Our quantitative method is applicable to automated high through put methods and can provide a 3D map of the concentration of these molecules thereby providing high content and high quality information about the complex 3D microenvironments of multi-cellular microtissues important for research, drug discovery and drug toxicity

5.2 Use of a Novel Method to Obtain Quantitative High Content Information from Wide-Field Fluorescent Images of 3D Microtissues for Purposes of Drug Screening

Multidrug-resistance transporters (MDR) are protein pumps that are upregulated in diseased cells such as cancer cells. These proteins actively pump out therapeutic drugs making the cells resistant to treatment. There is a clinical need to discover a drug that inhibits these pumps (to be co-delivered with the therapeutic drug), while not affecting the uptake and transport of the therapeutic drug. Currently, there are three methods used to characterize or screen for drugs that inhibit MDR; monolayer efflux studies of radiolabeled compounds in transwells, drug-stimulated ATPase activity, and calcein uptake assays. Each of these methods uses monolayers of cells, but these methods do not adequately predict in vivo efficacy. It is well established that cells in a monolayer do not accurately replicate all of the complexity and biology of the 3D environment. Of particular importance to drug screening, monolayers of cells do not have mass transport limitations which are major barriers to drug transport/diffusion in 3D tumors. For example, in the calcein uptake assay, fluorescent calcein is an easy to measure surrogate for a therapeutic drug. When MDR is inhibited in this assay, calcein uptake is increased because it is not being pumped out. However, because the assay is performed on monolayers of cells there is no 3D information in this method.

We have used our novel method of obtaining quantitative 3D information from wide field fluorescent images to invent a new method for identifying and quantitatively characterizing inhibitors of MDR and determining their effectiveness in 3D. Our method measures the uptake and transport/diffusion of fluorescent calcein through 3D multi-cellular spheroids. In the presence of verapamil, an inhibitor of MDR, calcein concentration is increased in the spheroid's outer shell of cells. But surprisingly, this

increased concentration of calcein in the shell does not result in a higher concentration of calcein in the center of the spheroid. In fact, calcein concentration is lower in the center of the spheroid than control spheroids not treated with verapamil. This suggests that although verapamil is inhibiting MDR, it is also inhibiting the transport/diffusion of calcein into the center of the spheroid. This demonstrates that verapamil is not effective at increasing the concentration of a therapeutic drug at the center of a mini-tumor. In contrast, when we tested other inhibitors of MDR (cyclosporine A, loperamide, and vinblastine), we saw increased concentration of calcein in the shell and also in the center of the spheroid. None of the current assays used can provide this information Moreover, for each of these inhibitors of MDR, our method enabled us to calculate the quantitative diffusion, uptake, efflux, and penetration data. This allows us to answer critical questions such as: *Did the MDR inhibitor affect overall calcein (therapeutic drug) uptake? Did the MDR inhibitor affect calcein transport across the multi-layers of cells? Did calcein reach the center of the spheroid? How long did it take to reach the center of the tissue and is the concentration at any location therapeutically relevant?* Our mathematical model yields a complete 3D reconstruction of the concentration profile as a function of time which allows these questions to be readily answered. This method is applicable to a wide variety of different *in vitro* mini-tumors (mammospheres, gliomaspheres, etc), 3D spheroids of cell mixtures that more accurately replicate in vivo barriers to drug transport (e.g., shell of endothelial cells surrounding a core of neural cells as occurs in the blood brain barrier), other fluorescent molecules and drugs besides calcein and other diseases besides cancer where drug transport is important (e.g., cardiovascular, neurological diseases). Our method is amenable to high throughput screening technologies.

5.3 Use of Chimeric 3D Spheroids as Models for Multi-Drug Resistance and Drug ADME-Tox

Quantification of uptake, transport, and elimination in 3D microtissues are an important addition to the existing *in vitro* tool box to study multi-drug resistance and drug ADME-Tox. This thesis has discussed in detail the importance of drug screening in 3D, and the added complexity of chimeric tissues further demonstrates the value of this assay. In terms of inhibiting multi-drug resistance in cancer, these tissues can be engineered to control the amount of pump overexpressing cells that each microtissue expresses. These mini-tumors provide sample to study how increasing percentages of high expressing pump cells change the elimination rate out of the spheroids, as well as how increasing the percentage of pumps expressed changes the interactions with inhibitors. Additionally, since the cells of a tumor are heterogeneous, chimeric tissues more accurately represent the tumor microenvironment, a complexity that cannot be replicated in 2D monolayers. As no pump inhibitors are currently used in the clinic to modulate Pgp or transporters to reverse multi-drug resistance, these chimeric tissues have the ability to fully characterize the system as well as to provide an important intermediary between current techniques and the *in vivo* environment.

As well, the quantification of elimination in these chimeric tissues also proves valuable. It is recognized that transporter pump expression is dynamic, and varies depending on organs within the body. It is also known that the pharmacokinetic parameters important to ADME-Tox are highly depended on the expression level of transporters. These chimeric tissues allow for the in depth study of how variations in transporter expression affects these key parameters, as expression levels in organ change or even as models for different organs. As this assay is amenable to forming spheroids

from nearly all cell types, elimination can be measured directly from spheroids made from cells of the particular organs. An additional possibility with chimeric tissues is to add multiple cell types to replicate the complex barriers observed in the body. For example, a chimeric tissue consisting of brain endothelial cells sorted with either glial cell or neurons can provide a model for the blood-brain barrier to study the uptake and elimination of drugs across this important physiological barrier.